Laser-Induced Fluorescence Imaging in Free-Piston Shock Tunnels

A thesis submitted for the degree
of Doctor of Philosophy of
the Australian National University

Philip Charles Palma

Submitted May 1998

Revised February 1999

The work in this thesis is entirely my own, except as described in the Acknowledgements and where credit is indicated by reference.

Phil Palma

This document was prepared using LaTeX 2_ε. It was compiled on a Macintosh with OzTeX 3.1 written by Andrew Trevorrow. The bibliography was produced using BibTeX 1.1.7 by Vince Darley. The style files used to conform to the ANU formatting requirements were `thesis.sty`, `thesis12.clo` and `thesis.cls` version 1.2, which was modified from D. Jackson's original. The bibliography style file used to produce the author-date referencing system was `harvard.sty`. The hypertext links were created by using the `hyperref` package, version 6.19, by Sebastian Rahtz. Note that citation links that are split across lines are not supported at this time. However, in these situations where the name is disabled, the citation year can be used as a link to the bibliography instead.

Acknowledgements

Six years is a long time. Therefore, the list of people that I need to thank is necessarily a lengthy one. I must begin by thanking my supervisors Brenton Lewis and Frank Houwing for their foresight and encouragement over the years. I should also like to thank my advisors Ken Baldwin and John Sandeman for their advice. Thanks to the shock tunnel research group for their assistance, and in particular Paul Walsh for his technical expertise. Thanks to Tim for his help with the early PLIF experiments. Thanks to Paul Danehy for his invaluable help with the degenerate four-wave mixing experiments, and his advice and assistance in the last round of PLIF experiments. At the Research School of Physics, I had very efficient technical support from Colin Dedman and Kevin Lonsdale for which I am sincerely grateful.

Thanks to Paul-Danehy for proof-reading this thesis and identifying where those-hyphens should-go. I also sincerely appreciate the work of my other proof readers Brenton, Sean and Joe.

I would like to thank my family for their encouragement and support, and for never pushing me.

I also have to thank all my friends who put up with me and kept me going over the years. I couldn't have done it without you. Thanks to Dave, Sam, Jim and Greg for the odd quiet beer. Special thanks to Christina for your love and support. And last, but not least, thanks to Karen for being there when it mattered.

Abstract

PLIF temperature measurements in a free-piston shock tunnel are presented. The viability of performing quantitative temperature measurements is established and application considerations are detailed. A single laser/camera system was used to measure rotational and vibrational temperatures in the freestream and in the shock layers on a wedge, a cylinder and a hemisphere. Two different laser sources were used to excite NO via the $A^2\Sigma^+ \leftarrow X^2\Pi$ transition between 225 and 245 nm. The first was a Raman-shifted tunable excimer laser which was restricted to excitation of the (0,0) band near to 226 nm, and therefore was only utilised for rotational temperature measurements. The other was an excimer-pumped frequency-doubled dye laser which was used to access the first three vibrational bands (0,v''=0–2) and to perform rotational and vibrational temperature measurements. Temperature measurements are compared with computations from CFD codes in an ongoing procedure of testing and validation.

The calculations were performed with a quasi-one-dimensional nozzle flow code (STUBE) which has been modified to include vibrational freezing phenomena. The measured rotational temperature of 439 $\pm$ 20 K compares well with the calculated freestream rotational temperature of 396 $\pm$ 10 K. A vibrational temperature of 4500 $\pm$ 270 K was measured in the stagnation region on the hemisphere. This measurement was estimated to be systematically high by 160 K due to variations in the overlap integral between 225 and 245 nm. The temperature calculated using STUBE was 4146 K. The measured freestream and hemisphere temperatures are higher than those calculated, which questions the validity of the nozzle-reservoir temperature used in the CFD calculations and the method used to obtain it. The freestream vibrational temperature of NO was measured to be 890 $\pm$ 30K which is greater than the calculated value of 670 K. This was anticipated due to the limited vibrational relaxation data available for the calculation.

Contents

List of Figures

List of Tables

Chapter 1

Hypersonic Flows

1.1 Introduction

When the Apollo 11 lunar return vehicle re-entered the Earth's atmosphere after the first successful manned flight to the moon on July 24, 1969, it was travelling at Mach 36—a velocity of 11 km/s. At this velocity, a strong bow shock wave surrounded the nose of the vehicle, and in the layer between the shock wave and vehicle the air was heated to temperatures on the order of 11,000 K. This is hypersonic flight. It is characterised by high temperatures, chemical reactions, and thin shock layers. These high-temperature effects that cause molecules to dissociate, and even ionise, distinguish hypersonic aerodynamics from non-reacting supersonic flows. As a general rule of thumb, Mach 5 marks the boundary between the supersonic and hypersonic flight regimes.

Hypersonic flow is important, not only because of its distinct physical differences from supersonic flow, but because it is the flow regime for which many of the present and future aerospace vehicles are being designed. The aerospace plane is one such design concept. Powered by air-breathing supersonic combustion ramjet engines (SCRAMjets), it is envisioned to take off horizontally from a runway, accelerate into orbit and return to earth and land like a conventional plane. Crucial to the design of such vehicles is the accurate prediction of physical and chemical effects influencing the aerodynamics at hypersonic velocities. The importance of hypersonic effects on aerodynamics is underlined by the anomalies between design predictions and actual flight data for the US space shuttle. Flight experience indicates a substantially greater pitching moment (requiring greater deflection of the body flap) from that predicted. Indeed, as shown by Maus et al. (1984), a comparison of calculations for chemically non-reacting and reacting shock layers indicate a higher pitching moment when the high-temperature effects of hypersonic flows are included.

Realistic evaluation of hypersonic phenomena on a particular vehicle design can be managed in one of three ways: flight tests of actual vehicles; simulation of flight conditions on scale models in ground-based test facilities; or numerical simulations implementing models of physical and chemical processes—known as computational fluid dynamics (CFD). The first case is prohibitively expensive and reserved for the prototype design. Individual ground-based facilities can only simulate flow conditions for a portion of the re-entry trajectory. The flows produced by such facilities only partially simulate re-entry flow conditions. The latter method, CFD, is a promising alternative with the advent of low-cost, high-power computing resources. However, CFD codes require validation against experimental data before they can be confidently used to predict inflight behaviour and aid in vehicle design and performance evaluation. The experimental data must come from the first two methods mentioned above, therefore emphasising the close relationship that exists between the alternative approaches.

The shock tunnel is one such ground-based test facility capable of producing very high enthalpies and shock-layer temperatures. The shock tunnel consists of a hypersonic nozzle attached to the end of a shock tube (see Fig. 1.1). The shock tube generates a shock wave which propagates through the test gas to the end of the shock tube where it is reflected from the end wall. Behind the reflected shock the gas is at a high temperature and pressure. This stagnant slug of shocked gas behaves as a supply reservoir for the nozzle, expanding through the nozzle and into the test section where it achieves hypersonic velocities.

The performance of shock tunnels is limited by the speed of the incident shock wave. The shock speeds were enhanced by the development of the free-piston driver technique which lead to the development of the free-piston shock tunnel (Stalker 1972). The free-piston shock tunnel is capable of producing the high-temperature chemically reacting flow phenomena necessary for the study of re-entry flows. The free-piston driver technique enhances the shock-tube performance by increasing the sound speed in the driver gas[†] (Gaydon and Hurle 1963, p. 92). This method allows high incident shock speeds (2–7 km/s) and hence very high nozzle reservoir temperatures and pressures to be achieved. Shock-tunnel flows generally last for only a few milliseconds as a result of the impulse nature of the shock tube, and as necessitated by the extreme gas temperatures produced.

In the past, many optical techniques have been used for flow visualisation in shock tunnels and to complement surface pressure and heat-transfer measurements. Schlieren photography, shadowgraph and interferometry have been used extensively to provide two-dimensional measurements with high temporal resolution. However, they can only provide an integrated measurement along the line-of-sight through the flow which masks any three-dimensional behaviour in the flow. Planar laser-

[†]The driver gas is compressed by the piston against a diaphragm which on rupturing produces a shock wave travelling through the test gas in the shock tube. For more information on shock tubes see Gaydon and Hurle (1963).

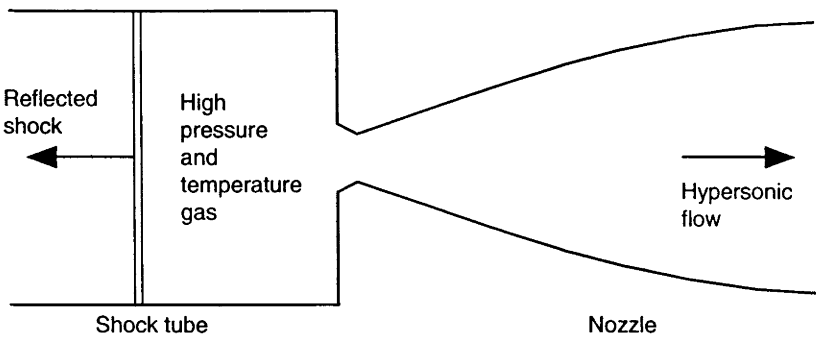

Figure 1.1: Schematic of a shock tunnel.

induced fluorescence (PLIF) has been widely used for flow visualisation in subsonic and supersonic flows and as a combustion diagnostic (Seitzman and Hanson 1993, Eckbreth 1996). It provides high spatial and temporal resolution, two-dimensional quantitative measurements and is chemical species specific. PLIF uses a thin sheet of laser light to excite a radiative transition in a particular chemical species in the flow. The laser sheet interrogates a thin ($\leq$1 mm) cross section through the flowfield and therefore PLIF can resolve three-dimensional features in flows, unlike the aforementioned line-of-sight techniques. The short duration of the laser pulse and resulting fluorescence gives PLIF the ability to freeze the motion of hypersonic flows, which makes it particularly applicable to shock tunnels.

The high-enthalpy flows produced by free-piston shock tunnels have a unique set of experimental problems not encountered in other flow facilities. There are large pressure and temperature variations which cause large fluorescence signal variations due to high collisional quenching rates and changes to the spectral overlap integral between the laser and the absorption transition (Allen et al. 1995, Quagliaroli et al. 1994). Other problems include excessive laser-beam absorption which can lead to hole burning of the laser spectral profile (Ruyten et al. 1995), spectral interference from other flow species and fluorescence trapping. A more severe problem is that metallic contaminants which are eroded from the shock tube walls produce strong emission in high-temperature regions in the flowfield (Palma et al. 1993). This background emission can easily overwhelm the fluorescence signals, so careful spectral and temporal filtering of the signal is necessary.

This thesis describes the development and use of PLIF as a diagnostic tool to be used on shock tunnels. In particular, the ability to perform accurate temperature measurements for the eventual validation of CFD codes is investigated. LIF imaging is also used to observe flow non-uniformities which can significantly effect experimental results and hamper validation of CFD codes. The remainder of this chapter provides an introduction to hypersonic flows and the concepts involved in CFD code

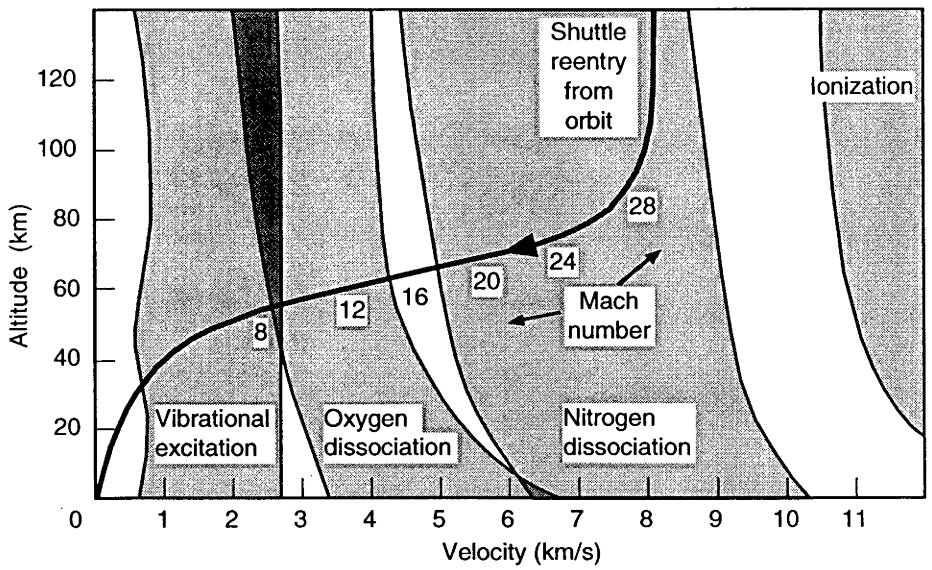

Figure 1.2: An altitude-velocity map for an aerospace vehicle returning from orbit. Also indicated is the Mach number along the re-entry trajectory and the regions of vibrational excitation, dissociation and ionisation. (After Anderson (1989).)

validation. A review of the scientific literature pertaining to LIF and LIF imaging is also presented.

1.2 Hypersonic Flows

A typical re-entry trajectory for an aerospace vehicle returning from orbit is shown on the altitude-velocity map in Fig. 1.2. Throughout the descent from orbit, the vehicle experiences a range of flow phenomena due to the variations in density and velocity. As the velocity of the vehicle decreases, the kinetic energy of the vehicle is converted into thermal energy and this causes chemical reactions in the gas near its surface to ensue. A variety of viscous and high-temperature effects are discussed below. The density variation along the trajectory influences chemical-relaxation rates and at high altitudes low-density (non-continuum) phenomena also occur.

The hypersonic flow regime begins when the Mach number is increased to a value where certain physical flow phenomena become noticeable. These phenomena that characterise hypersonic flow are (Anderson 1989, pp. 14–24):

- *Thin shock layers.* As the Mach number increases, the density increase across the shock also increases, and hence the shock lies closer to the body. The

flow region between the shock and the body is called the shock layer and at hypersonic velocities can be quite thin.

- *Entropy layer.* Consider a hypersonic flow over a blunt body where the shock at the nose is nearly normal and detached from the body. Since entropy increases across a shock, and increases more for stronger shocks, there is a region after the shock of strong entropy gradients. This fluid with increased entropy flows downstream over the vehicle and is termed the entropy layer. Vorticity is also associated with entropy gradients and therefore the interaction of the entropy layer and boundary layer can complicate the flow.

- *Viscous interaction.* As the flow is slowed in the boundary layer, kinetic energy is transformed into internal energy of the gas. This is known as viscous dissipation and causes a temperature increase in the boundary layer. It is a dominant characteristic of hypersonic boundary layers and causes a thickening of the boundary layer through a decrease in the density and an increase in viscosity. The thickened boundary layer influences the inviscid flow outside the boundary layer which in turn feeds back to affect the growth of the boundary layer. This is called viscous interaction. The surface pressure distributions, skin friction and heat transfer are all affected by viscous interaction and hence it plays a significant role in the aerodynamics of hypersonic vehicles.

- *High-temperature effects.* At high velocities the viscous dissipation in the boundary layer causes very high temperatures. High temperatures also occur in the nose region of the vehicle, behind the normal bow shock. Initially, as temperature increases, vibrational excitation of the molecules becomes important, absorbing energy that would otherwise go into the translational and rotational excitation modes of the molecules. At higher temperatures the molecules begin to dissociate and ionise. The result is a chemically reacting gas which has a significant effect on the lift, drag, and moments of the hypersonic vehicle. The most dominant effect, and the one that influences hypersonic aerodynamic design most, is the high heat-transfer rates from the boundary layer to the vehicle's surface. As well as convective heat transfer from the boundary layer to the surface, thermal radiation from the high-temperature gas can also provide a significant contribution to surface heating. In summary, the two major physical characteristics that differentiate non-reacting gas flows from high-temperature gas flows are:

  1. vibrational excitation.
  2. dissociation and ionisation leading to chemically-reacting flows.

  Figure 1.2 indicates the regions in which these high-temperature phenomena occur on a altitude-velocity map.

- *Low-density effects.* At altitudes above about 150 km, the gas density is low and behaves like a stream of discrete particles. This is known as *free-molecular flow* and is characterised by diffuse shocks and thick boundary layers that can

fill the entire shock layer. At lower altitudes, the mean free path between collisions becomes much less than the characteristic flow length (length over which flow properties are changing) and the gas behaves more like a *continuum.* Between approximately 150 and 90 km is a transition regime where continuum models are modified to account for low-density effects. These include temperature and velocity slip at the vehicle's surface where the temperature is no longer constrained to be the wall temperature, and the velocity is no longer constrained to be zero, as they are in continuum models. Below approximately 90 km, the flow behaves on a macroscopic scale like a continuous material—a property utilised in deriving the fundamental equations of fluid flows. The Knudsen number is the important parameter for low density flows. It is defined as the ratio of the molecular mean free path λ to the typical vehicle dimension L, that is, $Kn = \lambda/L$. For the shuttle, values of 10 or more indicate molecular free flow and $0.03 < Kn < 10$ indicates the transition regime between continuum and non-continuum flow.

High-temperature effects are often described in the aerodynamic literature as *real-gas effects.* A *perfect gas* is defined as *a gas in which intermolecular forces are neglected* and it follows that a real gas is one which intermolecular forces are important. At very low temperatures and high pressures, the molecules of a gas are more closely packed and intermolecular forces become more important. However, common usage of the term real gas by the hypersonic community refers to the high-temperature effects such as vibrational excitation and chemical reactions. For the flows encountered in this text intermolecular forces are not important and so high-temperature effects will often be referred to as real-gas effects.

1.2.1 Non-Equilibrium Phenomena

Chemical reactions proceed at a finite rate. If the flow properties are changing too rapidly for chemical reactions to maintain equilibrium with the local flow properties, a state of *non-equilibrium* occurs. If we define l_f as the characteristic length scale over which the flow properties are changing (represented for example by a vehicle dimension such as the nose radius), and define l_c as the characteristic length scale for chemical reactions to achieve equilibrium, then we can define the following three regimes:

$l_c \ll l_f$ *Equilibrium* — chemistry is in equilibrium with the local flow properties.

$l_c \approx l_f$ *Non-equilibrium* — chemistry is changing but is not in equilibrium.

$l_c \gg l_f$ *Frozen* — chemistry is effectively "frozen", not changing at all.

The collision rate determines the magnitude of l_c and therefore as the density varies with altitude the state of chemical equilibrium also changes.

An analogous description can be used to describe the distribution of energy amongst the various energy modes of molecules (*e.g.*, translation, rotation, vibration, electronic). Rotation rapidly equilibrates with translation, whereas vibration requires a much greater number of collisions to equilibrate with translation. Defining l_v as the characteristic length scale for vibrational relaxation, we can define the same regimes of equilibrium, frozen and non-equilibrium for vibration as for chemistry. Therefore, vibrational equilibrium requires $l_v \ll l_f$. Non-equilibrium vibration and chemistry are important features of hypersonic flows.

1.3 Validation of CFD Codes

The problems encountered by designers of hypersonic vehicles are numerous. To begin with, the hypersonic environment is characterised by a variety of flow phenomena which may include boundary-layer transition and turbulence, viscous/inviscid interactions, separated flows, non-equilibrium chemistry, surface catalycity, ablation and non-continuum effects (Bertin 1994). Which of these phenomena are important depends on the end application (*i.e.*, mission requirements, vehicle size, trajectory etc.). The design is further complicated if the vehicle is to be powered by an air-breathing scramjet engine which is integrated into the airframe design.

Designers have at their disposal several methods to aid in the design process: CFD codes, ground-based test facilities, and flight tests. According to Bertin (1994), "Only flight tests of the full-scale vehicle provide an uncompromising representation of the vehicle's environment." However, design, fabrication and testing of full-scale vehicles is prohibitively expensive. Neither CFD nor ground-tests alone provide the necessary information required by the designer. Therefore, designers should utilise the best combination of available tools, experimental and computational.

1.3.1 Definitions

The stringency of testing performed on a CFD code dictates the level of confidence the user should have in the code's ability to simulate reality. Accordingly, there are a number of definitions associated with ranking the credibility of codes. Bradley (1988) distinguishes elegantly between *validation* and *calibration*:

> CFD code validation implies detailed surface and flowfield comparisons with experimental data to verify the code's ability to accurately model

> the critical physics of the flow. Validation can occur only when the accuracy and limitations of the experimental data are known and thoroughly understood and when the accuracy and limitations of the code's numerical algorithms, grid-density effects, and physical basis are equally known and understood over a range of specified parameters.
>
> CFD code calibration implies the comparison of CFD code results with experimental data for realistic geometries that are similar to the ones of design interest, made in order to provide a measure of the code's ability to predict specific parameters that are of importance to the design objectives without necessarily verifying that all the features of the flow are correctly modelled.

The process of establishing the credibility of a code is called code *certification.* Mehta (1990) elaborates on these definitions and also adds that a CFD code may be certified by another already certified code, which occurs often during code development due to the limited availability of experimental data.

Note that surface and integrated measurements (*e.g.,* forces, moments) are not sufficient for code validation. Extensive measurements in the flow away from the surface are required to validate a code's ability to model the important flow phenomena.

1.3.2 Ground-Based Testing

According to Bertin (1994), "Complete simulations of the flowfield cannot be obtained in any one ground-based facility." Despite the limitations of ground-based facilities, they still remain the source for the majority of experimental data on hypersonic flows. Since perfect simulation is unfeasible, the designers should identify the critical parameters and objectives of a particular test program, and then utilise many different facilities to achieve their results. In this regard, Korkegi (1985) notes some of the advantages of CFD over wind-tunnel testing:

> CFD can, in principle, give considerably greater detail of a flowfield than is possible in any wind tunnel as all aerodynamic parameters are computed at each grid point. CFD provides a capability for configuration changes before commitment to model construction is made. In this respect, CFD helps in making more effective use of ground-test facilities. On the other hand, when integrated forces and moments are desired, CFD is subject to inherent mathematical inaccuracies associated with small differences of large numbers.

Neumann (1988), however, warns "The codes are NOT an end in themselves ... They represent engineering tools; tools that require engineering judgement to use

and critical appraisal to understand." Ground-based tests are necessary. Apart from validation and calibration, ground-tests are required especially in circumstances where CFD results are unreliable or exceed computational power. The calculation of integrated aerodynamic forces and moments and/or heat transfer distributions for an entire vehicle is one such case.

1.3.3 Requirements for CFD Validation

With the increasing use of wind-tunnel tests for validation and calibration of CFD codes, a summary of the experimental requirements for code validation is presented. These requirements are separated into three categories (Boyce 1995):

1. *Facilities.* There are various types of ground-test facilities—shock tubes, arc jets, hypervelocity wind tunnels, ballistic ranges, expansion tubes—each with unique advantages and disadvantages. Multiple facilities should be used to ensure all relevant flow phenomena have been simulated (*e.g.,* for re-entry flows this requires simulation of real-gas effects).

2. *Measurements.* The accuracy of measurements should be at least comparable to that expected from computations. Apart from minimising experimental error, measurements should be repeated with different instruments and in different facilities (redundancy) to remove possible systematic or facility-dependent errors. Several types of measurements are possible. Global or integrated measurements are important in aerodynamic design but say nothing about the distribution of the quantity and can therefore not be used for code validation. Surface measurements (*e.g.,* pressure, heat transfer) are valuable and can be used for calibration, but on their own are insufficient for validation. Flow visualisation techniques which measure density variations (*e.g.,* schlieren photography, shadowgraph, interferometry) provide extensive information about flowfield parameters and can be used to evaluate effects of chemistry in CFD codes. Non-intrusive laser-based methods which utilise spectroscopic and non-linear optical techniques for planar and point-wise measurements are capable of determining flow parameters such as: rotational and vibrational temperatures, species concentrations and velocities. They are ideal for code validation.

3. *Methodology.* The process of validation should commence with the study of simple flows (*i.e.,* continuum, no real-gas effects) and gradually increase complexity of the flow (*i.e.,* increase Mach number, add chemistry). Experiments should be designed to test a single flow phenomenon while minimising competing effects that may complicate data interpretation (cause-and-effect tests). Simple models can be used to test specific flow phenomena and in some cases this is more desirable. The sensitivity of flow parameters can be determined

from CFD modelling and can help direct the experimentalist as to what parameters to measure. The experiments should simulate effects (*e.g.*, chemistry) found in the end application of the code since unexpected results can occur otherwise. Finally, since the facilities only partially simulate re-entry flows, it is vital for code validation that the freestream be fully characterised. As Neumann (1989) puts it, the experimentalist "should spend more time characterising, and less time trying to improve, his bad flows, and the numericist should apply his expertise to including the bad nature of the flow in his calculations."

1.4 Optical Diagnostics for Shock-Tunnel Flows

Shock waves were first visualised with the schlieren method by August Toepler (1875) as reviewed by Krehl and Engemann (1995). Ernst Mach later went on to study shock waves in detail and discovered the Mach reflection effect (Mach and Wosyka 1875). With the schlieren technique, the final image obtained of the flow is related to the first derivative of the density. The shadow technique is similar in practice to schlieren, however the image produced of the flow is related to the second derivative of the density. To obtain the density from these methods requires integration, however this is avoided if one uses interferometry in which the density field is obtained directly. These are the traditional methods for visualisation of wind-tunnel flows and are reviewed briefly by Liepmann and Roshko (1957).

There are many other techniques which are now applied to wind tunnels and combustion environments, some of which owe their feasibility to the invention of the laser. Absorption, Raman and Rayleigh scattering, laser-induced fluorescence (LIF), coherent anti-Stokes Raman scattering (CARS) and degenerate four-wave mixing (DFWM) are a few (see Eckbreth (1996) and Demtröder (1996) for a review of these and other laser-spectroscopic methods). In this section and the next we will be concerned only with the use of LIF imaging relevant to the current application.

Consider some of the desired attributes of a diagnostic technique to be used on a shock tunnel. As mentioned in the previous section on CFD validation, accuracy of measurements is an important factor to be considered. Also, shock tunnels are impulse facilities and hence require measurements to be made during time intervals on the order of a millisecond. Most currently available laser systems can only provide a single pulse on this time scale, so techniques that can make a measurement in a single laser pulse are favoured. Techniques that produce instantaneous measurements (one measurement per tunnel run) are desirable to reduce both expense and time requirements. Shock-tunnel flows are quite luminous, especially in the high-temperature shock-layer regions, and hence techniques that can reject background interferences are preferred. Multiple or planar measurements are also desirable because they re-

duce the expense associated with performing many point-wise measurements over many tunnel runs. Planar measurements are also capable of resolving turbulence effects. Measurements of vibrational and rotational temperatures can be used to directly test vibrational-excitation models in CFD codes, and also indirectly test chemistry models. Chemistry is directly verified by measurements of species number densities. No single technique has all of these attributes.

In this work, we will consider only temperature measurements. Single-pulse CARS thermometry on N_2 has been demonstrated to have an accuracy of 2% (Hahn et al. 1997, Snowdon et al. 1991). CARS is a well established technique and incorporates many of the benefits of nonlinear techniques. The coherent signal beam allows complete collection of the signal and rejection of interferences, which is ideal for luminous environments such as shock layers in hypersonic flows. However, it is a point-wise measurement and is generally restricted to major flow constituents. PLIF, on the other hand, provides two-dimensional measurements with very high sensitivity, making it applicable to the detection of trace species and reaction intermediates. Two-line instantaneous PLIF thermometry is inherently less accurate than CARS thermometry which uses sophisticated algorithms to fit whole vibrational bands to calculated spectra. The two-line PLIF approach, on the other hand, compares the fluorescence signals from only two sequentially-excited transitions to arrive at a determination of the temperature. Therefore, in situations where the accuracy of PLIF is inadequate but the two-dimensional nature is desirable, the calibration of the PLIF results with a single-point CARS measurement would appear to be a practical solution.

A vast amount of the scientific literature on PLIF is devoted to the detection of hydroxyl radicals (OH) in combustion environments. However, since OH is not present in non-combusting shock-tunnel flows we will concentrate on nitric oxide (NO). NO is naturally present in heated-air flows such as those examined here. This situation is often preferable to seeding a chemical species into the flow which can often be impractical or may influence the dynamics of the flow. NO has some advantageous spectroscopic properties that make it an excellent choice for PLIF thermometry. NO has excited-state radiative lifetimes and collisional-quenching rates that are independent of rotational quantum number (McDermid and Laudenslager 1982) and it also exhibits strong non-resonant fluorescence which alleviates problems associated with radiative trapping and laser scatter. The spectroscopy of NO is also very well characterised which significantly simplifies data analysis and modelling.

1.5 Literature Review for Planar Laser-Induced Fluorescence

Cattolica and Stephenson (1984) presented the first two-dimensional PLIF ther-

mometry measurements. They measured the vibrational temperature of OH in a methane-air flame using a frame-averaged two-line approach. Kychakoff et al. (1984) imaged NO fluorescence for the first time and suggested NO for use in temperature measurements. Instantaneous PLIF temperature measurements with a single laser/camera system (one-line technique) were performed by several authors by assuming a constant species mole fraction and temperature independent quench rates (Seitzman et al. 1985, Lee 1991, Allen et al. 1992). Instantaneous PLIF thermometry using the two-line technique was performed on OH using two lasers and two cameras by Paul and Hanson (1990) and Allen et al. (1990).

For supersonic flows, PLIF has been used to measure rotational temperatures (McMillin et al. 1991, Palmer et al. 1992, McMillin et al. 1993, Palmer and Hanson 1995), vibrational temperatures (McMillin et al. 1992, Palmer et al. 1993), velocity (McDaniel et al. 1983, Paul et al. 1989), pressure (Lemoine and Leporcq 1995), combined velocity and pressure (Hiller and Hanson 1988), and mole fraction (Abbitt et al. 1991). A multi-line method that uses four NO rotational transitions rather than just two was used by Palmer et al. (1996) to determine rotational temperature in a shock-tunnel free jet. This provided sensitivity to a greater range of temperatures and improved measurement accuracy. PLIF thermometry in a shock layer in a small-scale expansion tube has also been performed (Houwing et al. 1996).

The application to large-scale facilities capable of simulating hypersonic flows has been much slower. This is partly due to metallic contaminants which are eroded from the shock-tube walls and produce strong emission in high-temperature regions in the flowfield (Palma et al. 1993). This background emission (flow luminosity) can easily overwhelm fluorescence signals, so careful spectral and temporal filtering of the LIF signal is necessary.

Ruyten (1996) has applied PLIF in NO to a free-piston shock tunnel at the Arnold Engineering Development Center (AEDC). In order to interpret the data, an extensive computational model of the fluorescence process was developed—computational flow imaging (CFI-PLIF) (Ruyten et al. 1995). Flow luminosity in the nose region of a blunted cone was too severe to make any measurements, and so subsequent measurements were made some distance downstream. Apart from flow luminosity due to contaminants, significant amounts of laser attenuation and spectral hole burning in the laser-line profile further complicated the analysis. The temperature measurements are reported with an accuracy of 30%.

An important contribution to the development of PLIF for shock-tunnel diagnostics has come from experiments performed on model scramjet combusters in shock tunnels (Allen et al. 1993). Combined NO and OH PLIF measurements were used to visualise the reaction-zone interface. In a related study, PLIF imaging of OH, NO and high temperature O_2 was performed in spray flame combusters at pressures ranging from 1 to 10 atm (Allen et al. 1995). Di Rosa (1996) also describes NO and O_2 LIF measurements in flames at pressures from 1 to 10 atm and identifies

regions in the NO excitation spectrum where minimum interference from O_2 absorption can be found. These methods for dealing with high-pressure environments are important for future measurements in shock layers.

The high-enthalpy shock tunnel (HEG) at the DLR, Göttingen, is the largest free-piston shock tunnel in operation. Measurements of spectrally resolved LIF along a line across a bow shock have been made (Beck et al. 1996, Wollenhaupt et al. 1997). The excitation scheme employed differs from most other studies in that a tunable ArF excimer laser was used to excite NO at 193 nm. The spectrally resolved LIF signals were used to determine freestream vibrational temperatures. Post-shock signals were observed for the first time due to the combined use of several methods to reduce the influence of flow luminosity. Their proposed instantaneous two-laser/two-camera experiments will use LIF performed in a heated reference cell to make corrections to the tunnel LIF signals for pulse-to-pulse fluctuations in laser spectral profiles. In a test experiment, this correction was observed to reduce the standard deviation in the temperature measurement by a factor of three over an energy correction alone. Special custom-made reflective filters are used to increase the fluorescence-signal to flow-luminosity ratio.

1.6 Aim and Overview of Thesis

The importance of accurate non-intrusive flowfield measurements of many parameters has been established. Measurements in high-enthalpy facilities that reproduce real-gas effects are of critical importance to CFD validation, fundamental studies of real-gas effects and for facility characterisation. The development and application of one such technique, PLIF, is the aim of this thesis.

Chapter 2 contains a review of basic absorption theory as related to LIF. A simple analytic model is developed and its limits of applicability tested against numerical simulations based on rate-equation models. Strategies for the measurement of rotational and vibrational temperatures are presented.

PLIF thermometry in a free-piston shock tunnel is presented in Chap. 3. A Raman-shifted tunable excimer laser is used to excite NO at 225 nm. Three transitions were used derive rotational temperature maps for flows over a cylinder and a wedge. Despite numerous difficulties, good agreement between experiment and calculations is reported. However, the most notable outcome from these experiments is an improved understanding of the requirements for performing accurate PLIF thermometry.

Chapter 4 describes a review of the operation of the free-piston shock tunnel, and the characterisation of the freestream flow through conventional pressure measurements

and comparisons with basic CFD codes. In Chap. 5, optimisation of the PLIF thermometry technique is considered. In particular, coatings for reflective filters are designed which will allow optimised fluorescence-signal to background ratios. Also, the process of transition selection is partially automated in an attempt to balance the many optimisation parameters presented by the PLIF technique. Finally, Chap. 6 presents the results of the re-engineered experiment with significantly improved results.

1.7 A Note on Units

Spectroscopic units have been chosen rather than the MKS system for the laser-spectroscopic parts of this monograph. In most cases, conversions to MKS units are given in the text for important quantities (such as the Einstein B coefficient). In particular, this means frequency is in cm^{-1} and irradiance is W/cm^2. When the word 'spectral' prefixes a quantity it is taken that this quantity has units of 'per frequency interval' (or per cm^{-1}). For example, spectral irradiance has units of $W/cm^2/cm^{-1}$. The conversion of frequency from cm^{-1} to Hz is given by

$$f[Hz] = c\nu \tag{1.1}$$

where c [cm/s] is the speed of light.

Chapter 2

Theoretical Aspects of Laser-Induced Fluorescence

2.1 Introduction

The theory of laser-induced fluorescence (LIF) is well developed. In simplistic terms, it can be described as the absorption of laser light via an optically-allowed transition in an atom or molecule, followed by the subsequent isotropic emission of radiation (fluorescence). However, this two-step description belies the complexities of the process which become apparent when one considers aspects such as saturation, inhomogeneous broadening, and energy-transfer mechanisms. The traditional approach to introducing these concepts is to begin with a *two-level model* of the absorber, which may be either an atom or a molecule, and gradually increase the degree of sophistication by adding more processes (*e.g.*, energy transfer, quenching), which generally translates into adding more levels to the model. Nevertheless, the two-level model encompasses the majority of the important features of laser-induced fluorescence for the situation in which it usually applied, *i.e.*, the weak-excitation (low laser irradiance) limit.

Although originally applied only as a point-wise technique, LIF has been extended to an imaging method by utilising a sheet of laser light and a two-dimensional detection system (typically intensified charge-coupled devices, or ICCDs). The basic principles remain the same though. A laser light source is tuned to a resonance transition in an absorber and a certain fraction of the absorbing state population is transferred to an excited state. The absorber then spontaneously radiates after some lifetime characteristic of the excited state, returning either to the original level or to some intermediate level. This radiation, or fluorescence, is generally isotropic, although in some cases it can show a certain degree of anisotropy as will be discussed later. The excited absorber will often be de-excited by other com-

peting mechanisms, both radiative and non-radiative. For example, if the excited absorber undergoes a collision then a non-radiative transition may occur, effectively quenching the fluorescence. This is known as *collisional quenching*. Other competing processes will be discussed below, but generally speaking, collision-induced transitions add a temperature- and species-dependent factor to the fluorescence signal which complicates interpretation and decreases the magnitude of the signal. Much of the theoretical development involves producing a closed-form solution to the equation describing the fluorescence signal, and developing strategies to isolate the signal dependencies on specific physical parameters, such as temperature, concentration or velocity.

There are two alternative approaches to the theoretical description of the LIF process. The first is the quantum-mechanical formulation, which involves solving the density matrix for the two-level absorber (Greenstein and Bates 1975, Daily 1977*b*, Yariv 1988). Collisional processes and spontaneous emission are included in terms of phenomenological decay constants. The alternative approach is to use a semi-classical rate equation analysis first put forward by Piepmeier (1972) and later elaborated on by many authors. The latter procedure is easier to conceptualise and solve mathematically, but has a limited range of validity and may omit possible coherence effects (Altkorn and Zare 1984). The semi-classical approach will be taken here and will include a discussion of the validity of the rate-equation analysis.

The fluorescence-signal equation simplifies in the limits of high and low laser irradiances. In the low-irradiance limit, the fluorescence signal varies linearly with laser irradiance and allows easy interpretation of experimental results. In the high irradiance limit, the absorption transition becomes *saturated* and the fluorescence is characterised by its reduced dependence on irradiance and collisional quenching (Piepmeier 1972, Daily 1977*a*). However, accurate saturated LIF measurements are difficult to achieve in practice due to the inability to ensure complete saturation across the entire spatial and temporal profiles of the laser pulse. Signal from the peripheral regions can contribute significantly to the total signal unless elaborate measures are taken. Apertures can be used to make the spatial profile more like a top-hat, while sampling only the fluorescence from that part of the temporal profile where saturation occurs effectively filters the pulse in the time-domain as well (see Eckbreth (1996) for a more detailed discussion of saturated LIF and appropriate references).

In this chapter, we will develop an equation describing the fluorescence signal and demonstrate how the temperature dependence of the signal can be isolated. We begin with the two-level model and gradually increase its complexity. Shock-tunnel flows cover a wide range of conditions with large variations in collision rates and quenching. For the case of combustion research, most of the current literature is concerned with atmospheric-pressure conditions which have relatively high quenching rates. Approximations to the fluorescence equations which are often made in these high-quenching environments are not valid in the low pressure and temper-

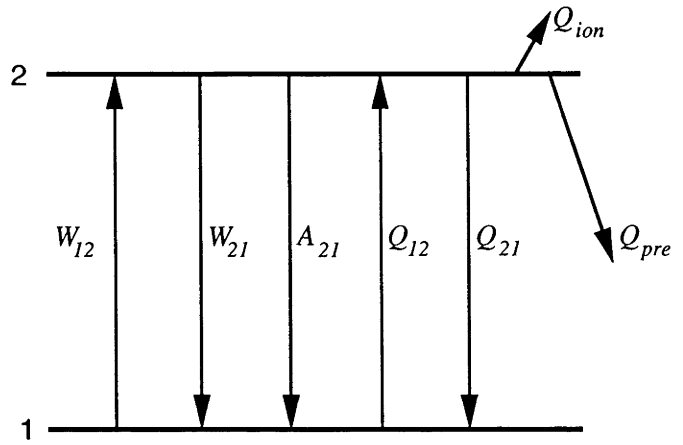

Figure 2.1: Simple two level energy diagram.

ature freestream of shock tunnel. Therefore, there is an attempt to maintain the generality of the theoretical description, especially in the early sections, but towards the end of the chapter we will tend to be more specific about the current application, in particular the use of nitric oxide for fluorescence imaging and thermometry.

2.2 Two-Level Model

Consider the simple two-level energy diagram in Fig. 2.1. Shown are the *rate constants* for various processes which can cause transitions between the levels. They are:

- W_{12} and W_{21} are the rate constants for stimulated absorption and stimulated emission, respectively. These rate constants are related to the incident laser irradiance I_ν and the Einstein B coefficients ($W_{12} \propto B_{12} I_\nu$) which will be elaborated on in the next section.
- Q_{12} and Q_{21} are the collisional excitation and quenching rate constants.
- Q_{pre} and Q_{ion} are the predissociation and photo-ionisation rate constants.
- A_{21} corresponds to spontaneous emission.

The transition rate [s^{-1}] for each process is given by the product of the rate constant and the population density of the level from which the transition originated. The population densities [cm^{-3}] are given by N_1 and N_2 respectively, and therefore the transition rates are $N_1 W_{12}$, $N_2 W_{21}$ etc.

The rate equations for the this two-level system are given by adding up the transition rates into and out of each level (Eckbreth 1996):

$$\frac{dN_1}{dt} = -N_1(W_{12} + Q_{12}) + N_2(W_{21} + A_{21} + Q_{21}) \tag{2.1}$$

$$\frac{dN_2}{dt} = N_1 W_{12} - N_2(W_{21} + A_{21} + Q_{21} + Q_{\text{pre}} + Q_{\text{ion}}) \ . \tag{2.2}$$

To solve these equations we first make the following simplifying assumptions:

1. Collisional excitation Q_{12} is negligible, which is a good assumption for transitions in the visible and ultraviolet regions.
2. Q_{pre} and Q_{ion} are also negligible, which is commonly the situation in most PLIF experiments unless specifically chosen otherwise.
3. The population of the excited state is negligible before the laser pulse. *i.e.*, $N_2(t < 0) = 0$. This is reasonable, considering assumption 1.
4. The laser pulse is a top-hat function in the temporal domain and has duration given by t_{las} and irradiance I_ν. This can be generalised to an arbitrary laser temporal profile, but the top hat function allows the time integral to be easily solved and suffices to elucidate the important features of the two-level model.

It follows from the second assumption that we are dealing with a *closed* system and therefore $N_1 + N_2 = constant = N_1^0$, where N_1^0 is the population of state 1 in the unperturbed system. The rate equations are solved directly by substituting $N_1 = N_1^0 - N_2$ and $r = W_{12} + W_{21} + A_{21} + Q_{21}$ into Eq. 2.2 and integrating to give

$$N_2(0 < t < t_{\text{las}}) = \frac{W_{12}N_1^0}{r}(1 - e^{-rt}) \ . \tag{2.3}$$

Hence, it can be seen that the population of the excited state approaches a steady state with a time constant given by r^{-1}. The fluorescence rate is equal to $N_2(t)A_{21}$, so if we integrate for the duration of the laser pulse ($0 < t < t_{\text{las}}$) we find

$$\begin{aligned} F_{0<t<t_{\text{las}}} &= \int_0^{t_{\text{las}}} N_2(t)A_{21}dt \\ &= \frac{W_{12}N_1^0A_{21}}{r}\int_0^{t_{\text{las}}}(1 - e^{-rt})dt \\ &= \frac{W_{12}N_1^0A_{21}}{r}t_{\text{las}}\left[1 - \frac{(1 - e^{-rt_{\text{las}}})}{rt_{\text{las}}}\right] \ , \end{aligned} \tag{2.4}$$

which represents the total number of fluorescence transitions [cm^{-3}] during the laser pulse.

After the laser pulse, the population density N_2 decays from a value of $N_2(t_{\rm las})$ with a time constant of $(A_{21}+Q_{21})^{-1}$. Hence we have

$$N_2(t > t_{\rm las}) = N_2(t_{\rm las})e^{-(A_{21}+Q_{21})t} \ . \tag{2.5}$$

The integrated fluorescence rate after the laser pulse ($t > t_{\rm las}$) is

$$\begin{aligned} F_{t>t_{\rm las}} &= \int_{t_{\rm las}}^{\infty} N_2(t)A_{21}dt \\ &= N_2(t_{\rm las})A_{21}\int_{t_{\rm las}}^{\infty} e^{-(A_{21}+Q_{21})t}dt \\ &= N_2(t_{\rm las})\frac{A_{21}}{A_{21}+Q_{21}} \\ &= \frac{W_{12}N_1^0A_{21}}{r}t_{\rm las}\left[\frac{(1-e^{-rt_{\rm las}})}{t_{\rm las}(A_{21}+Q_{21})}\right] \ , \end{aligned} \tag{2.6}$$

where in the last step we have substituted for $N_2(t_{\rm las})$ using Eq. 2.3. The total number of fluorescence transitions for the pulse is obtained by adding these two results together to give

$$F_{\rm Total} = \frac{W_{12}N_1^0A_{21}}{r}t_{\rm las}\left\{\left[1-\frac{(1-e^{-rt_{\rm las}})}{rt_{\rm las}}\right]+\left[\frac{(1-e^{-rt_{\rm las}})}{t_{\rm las}(A_{21}+Q_{21})}\right]\right\} \ . \tag{2.7}$$

It is useful at this stage to introduce the saturation spectral irradiance $I^{\nu}_{\rm sat}$ via the relation

$$\begin{aligned} r &= W_{12}+W_{21}+A_{21}+Q_{21} \\ &= (A_{21}+Q_{21})\left(1+\frac{W_{12}+W_{21}}{A_{21}+Q_{21}}\right) \\ &= (A_{21}+Q_{21})\left(1+\frac{I_{\nu}}{I^{\nu}_{\rm sat}}\right) \ , \end{aligned} \tag{2.8}$$

where

$$I^{\nu}_{\rm sat} = \frac{A_{21}+Q_{21}}{B_{12}+B_{21}} \ . \tag{2.9}$$

If we now substitute for r and note that $(A_{21}+Q_{21}) = r(1+I_{\nu}/I^{\nu}_{\rm sat})^{-1}$, Eq. 2.7 becomes

$$F_{\rm General} = W_{12}N_1^0\frac{A_{21}}{A_{21}+Q_{21}}\left(1+\frac{I_{\nu}}{I^{\nu}_{\rm sat}}\right)^{-1}t_{\rm las}\left[1+\frac{(1-e^{-rt_{\rm las}})}{rt_{\rm las}}\frac{I_{\nu}}{I^{\nu}_{\rm sat}}\right] \ , \tag{2.10}$$

which is our general analytic solution to the two-level model.

2.2.1 Linear Solution

In Eq. 2.10, the term $(1 - e^{-rt_{las}})/rt_{las}$ approaches unity for values of $rt_{las} \ll 1$ and approaches zero for values of $rt_{las} \gg 1$. Hence it follows that, in the low-irradiance limit ($I_\nu \ll I^\nu_{sat}$),

$$\frac{(1 - e^{-rt_{las}})}{rt_{las}} \frac{I_\nu}{I^\nu_{sat}} \rightarrow 0 \tag{2.11}$$

faster than $I_\nu / I^\nu_{sat} \rightarrow 0$. In the low-irradiance limit the solution then becomes

$$F_{Linear} = W_{12} N_1^0 \frac{A_{21}}{A_{21} + Q_{21}} t_{las} \ , \tag{2.12}$$

which is true for all values of rt_{las}. This relation can also be derived by considering a simple absorption-fluorescence model, where $W_{12}N_1^0 t_{las}$ is the number of absorption transitions, and $A_{21}/(A_{21}+Q_{21})$ represents the ratio of de-excitation transitions that produce fluorescence photons to the total number of de-excitation transitions. This last factor is often termed the fluorescence yield, or the Stern-Volmer function (Mitchell and Zemansky 1934).

2.2.2 Steady-State Solutions

The steady-state solution is often applied to more sophisticated models where it is necessary to help solve the set of differential equations describing the population changes in the levels. We didn't need to invoke it for this simple two-level model but it is often applied in combustion environments to simplify the general solution. The steady-state approximation assumes that the excited-state population has reached a constant value which occurs when the laser pulse is much longer than the rate constant r^{-1}. In other words, when $rt_{las} \gg 1$, the term $(1 - e^{-rt_{las}}) \rightarrow 1$ in Eq. 2.7, and the steady state solution becomes

$$F_{SS} = \frac{W_{12} N_1^0 A_{21}}{r} t_{las} \left[1 + \frac{1}{t_{las}(A_{21} + Q_{21})} \frac{1}{(1 + I^\nu_{sat}/I_\nu)} \right] \ . \tag{2.13}$$

In the low-irradiance limit, the bracketed term approaches unity and this equation becomes the simple linear fluorescence equation Eq. 2.12. However, in the strong-saturation limit ($I_\nu \gg I^\nu_{sat}$) it becomes

$$F_{SS-saturation} = \frac{W_{12} N_1^0 A_{21}}{r} t_{las} \left[1 + \frac{1}{t_{las}(A_{21} + Q_{21})} \right] \ . \tag{2.14}$$

The term in brackets is the same as that given by Paul et al. (1994) to describe the signal collected after the laser pulse. However, from the analysis presented here this factor appears only to be important in the saturating regime, and the term in brackets in Eq. 2.13 becomes negligible in the low-irradiance limit. If the fluorescence equation of Paul et al. (1994) is used in the steady-state regime, the extra term may cause only a small error. If used in low quenching environments it may cause significant discrepancy. A graphical comparison of these results is presented in Fig. 2.2. Typical values for the current experiments are used. The steady-state solution differs from the general solution in the low quenching case because $rt_{\text{las}} < 1$ for non-saturating irradiance levels. The conclusion from this analysis is, therefore, that in the weak-excitation limit the extra term of Paul et al. (1994) should be omitted and the simple linear fluorescence equation used.

2.2.3 Collection Efficiency and Fluorescence Signal

In general, the fluorescence is emitted isotropically but the optics and detector used to measure the fluorescence will only collect a certain portion. The collected fluorescence signal S_f [J] is obtained by multiplying the total number of fluorescence transitions [cm^{-3}] by the energy per photon, the collection efficiency of the optical-detection system and the interaction volume size. Therefore the general solution for our simple two-level model is

$$S_f = F_{\text{General}} h\nu c \frac{\Omega}{4\pi} \eta \ell a \ , \tag{2.15}$$

where h [Js] is Planck's constant; ν [cm^{-1}] is the frequency of the fluorescence; c is the speed of light [cm s^{-1}]; Ω is the solid angle subtended by the detector; η is the detection efficiency; ℓ [cm] is the length of the interaction volume in the direction of the beam; and a [cm^2] is the cross sectional area of the beam. A more practical quantity to calculate might be the number of fluorescence photons N_{p} detected, which would be given by the above equation divided by the energy per photon. Hence, in the low irradiance limit, we have

$$N_{\text{p}} = W_{12} N_1^0 \frac{A_{21}}{A_{21} + Q_{21}} t_{\text{las}} \frac{\Omega}{4\pi} \eta \ell a \ . \tag{2.16}$$

2.3 Absorption

In the previous section, the stimulated absorption and emission rates, W_{12} and W_{21}, were related to the Einstein B coefficients and the spectral irradiance without any concern for spectral lineshapes of the irradiation source or absorption transition.

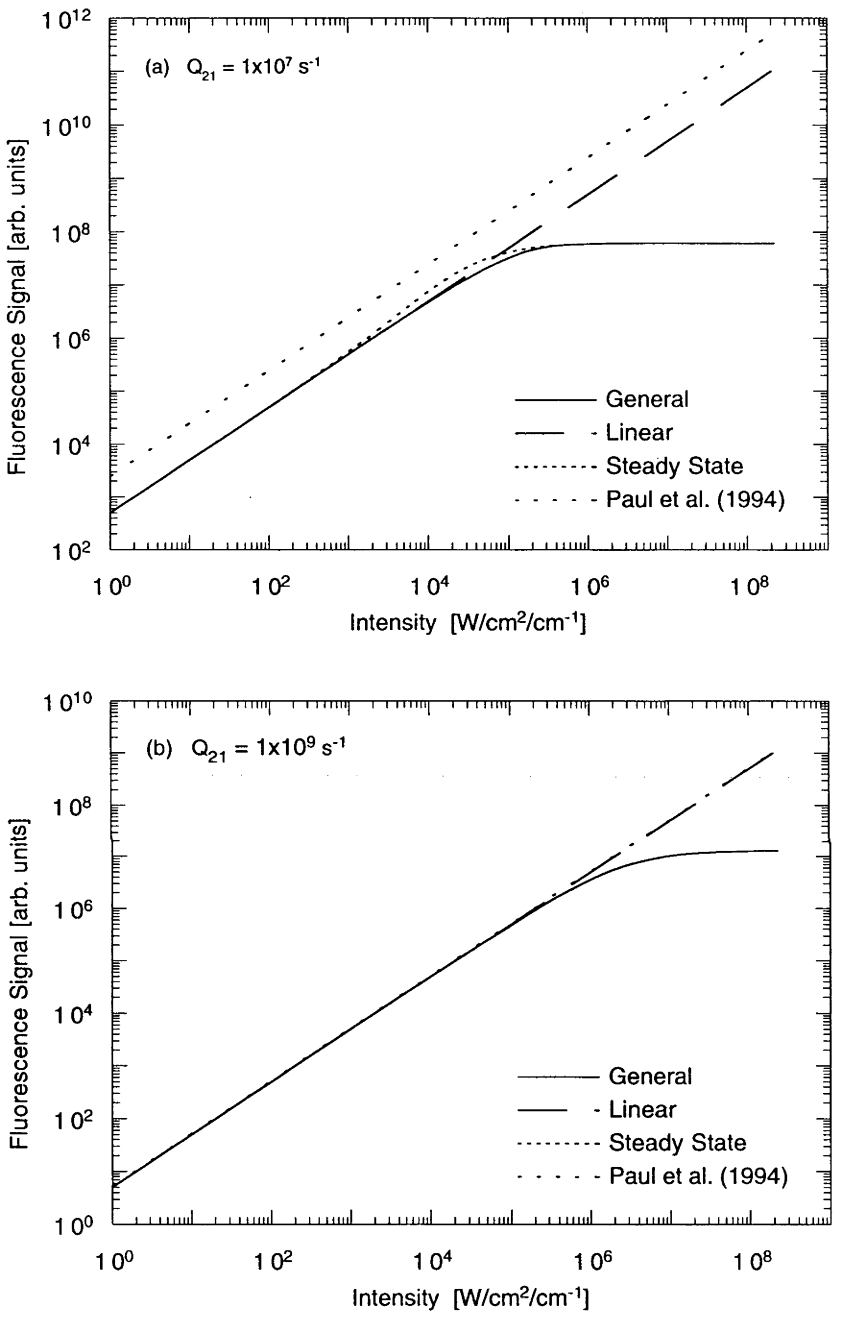

Figure 2.2: Comparison between the general analytic solution for the simple two-level model and various approximations. Calculations have been performed for the values: $B_{12} = B_{21} = 200$ s^{-1}(W/cm^2/cm^{-1})$^{-1}$; $A_{21} = 1\times10^5$ s^{-1}; $t_{las} = 25$ ns; and $N_1^0 = 1\times10^{10}$ cm^{-3}. The calculations are for two different quenching rates: (a) $Q_{21} = 1\times10^7$ s^{-1} and (b) $Q_{21} = 1\times10^9$ s^{-1}.

When these lineshapes are of the same order of magnitude such that neither can be approximated as monochromatic or constant-valued, a more sophisticated treatment is necessary to include the degree of spectral overlap between the two entities. In subsequent sections, the spectral dependence of parameters used to describe the process of absorption will be derived, leading to the definition of the spectral-overlap integral.

2.3.1 Einstein Probability Coefficients

Einstein (1917) introduced the probability coefficients for stimulated absorption (B_{12}), stimulated emission (B_{21}) and spontaneous emission (A_{21}). The coefficients were defined such that the probability of an absorption transition from level 1 to level 2 in the time interval dt is given by $B_{12}\rho(\nu_{12})dt$, where $\rho(\nu_{12})$ [J m^{-3}Hz^{-1}] is the spectral density of radiation at the frequency ν_{12} [Hz] corresponding to the transition. The B coefficient thus defined has units of inverse spectral radiation density per unit time [s^{-1}(J m^{-2} Hz^{-1})$^{-1}$]. Einstein also derived the following important relations between the coefficients (Thorne 1988):

$$g_1 B_{12} = g_2 B_{21} \tag{2.17}$$

$$A_{21} = \frac{8\pi h\nu^3}{c^3} B_{21} = \frac{g_1}{g_2}\frac{8\pi h\nu^3}{c^3} B_{12} \,, \tag{2.18}$$

where g_1 and g_2 are the degeneracies of the levels, h [Js] is Planck's constant and c [ms^{-1}] is the speed of light. These relations were derived by Einstein assuming thermodynamic equilibrium, but since the coefficients are intrinsic atomic properties, they hold even when thermodynamic equilibrium does not exist.

It is also important to realise that the probability coefficients defined above are in terms of spectral radiation density, whereas later definitions (Milne 1924) are in terms of isotropic intensity and require the B coefficients to be redefined accordingly. Altkorn and Zare (1984) utilise *directional* probability coefficients for the LIF process which allows them to model the interaction of directional and polarised radiation with molecules having a specific orientation. Thorne (1988, p. 290) discusses the various units used to define B coefficients in the literature and the surreptitious way in which factors of 2π can hide in the expressions. Although there is a trend towards the use of SI units, the spectroscopic quantity wavenumber (or frequency) in cm^{-1} still has a certain appeal in spectroscopy and will be used in the remaining portion of this monograph.[†] In the work presented here, we will consider the Einstein B probability coefficients [s^{-1}(W/cm^2/cm^{-1})$^{-1}$] defined in terms of the spectral irradiance I_ν [W/cm^2/cm^{-1}], which is the incident laser irradiance per unit frequency interval at the frequency ν [cm^{-1}]. Hence, the probability per second

[†]The units of cm^{-1} has also been given the name Kayser [K]

of an absorption transition is $B_{12}I_\nu(\nu_{12})$, where $I_\nu(\nu_{12})$ is the spectral irradiance at the transition frequency. Finally, the relationship between the B coefficient defined in terms of spectral density (SI units) and that in terms of spectral irradiance (spectroscopic units) is given by

$$B\ [\mathrm{s}^{-1}(\mathrm{W/cm^2/cm^{-1}})^{-1}] \times 10^{-6} \times c^2 = B\ [\mathrm{s}^{-1}(\mathrm{Jm^{-2}\ Hz^{-1}})^{-1}]\ , \tag{2.19}$$

where c [cm s^{-1}] is the speed of light and the relation $I_\nu = \rho_\nu c$ has been used to convert spectral density to spectral irradiance. Rewriting Eq. 2.18 in spectroscopic units gives

$$A_{21} = 8\pi hc^2\nu^3 B_{21} = \frac{g_1}{g_2} 8\pi hc^2\nu^3 B_{12}\ . \tag{2.20}$$

2.3.2 The Absorption Coefficient

When a collimated beam of light falls on an absorbing medium, the power absorbed is proportional to the incident spectral irradiance I_ν and the distance traversed, dx [cm]. The constant of proportionality is known as the absorption coefficient k_ν [cm^{-1}] and is defined by the relation (Thorne 1988)

$$-dI_\nu = k_\nu I_\nu dx\ . \tag{2.21}$$

The transmitted spectral irradiance I_ν of a beam of light having passed through a *uniform* absorbing medium of length ℓ [cm] is obtained by integrating Eq. 2.21 to give

$$I_\nu = I_0 e^{-k_\nu \ell}\ , \tag{2.22}$$

where I_0 is the incident spectral irradiance. The spectral absorption coefficient can be rewritten as

$$k_\nu = S_{12} Y(\nu)\ , \tag{2.23}$$

where S_{12} [cm^{-2}] is the line-strength factor for the transition and $Y(\nu)$ [cm] is the lineshape function, normalised such that

$$\int Y(\nu) d\nu = 1\ . \tag{2.24}$$

With k_ν expressed in this manner, S_{12} contains only terms relating to the transition probability and is independent of lineshape effects. In the next section we will examine how $Y(\nu)$ is effected by various broadening processes.

To derive an expression for k_ν, we begin by considering our simple two-level absorber with a lower-level population N_1 and upper-level population N_2. We use the same collimated beam of light described above traversing a distance dx with spectral irradiance I_ν between ν and $\nu + d\nu$. Of the total N_1 absorbers in the lower level only δN_1 absorbers are capable of absorbing in the frequency range ν to $\nu + d\nu$. The lineshape function can be used to describe this fraction so we can write $\delta N_1 = N_1 Y(\nu) d\nu$.[†] In the volume of length dx [cm] and unit area there are $\delta N_1 dx$ absorbers and so the number of transitions per second is $\delta N_1 dx B_{12} I_\nu$. The energy per photon is $h\nu c$. Therefore, neglecting spontaneous emission because it is isotropic, but including stimulated emission ($\delta N_2 = N_2 Y(\nu) d\nu$), the amount of energy absorbed in the volume element is

$$\begin{aligned} -dI_\nu d\nu &= \delta N_1 dx B_{12} I_\nu h\nu c - \delta N_2 dx B_{21} I_\nu h\nu c \\ &= (N_1 B_{12} - N_2 B_{21}) h\nu c Y(\nu) I_\nu dx d\nu \\ &= N_1 B_{12} h\nu c \left(1 - \frac{N_2}{N_1}\frac{g_1}{g_2}\right) Y(\nu) I_\nu dx d\nu \ , \end{aligned} \tag{2.25}$$

where we have used the relation $g_2 B_{21} = g_1 B_{12}$ to eliminate B_{21}. Dividing through by $I_\nu dx d\nu$ and comparing with Eq. 2.21 we find

$$\begin{aligned} k_\nu &= \frac{-dI_\nu}{I_\nu}\frac{1}{dx} \\ &= N_1 B_{12} h\nu c \left(1 - \frac{N_2}{N_1}\frac{g_1}{g_2}\right) Y(\nu) \ . \end{aligned} \tag{2.26}$$

Hence, from our previous definition of $k_\nu = S_{12} Y(\nu)$, we have

$$S_{12} = N_1 B_{12} h\nu c \left(1 - \frac{N_2}{N_1}\frac{g_1}{g_2}\right) \ , \tag{2.27}$$

where the term in parentheses is due to stimulated emission and is only significant when there is appreciable population in the excited state.

The excited-state population can become appreciable for high irradiance levels and manifests itself as a reduced absorption coefficient from that in the low-irradiance case. This is known as *saturation* and is characterised by a lineshape which appears broadened, which is termed saturation broadening, or power broadening. At very high irradiance levels the absorption coefficient approaches zero, and the absorbing medium appears transparent. Note that the homogeneous linewidth has not really been broadened in any fundamentally new way (Seigman 1986, p. 295) but rather appears to be broadened because of the reduced absorption coefficient near line centre. It is important to note that saturation broadening is only observed when

[†] $N_1 Y(\nu) d\nu$ assumes that the transition is homogeneously broadened. See Sect. 2.3.6 for the case of inhomogeneously broadened transitions.

the exciting irradiance can spectrally resolve the transition (*e.g.*, with a narrowband laser).

Assuming the excited-state population is negligible we can integrate k_ν over the absorption line, and neglecting the slight variation in ν (in S_{12}) across the line, we arrive at

$$\begin{aligned} \int k_\nu d\nu &= S_{12} \int Y(\nu) d\nu = S_{12} \\ &= N_1 B_{12} h\nu c \,, \end{aligned} \tag{2.28}$$

where we have used the normalisation condition $\int Y(\nu)d\nu = 1$. Equation 2.28 expresses the very important result that the integral of the absorption coefficient k_ν over the line is determined by the line-strength and is independent of the lineshape. This result has been used extensively in the past for measuring line-strengths from absorption measurements (Huber and Sandeman 1986).

2.3.3 Line Broadening and Shifting Processes

Spectral line broadening is usually observed when absorption or emission is measured as a function of frequency. There are two main classes of broadening mechanisms: homogeneous and inhomogeneous. For *homogeneous* broadening, the absorbers can be considered indistinguishable and each have the same transition energy. Natural broadening and collision broadening are examples of this class and will be considered below. Homogeneous broadening is characterised by a Lorentzian lineshape. For *inhomogeneous* broadening, the absorbers are distinguishable, as in the case of Doppler broadening where each absorber has a slightly different transition frequency. The transition frequencies are Doppler-shifted due to the finite velocity of the absorbers in the direction of the observer. Doppler broadening is characterised by a Gaussian lineshape due to the Maxwell velocity distribution of the absorbers in the gas.

Spectral line broadening is covered in virtually all texts on spectroscopy and quantum electronics and only the relevant points are presented here (Mitchell and Zemansky 1934, Thorne 1988, Yariv 1988, Demtröder 1996). The three main line broadening processes that we will consider are:

1. *Natural* broadening due to the finite lifetime of the excited state. This broadening can also be derived from considerations relating to the Heisenberg Uncertainty Principle. It is significantly smaller than either of the following broadening processes and so can be ignored in most cases. When it cannot be ignored, it is usually accounted for by adding the FWHM due to natural broadening ($\Delta\nu_N$) to the other homogeneous broadening widths, such as col-

lision broadening ($\Delta\nu_c$). The Lorentzian lineshape used for homogeneously broadened transitions, with FWHM $\Delta\nu_H$ is given by

$$g_H(\nu) = \frac{\Delta\nu_H}{2\pi} \frac{1}{(\nu-\nu_0)^2 + (\Delta\nu_H/2)^2} , \tag{2.29}$$

where ν_0 is the centre frequency of the transition.

2. *Doppler* broadening due to the thermal motion of the absorbers. The Gaussian lineshape function $g_D(\nu)$, with FWHM $\Delta\nu_D$, is given by

$$g_D(\nu) = \frac{2(\ln 2)^{1/2}}{\pi^{1/2}\Delta\nu_D} \exp\left[\frac{-4(\ln 2)(\nu-\nu_0)^2}{\Delta\nu_D^2}\right] \tag{2.30}$$

$$\Delta\nu_D = 2\nu_0\sqrt{\frac{2kT}{Mc^2}\ln 2} , \tag{2.31}$$

where ν_0 is the centre frequency corresponding to a stationary absorber, M is the mass of the absorber, c is the speed of light, k is Boltzmann's constant and T is the temperature.

3. *Collision* broadening (or pressure broadening) due to collisions with other atoms or molecules. Associated with the collision broadening width $\Delta\nu_c$, there is a collision induced shift $\Delta\nu_s$ in the centre frequency and also an asymmetry of lineshape. The various theories for collision broadening are reviewed, *e.g.*, by Thorne (1988), but in the current investigation it is simpler and more accurate to use empirically derived results.† In particular, collision widths and shifts for a gas mixture of chemical species are determined by using the empirical relationships (Chang et al. 1992, Di Rosa 1994)

$$\Delta\nu_c = P\sum_i(\chi_i\, 2\gamma_i) \tag{2.32}$$

$$\Delta\nu_s = P\sum_i(\chi_i\, \delta_i) , \tag{2.33}$$

where P [atm] is the total pressure, χ_i is the mole fraction, $2\gamma_i$ [cm^{-1} atm^{-1}] is the FWHM collision width per unit pressure, and δ_i [cm^{-1} atm^{-1}] is the collision shift per unit pressure. The summation is over all chemical species represented by i. The temperature dependence of $2\gamma_i$ and δ_i can be expressed with reference to ${2\gamma_i}^{T_0}$ and ${\delta_i}^{T_0}$, which are the values at the known temperature T_0, by

$$2\gamma_i = 2\gamma_i^{T_0}\left(\frac{T_0}{T}\right)^{m_i} \tag{2.34}$$

$$\delta_i = \delta_i^{T_0}\left(\frac{T_0}{T}\right)^{n_i} , \tag{2.35}$$

†See also Di Rosa (1996) for an extensive review of the theoretical aspects of collision broadening.

where the exponents m and n have been determined from experiments for various perturbing species.

When the processes of Doppler and collision broadening are considered as independent broadening mechanisms, we can perform a convolution of their respective lineshape functions. The resulting integral, which was first solved by Voigt, is given by (Mitchell and Zemansky 1934, Eckbreth 1996)

$$Y(\nu) = \frac{2}{\Delta\nu_{\mathrm{D}}}\sqrt{\frac{\ln 2}{\pi}}V(a,x) \ , \tag{2.36}$$

where the Voigt function $V(a,x)$ and parameters a and x are given by

$$V(a,x) = \frac{a}{\pi}\int_{-\infty}^{\infty}\frac{e^{-y^2}}{a^2+(x-y)^2}dy \tag{2.37}$$

$$a = \sqrt{\ln 2}\frac{\Delta\nu_{\mathrm{H}}}{\Delta\nu_{\mathrm{D}}} \tag{2.38}$$

$$x = 2\sqrt{\ln 2}\frac{(\nu-\nu_0)}{\Delta\nu_{\mathrm{D}}} \ . \tag{2.39}$$

The Voigt function $V(a,x)$ cannot be solved analytically but is usually calculated using numerical methods (Humlícek 1979).

2.3.4 The Spectral-Overlap Integral

So far we have considered the spectral variation of the absorption transition but not that of the irradiance. Consider the spectral irradiance described by

$$I_\nu = IL(\nu) \ , \tag{2.40}$$

where I [W cm^{-2}] is the irradiance and $L(\nu)$ [1/cm^{-1}] is the lineshape function normalised such that

$$\int L(\nu)d\nu = 1 \ , \tag{2.41}$$

and hence

$$\int I_\nu d\nu = \int IL(\nu)d\nu = I \ . \tag{2.42}$$

Inserting this expression for I_ν into Eq. 2.21 and integrating over the absorption line, we get the total power absorbed in the line to be[†]

$$\begin{aligned} -\Delta I = \int -dI_\nu d\nu &= \int_\nu k_\nu I L(\nu) dx d\nu \\ &= \int_\nu S_{12} I Y(\nu) L(\nu) dx d\nu \\ &= S_{12} I dx \int_\nu Y(\nu) L(\nu) d\nu \\ &= S_{12} G I dx \ , \end{aligned} \tag{2.43}$$

where

$$G = \int Y(\nu) L(\nu) d\nu \tag{2.44}$$

is the spectral-overlap integral. The overlap integral G [$1/\text{cm}^{-1}$] represents the degree of overlap between the irradiance lineshape and the absorption line. We may now write a more accurate expression for the stimulated absorption and emission rate constants. Following the same logic that led to Eq. 2.25, we can write the number of transitions per second to be

$$\begin{aligned} N_1 W_{12} &= \int N_1 Y(\nu) B_{12} I_\nu d\nu \\ &= N_1 B_{12} I \int Y(\nu) L(\nu) d\nu \\ &= N_1 B_{12} I G \end{aligned} \tag{2.45}$$

and therefore the rate constants for stimulated absorption and emission are

$$\begin{aligned} W_{12} &= B_{12} I G \\ W_{21} &= B_{21} I G \ . \end{aligned} \tag{2.46}$$

The overlap integral as defined by Eq. 2.44 has a vague physical interpretation. To address this Partridge and Laurendeau (1995) introduced the dimensionless-overlap integral Γ by defining the spectral irradiance as

$$I_\nu = I_\nu^0 L'(\nu) \ , \tag{2.47}$$

[†]Line 3 of this analysis assumes that S_{12} is constant across the line and can therefore be taken out of the integral. This is only true for weak excitation according to Eq. 2.28.

where I_ν^0 [W/cm^2/cm^{-1}] is the normalised spectral irradiance and $L'(\nu)$ is the independent dimensionless spectral distribution function, normalised such that

$$\int L'(\nu)d\nu = \Delta\nu_{\text{las}} \,, \tag{2.48}$$

where $\Delta\nu_{\text{las}}$ [cm^{-1}] is the FWHM of the irradiance spectral distribution function. Hence, we define the dimensionless-overlap integral as

$$\Gamma = \int Y(\nu)L'(\nu)d\nu \tag{2.49}$$

and note that $\Gamma = \Delta\nu_{\text{las}}G$. I_ν^0 can be calculated from the measured pulse energy E [J], the beam cross-sectional area a [cm^2], the pulse duration t_{las} [s] and the FHWM $\Delta\nu_{\text{las}}$ using $I_\nu^0 = E/(a\Delta\nu_{\text{las}}t_{\text{las}})$. The irradiance I is given simply by $I = E/(at_{\text{las}})$.

The dimensionless overlap integral can be interpreted as the ratio of the total photon absorption rate in the actual broadened system to that which would exist in the monochromatic limit. The monochromatic limit, for which $\Gamma = 1$, is defined as a monochromatic irradiance interacting with a monochromatic absorption line. Hence Γ varies between 0 and 1 depending on the degree of overlap and is more readily interpreted than the previous formulation G. In the equations where it appears above, $\Gamma/\Delta\nu_{\text{las}}$ can easily be substituted for G.

In the limit that the absorption line FWHM $\Delta\nu_{\text{a}} \ll \Delta\nu_{\text{las}}$ (*i.e.*, the broadband excitation case) we find that $G \to L(\nu_{\text{a}}) \approx 1/\Delta\nu_{\text{las}}$, where $L(\nu_{\text{a}})$ is the value of the irradiance lineshape function at the frequency (ν_{a}) of the monochromatic absorption line. In the other extreme (*i.e.*, the monochromatic excitation case) $\Delta\nu_{\text{las}} \ll \Delta\nu_{\text{a}}$, we find $G \to Y(\nu_{\text{las}}) \approx 1/\Delta\nu_{\text{a}}$ where $Y(\nu_{\text{las}})$ is the value of the absorption line lineshape function at the frequency (ν_{las}) of the monochromatic irradiance. Hence Γ varies from $\Delta\nu_{\text{las}}/\Delta\nu_{\text{a}}$ to 1 in the limits of monochromatic and broadband excitation.

A narrow laser linewidth can be chosen to selectively excite a particular transition. However, the laser linewidth that gives the maximum absorption and hence the maximum fluorescence signal may also be a criterion of importance. Greenstein and Bates (1975) discuss these points and indicate that an irradiation linewidth somewhere between the Doppler and Lorentz widths provides the maximum absorption coefficient.

2.3.5 The Spectrally-Integrated Absorption Coefficient

If we consider a beam of irradiance I [W cm^{-2}] passing through an absorbing medium, we can define the line-integrated absorption coefficient according to

$$-\Delta I = k_{\text{int}} I dx \tag{2.50}$$

and equate this with Eq. 2.43 to give

$$k_{\text{int}} = S_{12}G = G \int k_\nu d\nu \ , \tag{2.51}$$

where we have assumed the weak excitation limit (see Eq. 2.28). From Eq. 2.51, we notice that $k_{\text{int}} \neq \int k_\nu d\nu$ but that G acts as a proportionality constant. If the irradiance is strong enough, saturation can occur, and we can write k_{int} as

$$k_{\text{int}} = \frac{k^0_{\text{int}}}{1 + I/I_{\text{sat}}} \ , \tag{2.52}$$

where $k^0_{\text{int}} = S^0_{12}G$ is the unsaturated integrated-absorption coefficient, and I_{sat} [W cm^{-2}] is the saturation irradiance. The unsaturated line-strength is given by $S^0_{12} = N_1 B_{12} h\nu c$. The saturation irradiance can be written as (Seigman 1986, p. 293)

$$I_{\text{sat}} = \frac{I}{W_{12}\tau_{\text{eff}}} = \frac{1}{B_{12}G\tau_{\text{eff}}} \ , \tag{2.53}$$

where τ_{eff} is the effective lifetime or population recovery time. If the saturation irradiance is known for a reference transition at a known pressure and temperature, the saturation irradiances can be determined for other conditions and transitions in the same vibrational band. The effective lifetime is dependent on the rotational and vibrational energy transfer rates, the collisional-quenching rates, and the spontaneous decay rates. Neglecting spontaneous decay because it is generally much less than the collisional effects and it is also constant for transitions from the NO $A^2\Sigma^+(v'=0)$ level, τ_{eff} is proportional to the collision rate only. Therefore, $\tau_{\text{eff}} \propto \sqrt{T}/p$ where T and p are the temperature and pressure respectively (Vincenti and Kruger 1975, p. 52). Hence, we arrive at the expression

$$I_{\text{sat}} \propto \frac{p}{B_{12}G\sqrt{T}} \ , \tag{2.54}$$

which can be used to determine saturation irradiances of different transitions at different pressures and temperatures if the saturation irradiance is known for a reference transition at a known pressure and temperature. Note that Eq. 2.54 assumes that the overall collision cross-section is temperature independent.

It is observed from Eq. 2.54 that as the laser is detuned from line centre, the saturation irradiance increases through the overlap integral G which is decreasing. Variations in the overlap integral via changes in the irradiance linewidth and detuning are accounted for through the value of G, provided that the type of interaction, homogeneous or inhomogeneous, remains constant. The rate at which a transition saturates, and hence the value of I_{sat}, is dependent on the temporal, spatial, and spectral distribution of the irradiance. Saturation occurs slower in the wings of these profiles. Therefore, Eq. 2.54 is only accurate for determining I_{sat} values for the same experimental arrangement for which the reference I_{sat} measurement was performed (*i.e.*, same temporal profile, focussing optics etc.).

2.3.6 Homogeneous and Inhomogeneous Interaction

In the derivation of k_ν we described the situation when the absorbers in level 1 were distributed according to $N_1 Y(\nu)d\nu$. This derivation assumes the interaction between the irradiance and absorbers is homogeneous. That is, that each absorber is indistinguishable and has the same probability at the frequency ν as any other absorber of absorbing a photon. However, in the inhomogeneous case this is no longer true and the interaction between the radiation and the absorbers is a little more complex. Nevertheless, in the low-irradiance limit the equations for the absorption coefficient reduce to the same result, whereas in the saturation limit extra terms are needed to describe the response for the inhomogeneous case.

Killinger et al. (1976) derived expressions for the interaction of broadband and narrowband irradiances with both homogeneously and inhomogeneously broadened transitions. In particular, they included the case where the irradiance spectral profile is made up of discrete modes which are representive of cavity modes in dye lasers. They also note, for an inhomogeneously broadened transition excited by a broadband irradiance ($\Delta\nu_{\text{las}} \gg \Delta\nu_{\text{D}} \gg \Delta\nu_{\text{H}}$), that the interaction is in fact homogeneous and can be described by the same equations as for the homogeneously broadened case. This is because the irradiance profile is essentially constant over the Doppler width and so each *homogeneous packet* (Yariv 1988, p.178) interacts with the irradiation in the same manner (Greenstein and Bates 1975).

All the work presented in this thesis will assume that the interaction is homogeneous, which is a good assumption when the laser linewidth is on the same order as, or greater than, the Doppler width of the transition, which is common in PLIF experiments. Also, in the weak-excitation regime, the theoretical description of the interaction between the irradiation and matter in terms of the overlap integral remains essentially correct independent of the broadening mechanism. A comprehensive treatment and a basic equation encompassing the effects mentioned is given by Yariv (1988, p. 178) but is beyond the scope of this monograph.

What are some of the implications for PLIF if the interaction *is* inhomogeneous and partially or fully saturating irradiances are used? Saturation occurs more slowly for the inhomogeneously broadened transition (Seigman 1986, p. 1182). Also, if the excitation selects only a portion of the Doppler velocity groups then only a fraction of the absorbers in the flow will be available to absorb a photon as compared with the homogeneously-broadened case. The distribution of fluorescence in a PLIF image will also be sensitive to the velocity component in the direction of the laser beam.

If the irradiance contains cavity modes with an irradiance distribution which randomly fluctuates amongst the modes, then a laser linewidth which is less than the homogeneous linewidth of the transition will minimise absorption fluctuations caused by the modes (McMillin et al. 1993). Fluctuations would then be dependent on the total irradiance of the laser which can be readily measured in experiments, whereas the distribution of irradiance amongst the modes is significantly more difficult to measure.

2.4 Collisional Energy Transfer

Collisions between atoms and molecules play an important role in the dynamics associated with absorption and emission of radiation. Apart from the line broadening mechanisms we have already discussed, collisions can cause non-radiative transitions between levels in the absorber. The simplest of these is electronic quenching, but in molecules population transfer to other levels, rotational and vibrational, can also occur. The transfer of population out of or into the laser-coupled states can have a significant influence on the saturation characteristics of the absorbing medium. Calculations of the the energy transfer rates are therefore, important in estimating saturation irradiances for LIF experiments.

Collisional quenching occurs when electronically-excited absorbers are de-excited by collisions with other atoms or molecules via non-radiative transitions. The more quenching collisions that occur, the less the fluorescence which is observed, and hence collisional quenching can significantly lower signal-to-noise ratios. The quenching may also be both temperature and rotational-level dependent, making quantitative interpretation of LIF measurements extremely difficult. However, various studies indicate that the quenching of the NO $A^2\Sigma^+$ is independent of the rotational level, which makes NO a very suitable species for thermometry applications in quenching environments (McDermid and Laudenslager 1982, Raiche and Crosley 1990).

To calculate collisional quenching rate constants, we need to sum the following expression over all the species i in the gas mixture (Eckbreth 1996, Vincenti and

Kruger 1975):

$$Q_{21} = \sum_i N_T \chi_i v_i \sigma_i \ , \tag{2.55}$$

where N_T [cm^{-3}] is the total number density; χ_i is the mole fraction of the quenching species i; σ_i [cm^2] is the quenching cross section; v_i [cm s^{-1}] is the average relative velocity for species i given by

$$v_i = \left[\frac{8kT}{\pi\mu}\right]^{\frac{1}{2}} \ , \tag{2.56}$$

where μ is the reduced mass and is given in terms of the molecular masses of the absorber (m_a) and quenching molecules (m_i) by $\mu = [m_a m_i/(m_a + m_i)]$. If we define the average molecular velocity as

$$v_a = \left[\frac{8kT}{\pi m_a}\right]^{\frac{1}{2}} \ , \tag{2.57}$$

and then collect terms independent of i and pull them outside the summation, we can rewrite Eq. 2.55 as

$$Q_{21} = N_T v_a \sum_i \chi_i \sigma_i \left[1 + \frac{m_a}{m_i}\right] \ . \tag{2.58}$$

The cross sections σ_i for various species quenching the NO $A^2\Sigma^+$ state can be calculated using the equations and coefficients given by Paul et al. (1994).

Rotational energy transfer (RET) and vibrational energy transfer (VET) are other mechanisms that can shift population out of (or into) the laser coupled states. RET and VET rate constants are calculated in an analogous way to collisional quenching, using cross section data obtained from experiments.

2.5 Multi-Level Models

Planar LIF is usually performed in the linear regime. However, in some situations background luminosity and other sources of signal interference require partial saturation of the transition in order to obtain good signal-to-noise ratios. Therefore, a knowledge of saturation irradiances is desirable to avoid saturation or to account for the deviation from linearity in partially-saturating situations. To calculate saturation irradiances it is necessary to add more levels to the two-level model to account for the processes of RET, VET and collisional quenching. Originally, multi-level

models were developed for analysing data from saturated-LIF experiments to determine species concentrations.

In the following section, we will be concerned with the population transfer dynamics in molecules, and in particular, nitric oxide. In molecules, rotational energy transfer (RET) plays an important role in redistributing population between the laser-coupled levels and other nearby rotational levels, and hence in determining the saturation properties of the transition. The two-level model previously analysed in detail remains a valid model when:

1. RET is frozen, *i.e.,* there is no transfer to nearby levels. The two levels in the two-level model represent individual rotational levels.
2. RET is infinitely fast (*i.e.,* completely relaxed) – rotational relaxation is complete and the population distribution amongst the rotational levels is described by a Boltzmann distribution. In this case the two levels represent vibrational levels.

The saturation irradiance is a minimum for the first case and a maximum in the second. Obviously, most real cases lie somewhere between the two extremes and hence RET needs to be included in the new model, a multi-level model. Vibrational energy transfer (VET) can be considered in the same way, but in general the rate of VET is an order of magnitude less than that of RET, and is ignored in the current analysis.

Berg and Shackleford (1979) used a *four-level model* to include the effects of RET. Two extra levels were added to the original two laser-coupled levels to represent all the nearby rotational levels. All of the rotational levels in the vibrational state are lumped together into a single *bath* level, with the exclusion of the rotational level probed by the laser. This model was solved using a steady-state analysis and demonstrated the importance of RET in interpreting experimental results from saturated-LIF experiments.

2.6 Numerical Models for NO

For nanosecond laser pulses and moderate laser irradiances, steady state conditions may not be achieved and temporal variations of the state population need to be modelled. We present two models here for transitions in NO. Because of spin-splitting in the NO $A^2\Sigma^+$ state, some transitions are highly overlapped and can not be resolved by typical multimode lasers. For two transitions excited simultaneously with the same spectral irradiance, we can simply add the line strengths for the two

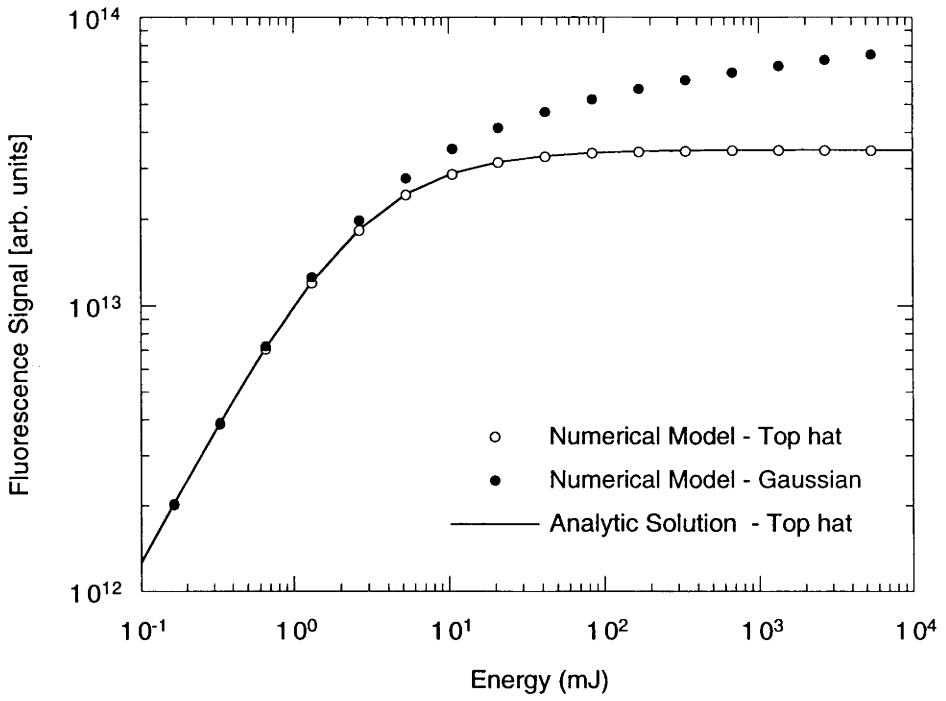

Figure 2.3: The influence that the laser pulse temporal profile has on the LIF signal saturation characteristics. A two-level numerical model was used to compare a Gaussian pulse with a top-hat shaped pulse. The analytic solution uses a top-hat profile.

transitions and treat it as a single stronger transition. This is of sufficient accuracy in the linear fluorescence regime, but with the onset of saturation one transition may begin to saturate much earlier than the other and the signal dependence on irradiance becomes more complex. Therefore, a five-level model is used to model single transitions and a six-level model is used for overlapped transitions.

2.6.1 The Effect of Laser Pulse Temporal Profile

The effects due to variation in the laser pulse shape are shown in Fig. 2.3. The two-level model has been solved numerically assuming a Gaussian shaped pulse and the results compared with the general analytic solution derived for a top-hat temporal profile (Eq. 2.10). The calculated fluorescence signals are plotted against pulse energy, rather than spectral irradiance which may vary considerably within a single pulse. In the low-irradiance limit both solutions converge to the simple linear solution implying that signal is independent of pulse shape. As the irradiance increases, the Gaussian pulse begins to saturate first because, for a given pulse energy, the peak spectral irradiance exceeds that of the top-hat pulse. However,

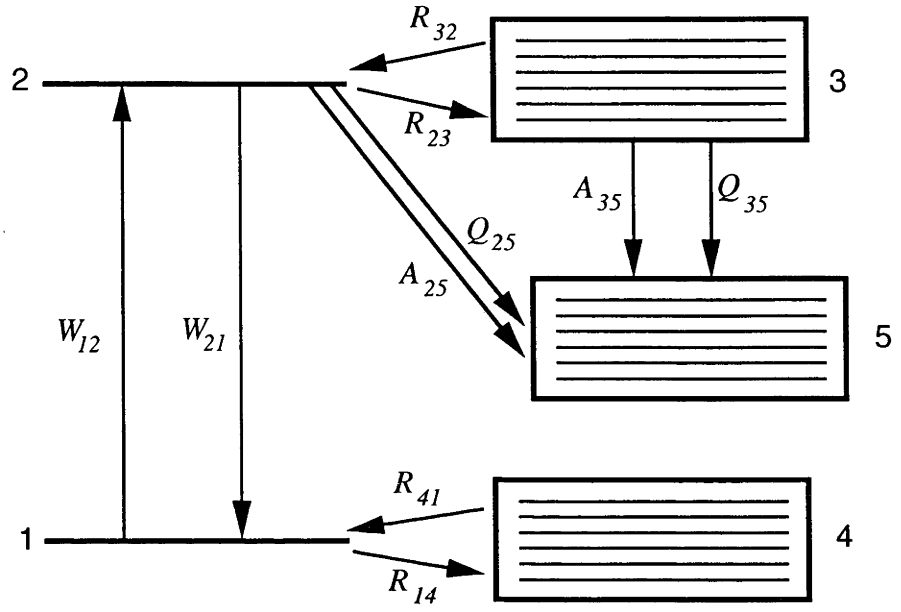

Figure 2.4: The five-level model used for modelling NO $A^2\Sigma^+ \leftarrow X^2\Pi$ transitions. The boxes represent multiple levels.

at higher pulse energies the Gaussian peak may be well saturated but the wings of the profile are far from saturated, and the fluorescence signal from the top-hat profile has levelled off completely while the Gaussian solution continues to rise. This demonstrates the previously stated point that lack of saturation in the wings of the temporal profile can introduce significant error if one assumes the transition is fully saturated. The accuracy of this numerical solution was verified by comparing the top-hat numerical solution with the top-hat analytic solution.

2.6.2 Five- and Six-Level Models

The two-level model under-estimates the saturation irradiances for real molecules which undergo rotational relaxation. To model NO, the *five-level model* used by Lee (1991) was employed. Figure 2.4 shows the five-level model. Levels 3 and 4 are the bath levels associated with the laser-coupled levels 1 and 2. The fifth level is the key to the model. It acts as a sink for population lost from laser-coupled vibrational states, and whether this represents an accurate model for NO is now discussed.

A schematic of the NO $A^2\Sigma^+ \leftarrow X^2\Pi$ system is shown in Fig. 2.5. Excitation in LIF experiments usually occurs through the highly populated (0,0) vibrational band. When this occurs, strong non-resonant fluorescence to higher-vibrational bands of the X-state is observed and often utilised in imaging applications to avoid unwanted laser scatter at the excitation wavelength and also the unwanted reabsorption of

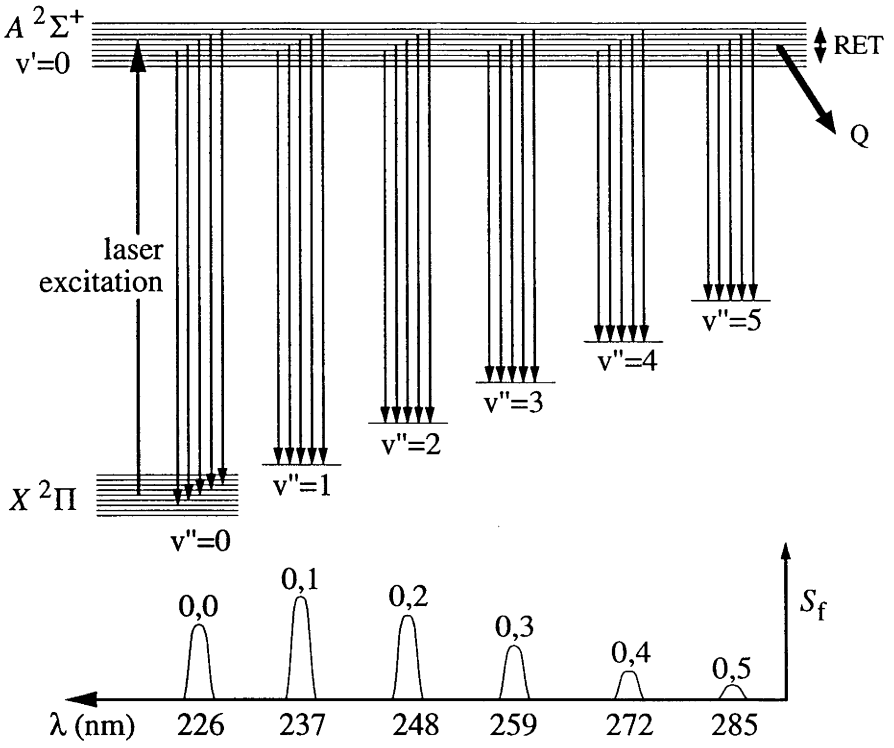

Figure 2.5: The NO $A^2\Sigma^+ \leftarrow X^2\Pi$ electronic transition. The fluorescence spectral distribution is shown at the bottom of the figure. The branching ratios were taken from Piper and Cowles (1986).

fluorescence by the highly populated $v'' = 0$ level (known as radiative trapping). Paul et al. (1994) observes that quenching of the NO $A^2\Sigma^+$ state has a strong tendency to produce vibrationally excited NO $X^2\Pi$. Also, due to the relatively slow vibrational transfer rates (Stephenson 1974) there is expected to be little or no 'recycling' of the population on the time scale of the laser pulse. Hence the excited vibrational levels of the NO $X^2\Pi$ state act as a sink for the population.

The rate equations for the five-level model were numerically integrated using a *stiff* ordinary differential equation solver routine taken from Press et al. (1992, pp. 731–735). This routine uses an automatic step-size adjustment algorithm to integrate over the laser pulse duration and the fluorescence after the pulse (500 ns is adequate for most quenching environments, although for very low pressures this may need to be increased). The quenching rate constants were determined using the equations of Sect. 2.4 and temperature-dependent cross-sections calculated using the equations and data from Paul et al. (1994). RET rate constants were calculated in the same manner, however, due to limited cross-section data, the values employed by Lee (1991) were used. The A-state RET cross-sections for collisions with NO, N_2, O_2 and Ar are 67, 66, 66, 30 Å^2 respectively (Ebata et al. 1984). The RET cross-sections in the X-state were set equal to the A-state cross-section due to lack of

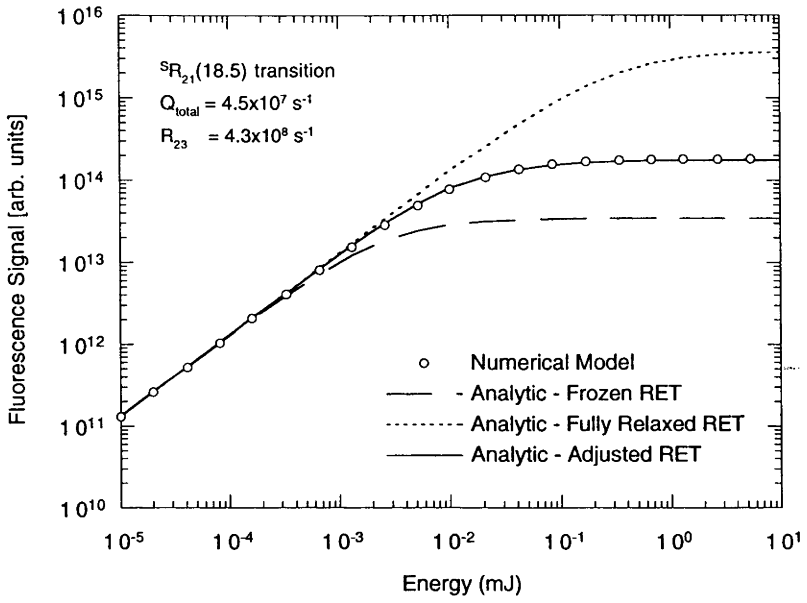

Figure 2.6: A comparison of saturation irradiances given by the five-level numerical model and from the analytic solution assuming varying degrees of RET.

data and on the basis that the rotational energy spacing for the two vibrational states are similar. The rate equations were simplified by assuming the Einstein A coefficients and quenching rate constants were independent of rotational level ($A_{25} = A_{35} = A; Q_{25} = Q_{35} = Q$). See Sect. 2.7 for supporting evidence for this assumption. For the model to be realistic, the rate constant R_{23} must be much larger than R_{32} (and similarly for R_{14} and R_{41}). Therefore, it is assumed that $R_{23} = MR_{32}$ where $M \approx N_T/N_1^0$ (Berg and Shackleford 1979), and the state-to-state RET rate constant calculated above using the cross-sectional data of Ebata et al. (1984) is equal to R_{23}. M represents the number of rotational levels that contribute to rotational redistribution and is approximately equal to the inverse of the initial Boltzmann fraction of level 1.

An analytic expression for the saturation irradiance which includes the effects of RET is given by (Eckbreth 1996, p. 406)

$$I_{\text{sat}}^{\nu} = \frac{A+Q}{B_{12}+B_{21}}\left(1+\frac{R_{23}}{R_{32}}\right) \approx \frac{A+Q}{B_{12}+B_{21}}M \ , \tag{2.59}$$

where the M indicates the increase in laser irradiance required to saturate the transition due to the effects of RET. Figure 2.6 shows a comparison between the cases of no rotational relaxation ($M = 1$) and the complete rotational relaxation ($M = N_T/N_1^0$). The numerical solution is obtained using the five-level model and

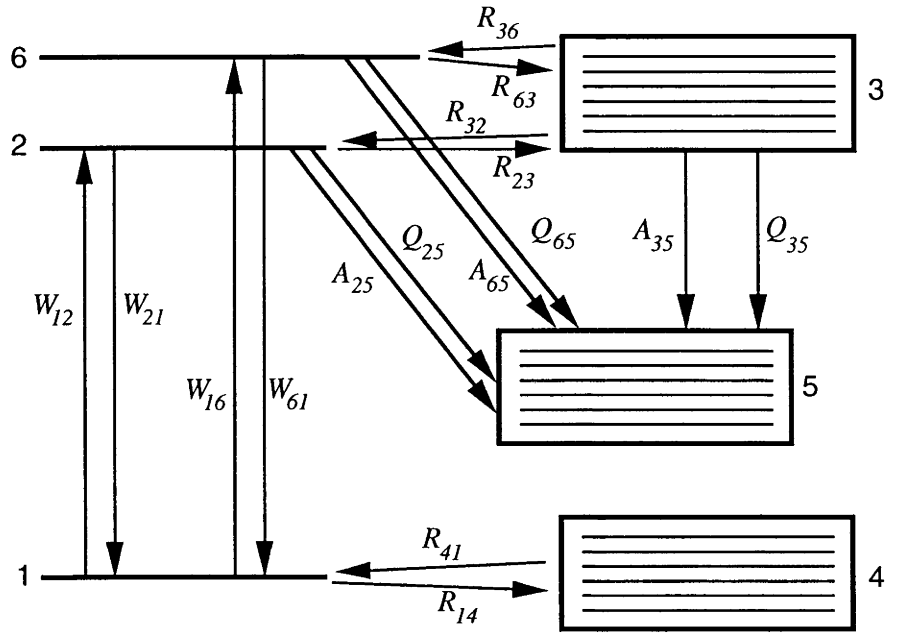

Figure 2.7: The six-level model used for modelling overlapping transitions.

falls about midway between the two analytic solutions.

The *six-level model* is shown in Fig. 2.7. Levels 2 and 6 now represent the spin-split levels of the A-state. The modelling proceeds in the same manner as with the five-level model described above. Figure 2.8 shows a comparison between the various numerical models. For the comparison, the Q_1+$^QP_{21}(27.5)$ transition-pair of the (0,0) vibrational band was used, and the transition strengths were added for the two- and five-level models, thereby approximating a single strong line. In general, the only major difference occurs in the saturating regime where the saturation irradiance for the six-level model is higher. In the linear regime all the solutions converge to the simple two-level model solution.

In the analytic solutions of Killinger et al. (1976) and (Greenstein and Bates 1975), the saturation irradiance and broadening is included explicitly in the equations for the absorption coefficient, but as mentioned previously, saturation broadening comes about due to stimulated emission (W_{21}) effectively reducing the population transfer to the excited state more at line centre than in the wings. Thus, although it does not appear explicitly in the rate-equations analyses above, saturation broadening would be observed if the numerical simulation of a spectrally resolved LIF or absorption experiment were performed.

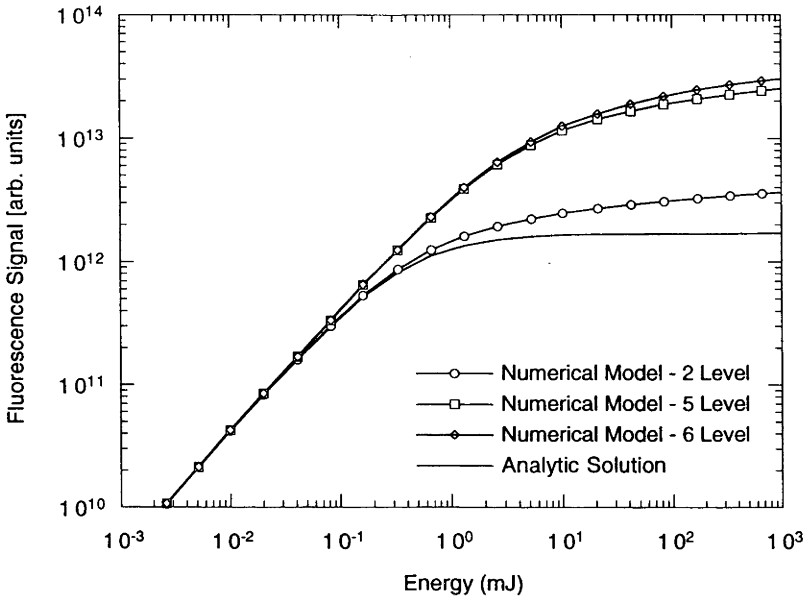

Figure 2.8: A comparison between the two-, five- and six-level numerical models for NO. A Gaussian temporal pulse shape is used for all cases except the analytic solution which was a top-hat function.

2.6.3 Validity of Rate Equation Analysis

The rate-equation approach is justified when coherent transients can be ignored (Altkorn and Zare 1984). This holds when the laser pulse rises slowly compared to the average time between collisions (Daily 1977*b*). Multimode lasers also tend to mask coherence effects because they have a reduced coherence time compared with single mode lasers. Signal averaging over many laser pulses also tends to mask coherence effects.

The bath-level approach to RET generally overpredicts RET. An alternative approach would be to model every rotational level separately (Lucht and Laurendeau 1979). However, since RET cross-section data is very limited for NO, this approach may not significantly increase the accuracy of the model. The bath-level approach should remain relatively accurate while RET only transfers a total population equal to several times the initial absorbing state population (Lee 1991).

2.7 Thermometry

There are many different approaches to LIF thermometry (Eckbreth 1996, Seitzman and Hanson 1993, Laurendeau 1988), but here we discuss only the method most relevant to the current experiments. This method is based on the *two-line* planar-thermometry technique used by Palmer et al. (1996) and McMillin et al. (1993). The theory for performing point-wise thermometry and planar thermometry are equivalent but the implementation differs considerably. For PLIF, consider a sheet of laser light passing through an absorbing medium and a two-dimensional array camera mounted perpendicular to the sheet. If each picture element (pixel) of the array is considered as a separate detector, then it collects fluorescence photons from a definite volume within the absorbing medium. This volume we will term the collection-volume, and its size depends on the pixel size and the magnification of the imaging optics of the camera. By considering pixels as separate detectors we can reduce the two-dimensional technique to the point-wise technique.

To see how temperature can be extracted from the fluorescence signal measurement, we begin by re-expressing the linear fluorescence equation (2.16). We are considering the electronic transition between the electronic-vibrational-rotational level $mv''J''$ and the excited-state level $nv'J'$. We will use the shorthand notation to write the Einstein absorption coefficient for this particular rotational-vibrational transition as $B_{J'J''}$. The absorption rate constant W_{12} can be rewritten using Eq. 2.46 as

$$W_{12} = B_{J'J''} IG = \frac{B_{J'J''} EG}{a t_{\text{las}}} , \tag{2.60}$$

where we have used the relation for the intensity $I = E/(at_{\text{las}})$. The initial population of the level $mv''J''$ is given by $N_1^0 = N_{\text{T}} f_{\text{B}} = (p\chi/kT) f_{\text{B}}$, where p [Pa] is pressure, χ is NO mole fraction, T [K] is the kinetic temperature, f_{B} is the Boltzmann fraction,† given by

$$f_{\text{B}} = \frac{2J''+1}{Z_{\text{total}}} \exp\left(\frac{-F_{J''}}{kT_{\text{rot}}}\right) \exp\left(\frac{-G_{v''}}{kT_{\text{vib}}}\right) . \tag{2.61}$$

Here, we have indicated the rotational and vibrational contributions to f_{B} and made the distinction between the rotational temperature T_{rot} and vibrational temperature T_{vib}. $F_{J''}$ is the rotationally dependent part of the energy of the absorbing state and $G_{v''}$ is the vibrational energy. Z_{total} is the total partition function and k is the

†This definition assumes there is local thermodynamic equilibrium between the rotational levels. Since it takes only a few collisions for rotation to equilibrate with translation, this rotational temperature may also be considered a measure of the translational temperature (Vincenti and Kruger 1975). Non-equilibrium amongst the vibrational levels is common in nozzle expansion flows.

Boltzmann constant. We redefine the fluorescence yield Φ as

$$\Phi = \frac{A_{\text{eff}}}{A_{\text{total}} + Q} , \tag{2.62}$$

where A_{eff} [s^{-1}] is the effective spontaneous emission rate for the collected fluorescence, A_{total} [s^{-1}] is the sum of spontaneous emission rates for all possible radiative transitions from the excited level, and Q [s^{-1}] is the collisional quenching rate. A_{eff} represents the way that A_{total} is modified by spectrally selective elements in the detection chain (*e.g.*, filters, camera quantum efficiency). Therefore the effective emission rate is given by (Allen et al. 1993)

$$A_{\text{eff}} = \sum_{v''} T_{\lambda v''} A_{v'v''} , \tag{2.63}$$

where $T_{\lambda v''}$ is the spectral transmission function for the detection system at the wavelength λ and the summation is over all vibrational bands of the lower electronic state. Hence, substituting these new definitions into Eq. 2.16, the number of fluorescence photons reaching the detector is given by

$$N_{\text{p}} = N_{\text{T}} f_{\text{B}} B_{J'J''} E G \Phi \frac{\Omega}{4\pi} \eta \ell . \tag{2.64}$$

Note that the dependence on irradiance cross-sectional area a and pulse length t_{las} have cancelled out. This demonstrates that, in the linear regime, the signal is dependent only on the number of incident laser photons and not the pulse duration or photon density. For Eq. 2.64 to represent the number of photons collected by a single pixel, ℓ must represent the length of the laser beam which is imaged onto a single pixel and Ω must be the solid angle subtended by the collection-volume to the imaging optics.

2.7.1 Two-line Measurements

Let us consider the temperature and rotational level dependence of each quantity in Eq. 2.64. Hence, for transition i, we have

$$N_{\text{p}} \propto E N_{\text{T}}(T) f_{\text{B}}(T, J) B(J) G(T, J) \Phi(T, J) , \tag{2.65}$$

where, for simplicity $B = B_{J'J''}$, $T = T_{\text{rot}}$ and $J = J''$. Now, if we make fluorescence measurements by exciting two different rotational levels (denoted by numbers 1 and 2), and take the ratio of the signals, we get

$$\text{Signal Ratio} = \frac{N_{\text{p1}}}{N_{\text{p2}}} = C \frac{E_1}{E_2} \frac{B_1}{B_2} \frac{f_{\text{B1}}}{f_{\text{B2}}} , \tag{2.66}$$

where C is a constant and we have assumed the quantities $G(T, J)$ and $\Phi(T, J)$ are independent of the excitation level J and hence any temperature dependence cancels out in the ratio. * Also, we have assumed that the number density of NO molecules $N_T(T)$ remains constant between the two measurements and also cancels. We will justify these assumptions below. The laser energy E is not dependent on J but usually fluctuates from pulse-to-pulse and so is retained for completeness. Equation 2.66 shows that the only temperature dependence is through the Boltzmann fraction, and this is the basis of most LIF thermometry techniques. Substituting for f_B from Eq. 2.61 and assuming that each transition is within the same vibrational band (*i.e.*, $G_{v''}$ is constant), we obtain

$$\frac{N_{p1}}{N_{p2}} = C\frac{E_1 B_1(2J_1+1)}{E_2 B_2(2J_2+1)} \exp\left(\frac{-(F_{J1}-F_{J2})}{kT_{rot}}\right) , \tag{2.67}$$

and, solving for T_{rot},

$$T_{rot} = \frac{(F_{J2}-F_{J1})/k}{\ln\left(C\frac{E_2 B_2(2J_2+1)}{E_1 B_1(2J_1+1)}\frac{N_{p1}}{N_{p2}}\right)} . \tag{2.68}$$

In a typical temperature measurement, one measures the fluorescence signal N_p and laser pulse energy E for each rotational level. Then, using calculated values for $F_{J''}$ and $B_{J'J''}$, the temperature can be obtained. This assumes that the value of C is known or has been determined empirically.

2.7.2 The Constant C

The constant C in Eq. 2.68 can be written such that all the quantities related to the detection system are contained within a separate constant C'. Hence we have

$$C = C'\frac{N_{T1} G_1 \Phi_1}{N_{T2} G_2 \Phi_2} . \tag{2.69}$$

C' is a constant containing the remaining quantities, that is

$$C' = \frac{\Omega_1 \eta_1 \ell_1}{\Omega_2 \eta_2 \ell_2} \tag{2.70}$$

which can be determined by calibration if different detectors are used for each measurement, or is equal to unity if the same detector and collection geometry are used.

*The constancy of G, and therefore C, depends on the repeatability of the laser spectral profiles. It will be seen in later chapters that fluctuations in the laser spectral profile contribute considerably to the uncertainties in the temperature measurements for the present work.

For PLIF thermometry in unsteady or turbulent flows, it is necessary to use two lasers and two cameras. The two transitions are excited in rapid sequence, thus freezing the flow motion, and ensuring that the flow conditions remain the same for both measurements (*i.e.*, N_{T1}=N_{T2}). However, for steady or repeatable flows it suffices to use one laser and camera and assume a degree of flow reproducibility. This is more attractive from an monetary point of view, as not many laboratories can devote two laser/camera systems to a single experiment. It also removes the need for calibration since the same detection system is used for both and hence $\Omega_1\eta_1 = \Omega_2\eta_2$. For pulsed facilities like the shock tunnel, this means taking images on successive shots of the tunnel. The one-laser-and-camera method has been employed here and therefore $C' = 1$, and if we assume perfect flow reproducibility, the flow conditions are a constant and hence N_{T1}=N_{T2}. The validity of this last assumption will be discussed in Sect. 4.6.

In Eq. 2.66, we assumed that the *ratios* Φ_1/Φ_2 and G_1/G_2 were independent of temperature. This is a good assumption if Φ and G are independent of J and reabsorption of fluorescence is negligible (McMillin et al. 1994). For the $A^2\Sigma^+(v' = 0)$ band of NO, the spontaneous emission rates and collisional quenching rates are independent of rotational quantum number[†] (McDermid and Laudenslager 1982). Hence we have $A_{\text{eff1}} = A_{\text{eff2}}$ and $Q_1 = Q_2$ and therefore Φ is also independent of J. The absorption line shape, $Y(\nu)$, is affected by collisional broadening and shifting (Chang et al. 1992, Di Rosa 1994), Doppler broadening, and Doppler shifts due to the flow velocity. The Doppler broadening varies with frequency but for transitions in the same vibrational band, $\nu_{a1} \approx \nu_{a2}$, and so $Y(\nu)$ can be considered independent of J. Providing that the laser-line profile overlaps the absorption-line profile in the same way for both transitions, and the laser spectral profiles are also the same (*i.e.*, no mode fluctuations) $G_1 = G_2$. The overlap integral will vary throughout the flowfield due to variations in pressure and temperature, but will remain independent of J. From the above considerations and the fact that $C' = 1$, it follows that $C = 1$. Provided that the assumptions about the NO spectroscopy are valid, then the main concern here is that the laser is tuned to the transition in the same manner for both lines.

For instantaneous thermometry imaging using two lasers and two cameras, $\eta_1 \neq \eta_2$. In that case, it is possible to calibrate the system if the temperature is known at one point in the imaged region. The value for C' can be determined and is a constant for the imaging system. Also, for a given set of transitions, C can be determined. In supersonic flows, this calibration point can be obtained from the stagnation point on a body or alternatively from the freestream temperature. Single-pulse/single-point

[†]Rotational-level-dependent quenching has been observed in OH$A^2\Sigma^+$ for low-J and temperatures in the range 300-1200 K. It should also manifest in NO$A^2\Sigma^+$ at $J < 5$ and at temperatures less than 300 K, according to Paul et al. (1994), based on computational models. J-dependent quenching would cause a significant systematic error in low-temperature NO thermometry if low-J lines were used. This combination of low-J lines for measuring low temperatures is avoided in the present experiments.

broadband CARS thermometry may also be used (Hahn et al. 1997).

2.7.3 Temperature Sensitivity

If we take the derivative of Eq. 2.68 with respect to the signal ratio R and rearrange, we find the temperature sensitivity is given by (Seitzman and Hanson 1993)

$$\left|\frac{\delta T}{T}\right| = \frac{kT}{|\Delta E|}\left|\frac{\delta R}{R}\right| , \tag{2.71}$$

where $R = N_{\mathrm{p1}}/N_{\mathrm{p2}}$ is the ratio of two fluorescence signals and ΔE is the energy separation between the two absorbing states. δT and δR are the uncertainties in temperature T and signal ratio R respectively. It is readily seen that a large ΔE gives the best sensitivity, however this approach is tempered by the need to keep the signal levels within the dynamic range of the camera. A large ΔE translates into a large difference in J'' for the two transitions, which invariably means a significant signal level variation at a given temperature. In practice, we generally find $\Delta E \approx kT$ is a good compromise. This will be an important factor to consider when choosing transitions.

An alternative approach that would allow a very large ΔE would be to alter the detector gain, some other parameter in the detection chain, or the laser irradiance, in order to maintain similar signal levels for both transitions and also to utilise as much of the dynamic range as possible. This would require calibrating the detection system response (*e.g.,* camera gain, filters) or using a known temperature in the flow for calibration. When the laser irradiance is varied, one must ensure both measurements are in the linear fluorescence regime or else it becomes necessary to know the degree of saturation for both transitions.

2.7.4 Multi-line Measurements

When the conditions and the hence fluorescence signal in the imaged region vary appreciably, the use of three or more transitions can be used to ensure that at each point in the image there are at least two transitions with appreciable signal to contribute to the temperature determination (Palmer et al. 1996). Using multiple transitions may also indicate systematic errors if the measured signals deviate from a straight line on a Boltzmann plot. For example, one transition may have an unexpected contribution from another NO transition or chemical species (*e.g.,* O_2).

Rotational temperatures are measured by making two or more fluorescence measurements with different J'' and the same v''. In this case, the vibrational part of

Eq. 2.61 is constant and cancels with all the other J-independent quantities. Then a Boltzmann plot of

$$\ln\left(\frac{N_\mathrm{p}}{EB_{J'J''}(2J''+1)}\right)$$

versus $F_{J''}$ gives a straight line with slope $-1/(kT_\mathrm{rot})$.

Vibrational temperature can be measured in an analogous way. Measuring fluorescence images for two or more transitions with different v'' and plotting

$$\ln\left(\frac{N_\mathrm{p}}{EB_{J'J''}(2J''+1)\exp(-F_{J''}/kT_\mathrm{rot})}\right)$$

versus $G_{v''}$ gives a straight line with slope $-1/(kT_\mathrm{vib})$. By keeping $F_{J''}$ as constant as possible, its influence is minor, and the vibrational temperature is therefore determined independent of the rotational temperature.

2.7.5 Thermometry Strategy for Current Work

The format for the experiments was as follows. The light from a single narrowband laser system was formed into a sheet and used to probe the shock tunnel flow. An intensified CCD camera collected the fluorescence signal at right angles to the sheet. Only one image was obtained per tunnel run. To make temperature measurements, different absorption transitions were probed on separate tunnel runs. Generally five images were produced for each transition and averaged. The temperature thus determined is an average of the flow conditions for that series of shock tunnel runs.

The excitation scheme generally employed for NO thermometry involves excitation of NO through the $A^2\Sigma^+ \leftarrow X^2\Pi$ ($v'' = 0$) band at 225 nm. Fluorescence is then collected from several vibrational bands at higher wavelength, away from the excitation wavelength (see Fig. 2.5). Detection at the excitation wavelength is avoided to prevent contributions to the signal from laser scatter. Furthermore, fluorescence transitions ending in the less-populated vibrational bands ($v'' \geq 1$) are preferred to reduce the influence of *fluorescence trapping*, which occurs when fluorescence photons are reabsorbed by molecules between the interaction-volume and the detector. When *broadband fluorescence detection* is employed, fluorescence is collected from all the rotational levels populated by collisions and not just the laser-coupled level (Seitzman and Hanson 1993). This has two advantages. First, collecting all the fluorescence gives higher signal strengths. Second, most modern lasers have a high degree of polarisation which can make the fluorescence from the laser coupled level highly anisotropic (Doherty and Crosley 1982). The levels populated by RET have reduced anisotropy due to depolarising collisions and thus collecting the broadband fluorescence significantly reduces these effects. Broadband fluorescence detection was employed in the experiments in the current study.

This is the format used in the preliminary PLIF experiments to be described in the next chapter. After the analysis of these preliminary results, slight improvements on the technique were made and these variations will be discussed in Chap. 5.

2.8 Summary

This chapter has been concerned with developing the theoretical background necessary for the LIF experiments described later in this monograph. In particular, we have presented analytic solutions to a simple fluorescence model and compared them with results from full numerical simulations of the molecular excitation dynamics. Accurate calculation of the fluorescence signals for a wide range of environments is desirable, especially when choosing which transitions are optimal for a particular temperature measurement. A basic approach for isolating the temperature dependence of the fluorescence signal was also presented.

In this chapter, we have neglected certain aspects that will later be seen to be very important to PLIF thermometry. These effects include attenuation of the laser beam as it passes through an optically thick medium, the non-ideal nature of the irradiance spectral profile (*i.e.*, mode structure), background flow luminosity and partial saturation of transitions. These concepts will be elaborated on in the next few chapters when we come to analyse experimental results and plan improvements to the technique.

Chapter 3

Laser-Induced Fluorescence Imaging using a Raman-Shifted Tunable Excimer Laser

3.1 Introduction

This chapter serves two purposes. First, it describes some PLIF thermometry experiments performed with a Raman-shifted tunable excimer laser which are unique in their own right. From these experiments, it is possible to form some conclusions about the effectiveness of using this type of laser source for quantitative fluorescence measurements. Second, and perhaps more importantly, it serves to identify some of the important parameters and difficulties that are associated with applying PLIF thermometry to shock tunnels. With this new information in mind, it is then possible to re-evaluate and optimise various experimental parameters to more accurately perform PLIF thermometry in shock tunnels. This re-evaluation procedure and the second iteration of the thermometry experiments is described in Chapters 5 and 6.

Tunable excimer lasers have been used for combustion diagnostics and flow visualisation (Andresen et al. 1990, Ketterle et al. 1992). However, due to their limited tuning ranges (typically 1 nm) they have not been as widely employed as frequency-doubled dye laser systems. By Raman-shifting the output of a tunable-excimer laser it is possible to substantially increase the flexibility and tunability of the laser system (Dreier et al. 1992). In particular, by Raman-shifting the 248 nm output of a KrF tunable-excimer laser in H_2, we can produce tunable-narrowband radiation between 224.8 and 225.7 nm. This coincides with the $A^2\Sigma^+ \leftarrow X^2\Pi(0,0)$ absorption band of nitric oxide.

We begin by investigating the flow over two rather simple geometric shapes: a wedge and a cylinder. The flowfields are designed to be two-dimensional because:

- two-dimensional flowfield calculations are much simpler and therefore can be used as a comparison to the experimental measurements. In general three-dimensional aerodynamic problems take an order-of-magnitude more work to obtain a solution (Anderson 1990, p. 390).
- the size of the post-shock region is smaller for axi-symmetric models due to the "three-dimensional relieving effect"(Anderson 1990, p. 112). The larger the flow region, the easier it is to make a measurement due to the limited spatial resolution of the detection system.

The total enthalpy is kept reasonably low due to the problems with flow luminosity. The test gas was air which was an attempt to simulate a real flow composition, with possible difficulties expected from the high NO and O_2 concentrations.

3.2 Experiment

3.2.1 Flow Conditions

The experiments were performed on the T2 free-piston shock tunnel at the Australian National University. A description of the shock tunnel and its operation has been given by Stalker (1967)[†]. The same flow conditions were used for both cylinder and wedge experiments and the test gas was always air. The T2 nozzle is a 7.5° half-angle conical geometry with a 6.4-mm diameter throat and a nozzle-exit diameter of 73 mm. Two pressure transducers were mounted along the shock tube to measure the nozzle-reservoir pressure (PCB P/N 113A23, S/N 5960, 0.521 mV/psi) and, by monitoring the transit time of the primary shock between the transducers (a distance of 1270 mm), the shock speed. The primary-shock speed was measured to be 1.9 ± 0.4 km s^{-1} which corresponds to a flow enthalpy of 4.1 MJ kg^{-1}. The nozzle-reservoir pressure was measured to be 28.4 ± 0.5 MPa and the calculated reservoir temperature was 3310 ± 80 K. The freestream temperature and pressure were calculated to be 300 ± 20 K and 4.2 ± 0.7 kPa respectively.

The reflected-shock conditions were calculated using the equilibrium shock tube code ESTC by McIntosh (1968). The nozzle-exit conditions were calculated using the quasi-one-dimensional nozzle flow code STUBE (Vardavas 1984). The gas in

[†]A summary of the shock tunnel design and operation, the flow conditions and methods used to calculate those conditions (ESTC and STUBE computer codes) is given in Chapter 4.

the nozzle reservoir is in thermochemical equilibrium due to the high pressure and temperature, however as it rapidly expands through the nozzle, chemical and vibrational nonequilibrium effects begin to dominate. The nozzle-exit temperatures calculated assuming vibrationally frozen and equilibrium flow were 240 K and 370 K, respectively, and demonstrate the influence that vibrational excitation has on the freestream temperature. The species concentrations were observed from the calculations to be frozen from about 10 mm downstream of the throat and the major species mole fractions at the nozzle exit were: N_2 0.751; O_2 0.178; NO 0.058; O 0.001. All of these calculations were performed assuming a reduced nozzle half-angle of 7.0° to account for the nozzle-wall boundary layer (verified by pitot survey). This reduced nozzle half-angle leads to a temperature increase at the nozzle exit of about 6%, when compared with calculations using the physical nozzle half-angle of 7.5°.

The shock tunnel filling conditions for this low-enthalpy condition are: reservoir 4.34 MPa (630 psi) of air; compression tube 118.6 kPa (17.2 psia) of Ar; shock tube 99 kPa of air (BOC instrument grade). The diaphragm was unscored mild steel of thickness 0.74 mm (0.029 inches) with a burst pressure of 46.9 MPa (6800 psi). The fill pressures were chosen to achieve a fairly tailored nozzle reservoir trace. The test time delay for firing the laser was chosen to be 450 μs after shock reflection, which is sufficient time to establish the flow. However, little is known about driver gas contamination in this facility and, therefore, there is a possibility that there may be some fraction of driver gas mixed with the test gas at this time.

The cylinder has a diameter of 25.4 mm and a length of 150 mm which means it extends beyond the edges of the core flow. The wedge has a half angle of 35° but is only 25.4 mm in length (perpendicular to the flow), and therefore is contained entirely within the core flow. Disturbances propagating from the corners of the leading edge of the wedge cause disturbances downstream. However, for the conditions used here, these disturbances reach the plane of the laser sheet far enough downstream to not be a problem. Both models were placed at a distance 39 mm from the nozzle exit, which, after taking a shock-tube recoil of 8 mm into account, puts the leading edge of the model 47 mm from the nozzle exit at the time the laser fires. The throat to nozzle-exit distance is 255 mm along the centreline.

3.2.2 Apparatus

In this section, an overview of the experimental arrangement is given, followed by a more detailed discussion of the individual components. A schematic of the experimental set up is shown in Fig. 3.1. A cell containing high-pressure hydrogen (1000 kPa) was used to Raman-shift the 248-nm output of a tunable-excimer laser. The first anti-Stokes order was separated from the other orders with a Pellin-Broca prism and formed into a sheet using a 40-mm focal-length cylindrical lens and a 1000-mm focal-length spherical lens. The sheet was 80-mm wide and loosely focussed

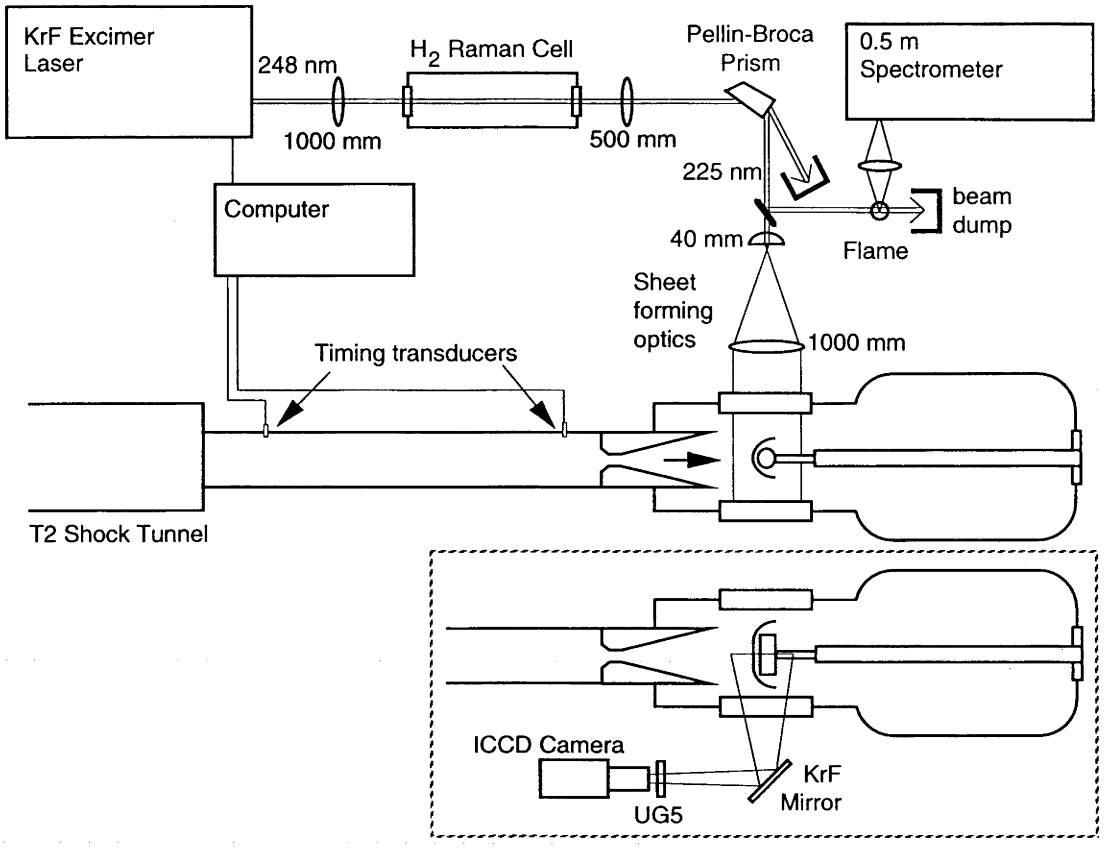

Figure 3.1: Plan view of the experimental arrangement used for performing PLIF in the T2 shock tunnel with a Raman-shifted tunable excimer laser. The inset shows a side view of the experiment with the intensified camera mounted below the test section and the filtering used in the experiments.

to approximately 1-mm thickness. The radiation was tunable between 224.9 and 225.4 nm which coincides with the $A^2\Sigma^+ \leftarrow X^2\Pi(0,0)$ band of NO. A small portion of the beam was split off and used for wavelength calibration by passing it through a fuel-rich H_2/O_2 flame. The laser-induced fluorescence (LIF) from the flame was imaged onto a 0.5-m spectrometer (which acts as a 9-nm bandpass filter), allowing detection of LIF from only the NO (0,1) vibrational band near 236 nm. This prevented the very strong OH emission bands near 308 nm from dominating the fluorescence signal. The energy of the Raman-shifted beam was typically 4 mJ per pulse with a linewidth of approximately 0.25 cm^{-1} FWHM.

An intensified CCD camera (250-ns gate) was used to capture the fluorescence image at right angles to the laser sheet. The fluorescence was turned through 90° by reflecting it off a dielectric mirror. A 3-mm-thick UG5 Schott glass filter was used to block off elastic scatter at the laser wavelength. Therefore, only the non-resonant fluorescence bands ($v'' \geq 1$) pass through to the camera.

Raman-Shifted Tunable Excimer Laser

The Lambda Physik EMG 150 ETS is a dual chamber (oscillator/amplifier) excimer laser capable of producing 750 mJ of narrowband tunable radiation at 248 nm, and at a 10-Hz repetition rate (specifications from the operator's manual). Operation at this wavelength corresponds to a gas-fill mixture of KrF. The oscillator consists of a stable resonator producing a near diffraction-limited beam. A series of prisms act as a dispersive element within the oscillator cavity and enables narrowband and tunable operation. The narrowband oscillator output is fed into the amplifier chamber and expanded by the unstable resonator optics of the amplifier. The unstable resonator ensures a low divergence output beam. When the oscillator is blocked or disabled the amplifier runs broadband which means it lases across the whole gain profile. When the oscillator is enabled the amplifier is forced to lase in just the narrow bandwidth determined by oscillator. The effectiveness of this process is termed the locking efficiency.

When the laser is operated at 248 nm, the linewidth (specified by the manufacturer) is 0.003 nm (0.5 cm^{-1}) and the tuning range is 0.5 nm (75 cm^{-1}). The narrowband tunable output is achieved by passing the output of the oscillator through an aperture, then expanding it with a set of four expansion prisms and then dispersed with three 60° prisms. The expanded and dispersed beam is reflected from a flat mirror and then traverses the same path back to the oscillator where the aperture only selects a small portion (spectral region) to reenter the gain medium. Hence through this process the oscillator is made narrowband, and tuning is achieved by tilting the mirror.

Several modifications were made to the excimer laser for the experiments.

- The tuning of the oscillator was automated by coupling a stepper motor to the micrometer adjuster controlling the mirror position. Control of the stepper motor was then handled by computer to allow synchronised scanning and firing of the laser and data collection. The accuracy of the tuning was estimated to be approximately 0.1 cm^{-1}.
- The laser linewidth was narrowed further by replacing the end mirror with a diffraction grating having 1200 lines/mm and blazed for the visible (*i.e.*, optimised for first order at 500 nm). Used in second order, it is optimised for the UV. The use of the grating with the prisms halved the linewidth so that the linewidth was estimated to be approximately 0.0015 nm (0.25 cm^{-1}).
- The tuning block holding the prisms was temperature stabilised by raising its temperature to just above room temperature. This was accomplished using heating resistors attached directly to the tuning block and a control box which used feedback from a temperature probe to maintain the temperature at the set point.

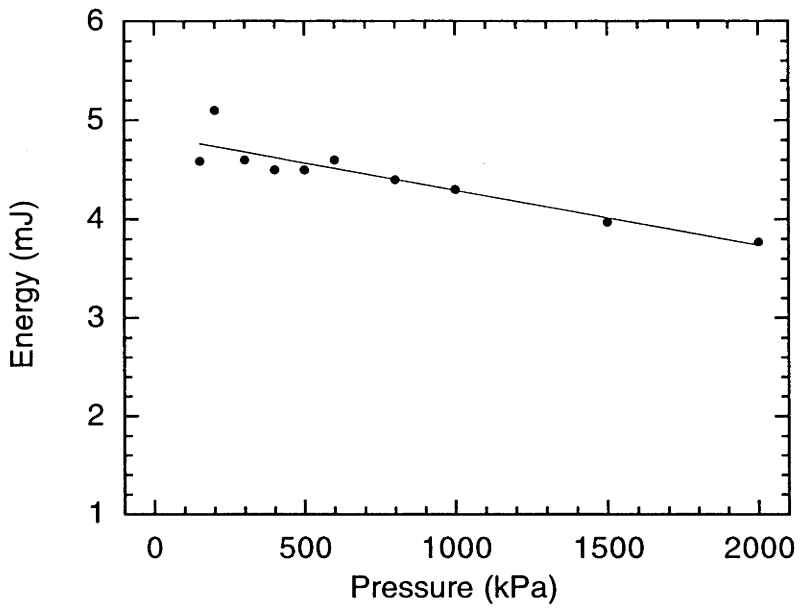

Figure 3.2: The energy of the first anti-Stokes order versus Raman-cell fill pressure of H_2. The experiments were performed at 1000 kPa.

Wavelength conversion was achieved by anti-Stokes Raman scattering (ASRS). The experimental set up was as described by Lewis et al. (1989). The excimer pump beam was focused into a 1-m Raman cell with a 1-m focal-length lens. The emergent forward-scattered anti-Stokes beam was collimated by a 500-mm focal-length lens and had a uniform rectangular geometry representative of the pump beam. The first anti-Stokes order (1AS) was separated from the fundamental and other Stokes and anti-Stokes components using a Pellin-Broca prism. The cell was operated at room temperature with 150-2000 kPa of ultrahigh-purity H_2 (99.999%). Figure 3.2 shows a plot of the energy of the 1AS beam versus fill pressure. The 1AS energy was optimal at about 200 kPa but for pressures below 500 kPa we observed large pulse-to-pulse fluctuations.

The dominant vibrational shift for H_2 is 4155 cm^{-1} and the dominant rotational shift is 588 cm^{-1}. If the input radiation is circularly or elliptically polarised, stimulated Raman oscillation will occur at the rotational frequency (Levenson and Kano 1987, p. 259) . A side-band was observed on either side of the 1AS beam at the dispersed output of the Pellin-Broca prism. The measured wavelength of the fundamental and side-bands indicated that they were indeed due to rotational Raman-shifting. It was further observed however that the side bands were strongest at a fill pressure of 200 kPa but decreased in intensity with increasing pressure until they were unobservable above 1000 kPa. The experiments were performed with a fill pressure of 1000 kPa which provided adequate energy, pulse-to-pulse fluctuations comparable to those inherent in the pump beam, and negligible influence from rotational

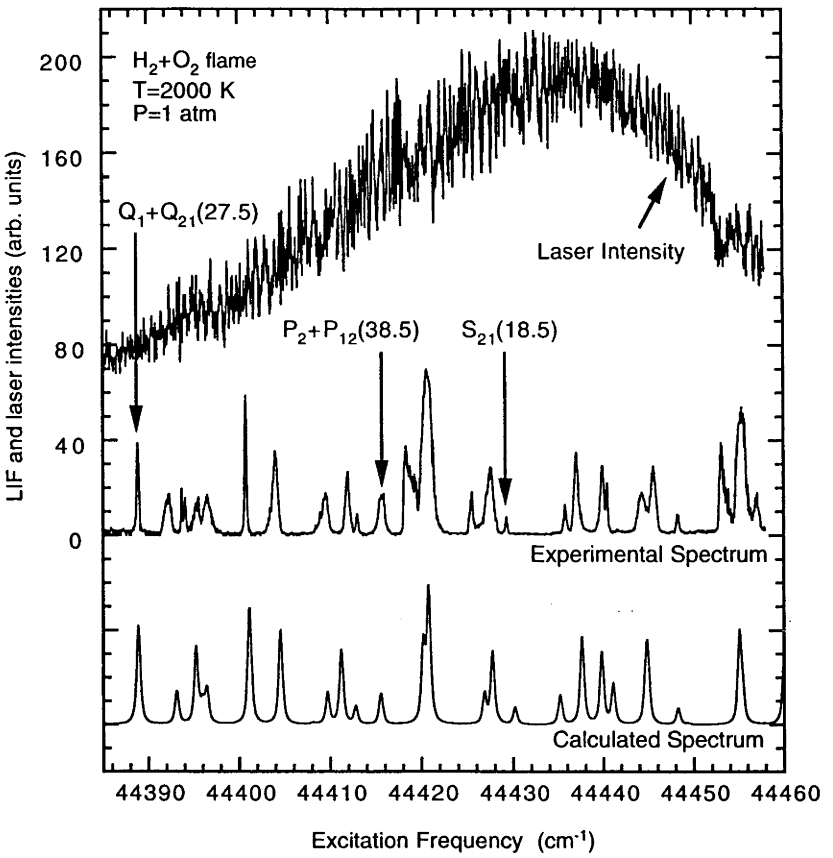

Figure 3.3: Comparison of experimental and calculated LIF excitation scans in an atmospheric flame at 2000 K. Also shown is the variation in laser energy across the tuning range of laser. The transitions indicated by arrows are those used in the current experiments. The excitation spectrum is calculated from the equations in Appendix A using a laser linewidth of 0.25 cm^{-1}.

Raman-shifting.

Problems Encountered with the Laser System

Figure 3.3 shows an example of a LIF excitation scan in an atmospheric pressure flame at 2000 K. The calculated spectrum assumes a Lorentzian laser profile with a FWHM of 0.25 cm^{-1}. Several problems were observed with the tuning mechanism, namely the occasional appearance of extra artifacts in the spectrum such as the one near the transition at 44420 cm^{-1} in Fig. 3.3. It appears that the tuning mechanism occasionally skips or jumps as evidenced by the movement in the positions of transitions between successive scans. For the PLIF experiments, tuning was achieved by

maximising the LIF signal in the flame before each shot, and so the problems due to the tuning mechanism were minimal. However, it was observed that there was some drift in the tuning over a period of 20 minutes, which could not be correlated with drifts in the room temperature (the tuning block was also temperature stabilised). For this reason the LIF signal from the flame was monitored right up until the last minute before firing the shock tunnel.

A more significant problem was the variation in the laser linewidth. The linewidth of the oscillator is determined by the aperture and dispersion in the tuning block, but the linewidth of the output from the amplifier also depends on the locking efficiency of the oscillator to the amplifier. For the EMG 150 ETS, the locking efficiency can be as low as 70% due to the high gain of the amplifier. The energy of the oscillator then has a large influence on the locking efficiency and hence the linewidth. During the course of the experiments, the electrostatic filters which lengthen the lifetime of a particular excimer-laser gas fill became inoperative. As the oscillator energy drops the linewidth varies considerably (approximately 0.25 to 0.8 cm^{-1}). The linewidth was monitored indirectly from the LIF flame spectra and the gas fill replaced when the linewidth was observed to broaden significantly. Increasing the energy of the oscillator by decreasing internal losses (*e.g.*, anti-reflection coated prisms), as well fixing the electrostatic filters, would have reduced this problem.

The reduced locking efficiency of the laser is also responsible for producing a weak, broadband background with the narrowband spectral component. This can cause the excitation of nearby transitions in a PLIF experiment and lead to systematic errors in temperature measurements.

Meijer et al. (1986) in their work on resonantly enhanced multiphoton ionisation (REMPI) used the same model excimer laser and discussed some of these problems. They, too, used a grating to decrease the linewidth of the oscillator; moreover they found that they were able to remove some of the dispersion prisms and therefore decrease cavity losses whilst retaining the manufacturer's specified linewidth. This extra oscillator power enabled a better locking efficiency and a greater tuning range ($\approx$150 cm^{-1}). Suppression of broadband background was achieved by tuning to a fluorescence transition and maximising the LIF signal by slight misalignment of the amplifier cavity. In this way the non-resonant fluorescence background completely disappeared. Unfortunately, at the time that the experiments here were performed the work of Meijer et al. (1986) was unknown because of its relation to REMPI and not PLIF.

Intensified CCD Camera

The detector used for these experiments is an in-house assembled intensified CCD (charge coupled device) camera (McIntyre 1995). The intensifier is a 18-mm diam-

eter dual-microchannel plate by Varo Inc., Ni-Tec Division, Garland, Texas (P/N 510-7500-303, S/N 007186). It has a maximum gain of 1×10^6 and a photo-response at 250 nm of 21 mA/W. The geometry consists of 10 μm diameter channels which are 12 μm centre-to-centre and the quoted resolution is 28 lp/mm. It is powered by a GBS micro power supply (P/N 20060000-002, S/N 0105) which converts 10 VDC to high voltage outputs (−6000 VDC). The gating is controlled by TTL input pulses with a minimum gating time of 100 ns. The image is transferred from the intensifier to the CCD via a tapered fibre-optic bundle (Galileo) having a demagnification of 1.21. Silicone oil is used as an index-matching fluid and lubricant between both surfaces of the fibre bundle. The CCD camera (EEV Photon, P/N P45580/V5.3/PHO, S/N 100415) is an 8-bit asynchronous device which is triggered separately from the intensifier. The interlaced readout consists of 578 × 488 pixels in an imaging area of 8.7 × 6.5 mm. The image is read by a Matrox IP8 frame grabber board installed in standard IBM compatible personal computer which also controls the timing for the rest of the experiment. The image stored from an experiment is a single interlace (every second horizontal line), 512 × 240 pixels. Finally, an ultraviolet telephoto lens was coupled to the front of the intensifier (Nikon, UV Nikor, 105-mm focal length, f/4.5).

The detection system's linearity was verified by performing PLIF on a mixture of 5% NO in N_2 at a total pressure of 270 Pa (2 Torr) in the shock tunnel test section. The total laser power was varied using calibrated UV neutral density filters (Optics for Research, P/N FDU-0.1 etc.). The intensifier settings for the linearity test were a gate of 250 ns width and gain of 7.8 (10 turn potentiometer). The experimental settings were a 250-ns gate and a gain of 7.2. Since the likelihood of intensifier saturation increases with gain, a linear response of the PLIF signal versus laser intensity at a gain of 7.8 ensures linearity at the experiment gain of 7.2. During the test, it was necessary to ensure that the NO transition being excited was not being saturated, as was obviously the case from the positive results.

Spatial Variation of Sheet Energy

The variation in energy across the laser sheet is measured simultaneously by use of a dye cell (100 mm length) and a standard CCD camera (Pulnix TM-760) (Seitzman et al. 1994). The dye used was Rhodamine 590 and the concentration was such that the beam was totally absorbed within the first few millimeters. This energy distribution measurement was used to correct the PLIF image obtained on the same laser pulse. It also takes account of any pulse-to-pulse fluctuations in the total laser energy. The spatial variation of the energy in the laser sheet was observed to remain constant on a pulse-to-pulse basis even over a period of hours. This was possibly due to the high pump energies substantially saturating the ASRS process. However, there was a slight drift throughout the day due to the variation in room temperature. For this reason, energy-profile corrections were recorded for

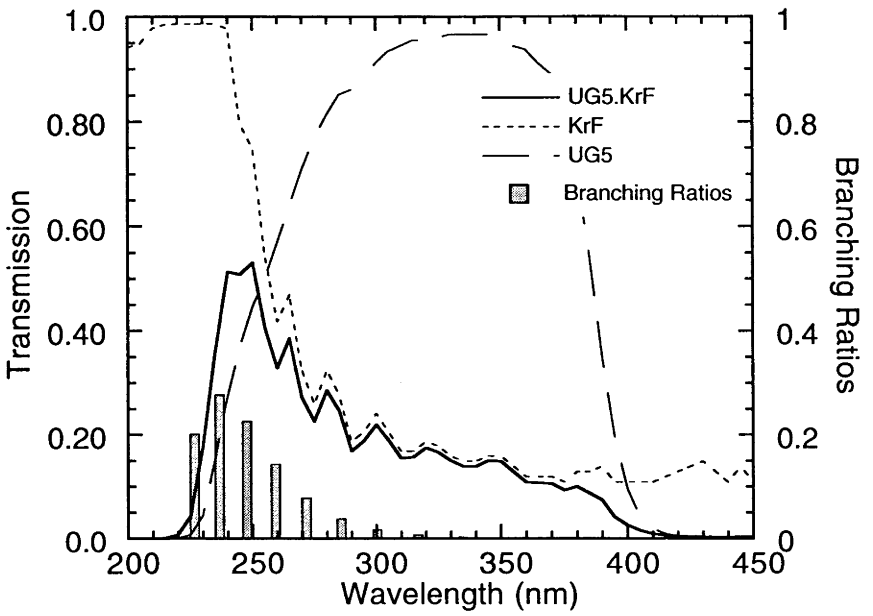

Figure 3.4: Spectral response of KrF mirror and UG5 filter used for filtering the PLIF signal. Also shown are the branching ratios for the NO fluorescence bands.

every tunnel run. The linearity of the sheet profiling monitor was verified by using calibrated neutral density filters to vary the incident laser intensity.

KrF Reflective Filter

Preliminary tunnel runs using just the 3 mm UG5 Schott Glass filter indicated that the flow luminosity was a serious problem. To enhance the signal-to-background ratio it was decided that further spectral filtering was required. By utilising a spare KrF excimer laser mirror as a reflective filter we were able to successfully observe fluorescence signals with the detection system. Figure 3.4 shows the spectral response of the two filters and multiplicative effect of using them in series. The KrF mirror is coated for maximum reflectance at 248 nm for light incident normal to the mirror. However, when turned to a 45° angle of incidence, the response of the coating is shifted to the blue. The maximum reflectance is then between 210 and 240 nm. The UG5 filter was used to block the laser wavelength and prevent scattered laser light reaching the detector. Also shown in Fig. 3.4 is the NO branching ratios for transitions from the $A^2\Sigma^+(v' = 0)$ vibrational level to the $X^2\Pi(v'' = 0, 1, 2\ldots)$ levels.

3.2.3 Line Selection

Within the tuning range of the laser only a limited number of lines are suitable for thermometry. It is preferable to choose lines that are spectrally isolated to prevent PLIF contributions from nearby transitions (the absorption line profile broadens and shifts throughout the flowfield due to the pressure and temperature variations). Transitions with relatively low absorption coefficients are preferable to prevent both excessive beam attenuation across the imaged region and also to prevent saturation of the transition. The beam attenuation problem is also dependent on the NO concentration in the flow which, in the current experiment, cannot be altered without changing the flow conditions.

The transitions used for this work are shown in Table 3.1, which also includes several transitions from previous NO thermometry studies for comparison. For both flowfields considered here, three transitions were chosen with a large variation in rotational quantum number J'', while trying to satisfy the above criteria. The $J'' = 18.5$ transition was the lowest J'' available within the tuning range while the $J'' = 38.5$ transition was one of the highest, giving $\Delta E/k = 3040$ K.

Figure 3.5 shows a plot of the fluorescence ratio versus temperature for several different transition pairs. The dynamic range of the detection system limits the maximum fluorescence ratio that can be measured. For the current 8-bit detection system, we estimate the maximum useful fluorescence ratio to be ≈ 5. Using Fig. 3.5, a fluorescence ratio of 5 for the $J'' = 18.5$ and $J'' = 38.5$ transitions would allow temperatures between approximately 800 and 4000 K to be measured. However, this supposes that one utilises the full dynamic range of the camera which rarely happens in practice due to signal fluctuations. Since the freestream has a temperature of about 300 K, a third line was chosen ($J'' = 27.5$) which, when combined with the $J'' = 18.5$ line, can be used to determine temperatures between 300 K and 1000 K ($\Delta E/\mathrm{k} = 1017$ K). Similar temperature ranges can be determined for the other transition pairs.

If there is a large difference between the signal strengths for a pair of transitions, then digitization and shot noise become a problem for the weaker signal. One method that could be used to reduce these effects would be to use a point in the flow to calibrate the temperature. Then it would be possible to vary the camera gain for weaker signals (or reduce stronger signals) to use the full dynamic range of the camera. This would also eliminate the need for choosing transitions with similar fluorescence signal strengths. However, for the work presented here we did not have an accurate calibration point. Other ways to reduce noise would be to use an improved CCD camera with a larger dynamic range (*e.g.*, 16 bit), or calibrate the gain control of the intensifier.

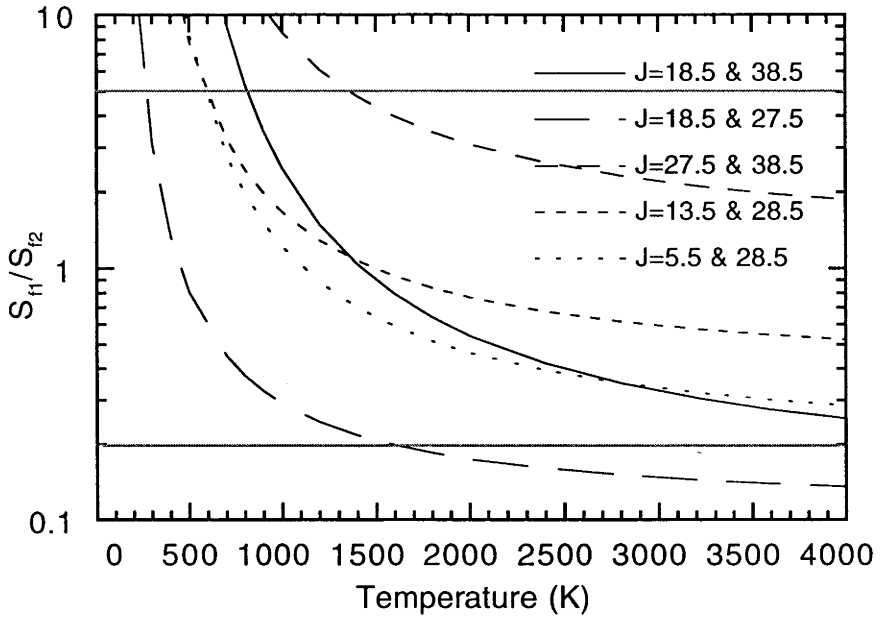

Figure 3.5: Calculated fluorescence ratio versus temperature for various NO transition pairs. The line pair J''=13.5 and 28.5 was used by McMillin et al. (1993), and the pair J''=5.5 and 28.5 was used by Palmer et al. (1992). The horizontal lines indicate the limits of the useful dynamic range of the detection system.

3.2.4 Experimental Procedure

To ensure an accurate measurement of the laser energy used in the experiment, it was necessary to ensure that the test-section windows were cleaned prior to each tunnel run. The tunnel was then reloaded and pumped to a pressure less than 26 Pa (0.2 Torr). A LIF excitation scan was then performed in the flame which enables monitoring of the laser linewidth and ensured that the laser was tuned to the correct NO transition. The laser was run at 1 Hz while the tunnel was filled. Immediately before firing (< 2 s), the tunnel operator stopped the laser via a remote switch next to the firing valve. After the firing valve was opened, the nozzle-reservoir pressure transducer detected the shock arrival at the end of the shock tube and the laser was fired 450 μs later. The intensified camera and the sheet monitoring camera were also triggered from the nozzle reservoir pressure transducer after a suitable delay. After the run, the data from the cameras was downloaded and recorded on computer. The pressure history from the shock tunnel pressure transducers was recorded on digital oscilloscope and also downloaded to the computer.

Transition	J''	ν (cm^{-1})	$S_{J'J''}$	$F_{J''}$ (cm^{-1})	
Q_1+$^QP_{21}$	5.5	44199.97	0.7689	-1.255	
R_1+$^RQ_{21}$	13.5	44289.83	0.6627	266.168	
$^SR_{21}$	18.5	44430.28	0.1395	542.165	*
Q_1+$^QP_{21}$	27.5	44388.96	0.9004	1248.656	*
Q_1+$^QP_{21}$	28.5	44404.60	0.9040	1343.774	
P_2+$^PQ_{12}$	38.5	44415.63	0.5738	2655.303	*

Table 3.1: NO $A^2\Sigma^+ \leftarrow X^2\Pi(0,0)$ transitions used for PLIF thermometry. Lines used in this work are denoted by an asterisk. The line positions ν given for transition pairs are for the stronger of the two lines. The normalised Hönl-London factors $S_{J'J''}$ and rotational energies $F_{J''}$ are defined in Appendix A.

3.3 Results

3.3.1 Analysis of Cylinder Images

In Fig. 3.6, images (a) to (c) show the corrected PLIF images for each of the three transitions chosen. In each image, the flow is entering from the left and the laser sheet from the top, producing the shadow region beneath the model. Each image is the average of five single-shot images, each of which was corrected for background luminosity and laser energy variation across the sheet. The inset in Fig. 3.6 shows horizontal cross sections through the stagnation region for each image and the temperature map. In image 3.6(a), the signal is strong in the freestream and decreases across the shock as the population of the $J'' = 18.5$ level varies. This image also allows the edges of the nozzle core flow to be observed easily. In images 3.6(b) and 3.6(c), the freestream signal decreases with increasing J'' since these rotational levels are less populated at the freestream temperature.

The temperature map shown in Fig. 3.6(d) was calculated from the three fluorescence images using Eq. 2.68 and assuming $C = 1$. The freestream temperature was determined by using the signals from images 3.6(a) and (b) (*i.e.*, J''=18.5 and 27.5, respectively) and the post-shock temperature was determined by using the signals in images 3.6(a) and (c) (*i.e.*, J''=18.5 and 38.5, respectively).

A freestream temperature of 320 ± 30 K was derived from this image by averaging over a small uniform region in the freestream to reduce random pixel-to-pixel noise. Temperatures of about 3000 K were calculated using STUBE for the stagnation region in front of the body and 2500 ± 900 K is obtained from 3.6(d). The large uncertainty is due to high collisional quenching rates in this region (pressure = 300 kPa) which, as can be seen from images 3.6(a) and 3.6(b), has significantly

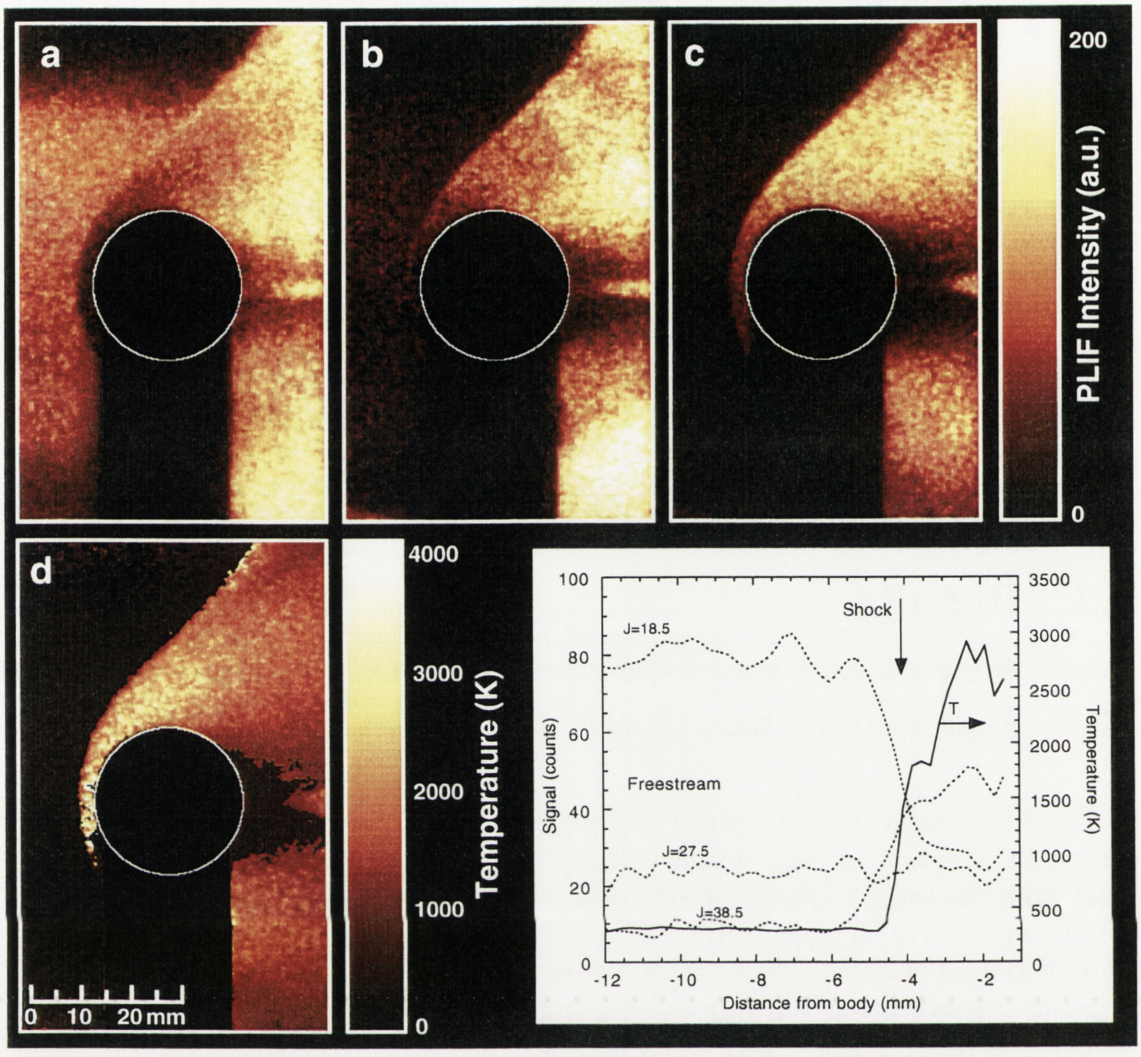

Figure 3.6: PLIF images of the flow over a cylinder. In each image the flow is from left to right and the laser enters from the top. Images (a), (b) and (c) are fluorescence signals produced by exciting the J''=18.5, 27.5 and 38.5 transitions, respectively. Image (d) is the temperature map. The inset shows horizontal cross sections through the stagnation region. Each cross section is a 1 pixel wide slice, except for the temperature slice which is averaged over 15 rows.

reduced the fluorescence signal intensity and hence increased the relative error in the signals due to shot-noise.

The signals in the stagnation region have an average of about 20–30 counts for the J''=18.5 and 27.5 transitions. The signals are shot-noise limited, so the only way to improve the noise with the current camera is to increase the number of photons falling on the photocathode. Some of the ways to increase the signal are: increasing the laser intensity; choosing stronger transitions; reducing collisional quenching

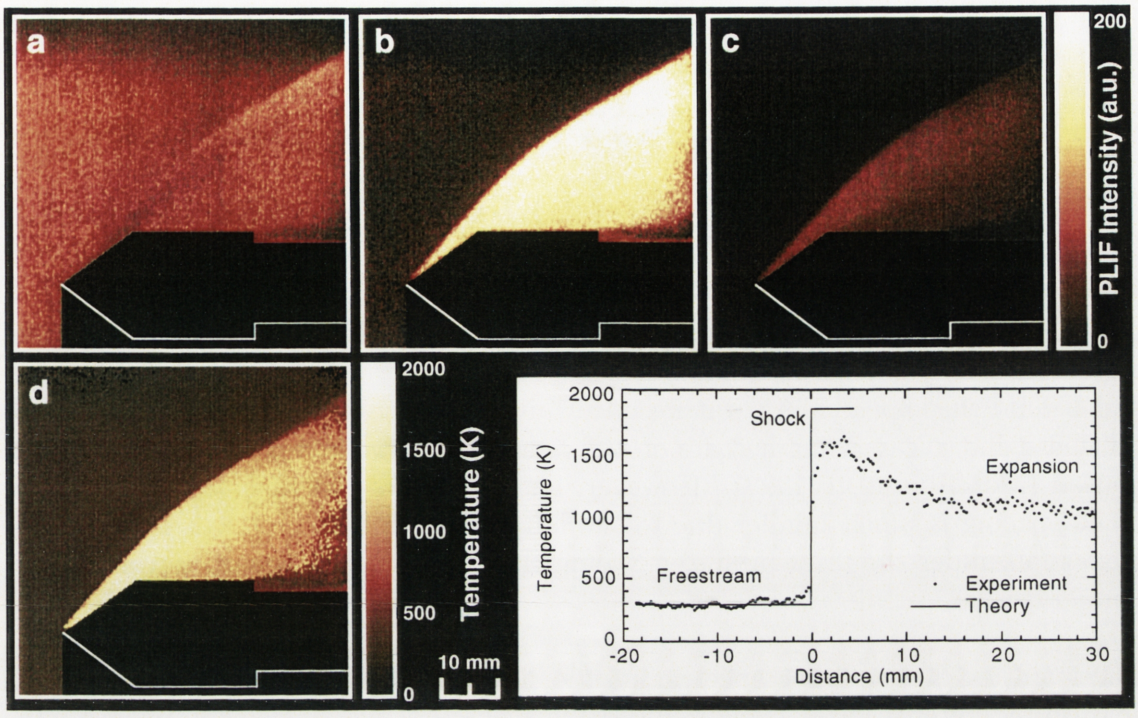

Figure 3.7: PLIF images of the flow over a 35° wedge. In each image the flow is from left to right and the laser enters from the top. Images (a), (b) and (c) are fluorescence signals produced by exciting the J''=18.5, 27.5 and 38.5 transitions, respectively. Image (d) is the temperature map. The inset shows a 1 pixel wide horizontal cross section through the temperature image just above the shoulder of the wedge.

effects by removing species from the flow that have high quench rates (*e.g.*, O_2); improving collection solid angle and efficiency; and improving the transmission of the reflective filter.

3.3.2 Analysis of Wedge Images

For the case of the wedge, the same analysis process as with the cylinder was followed. Fig. 3.7 shows the wedge images for the three transitions used and the derived temperature map. In these images, the oblique shock makes an angle of 49° to the horizontal at the leading edge and then curves as it interacts with the expansion from the corner. The edge of the core flow occurs near the top of the image. The freestream temperature measured here was 300 ± 30 K while behind the shock a maximum temperature of 1500 ± 150 K was measured. The temperature behind this oblique shock calculated using STUBE is about 1800 K. Image 3.7(a)

shows signs of saturation in the freestream which would tend to lower the measured temperatures. This would not be as important behind the shock since the pressure here would significantly increase the collision rate and hence reduce saturation of the transition.

3.3.3 Uncertainties

The main sources of uncertainty for PLIF measurements are shot-noise and pulse-to-pulse fluctuations in the laser spectral profile. Random noise has been reduced in the measurements presented here by averaging over a uniform region in the freestream and behind the shock. Temperature uncertainties due to laser spectral profile fluctuations (due to cavity modes) are on the order of 10% when a broadband dye laser is used (McMillin et al. 1993). However, for the tunable excimer laser the cavity mode spacing is much smaller due to the longer cavity length, and therefore more modes fall under the laser profile, reducing the influence of mode structure on the temperature uncertainty.

Uncertainties due to laser spectral profile fluctuations, tuning inaccuracies and flow reproducibility have been reduced by averaging five single-shot images. In the freestream, the relative error in the fluorescence signal ratio is approximately the same as in the post-shock region. However, the freestream temperature measurement is less sensitive to signal fluctuations due to the more favourable value of $\Delta E/kT$. The uncertainties quoted above are based on estimates of the fluctuations in the signal levels in each region.

The discrepancies between the experimental and calculated temperatures are due to several reasons. First, the accuracy of the CFD temperature calculations relies on accurate knowledge of the freestream pressure and Mach number. The freestream conditions are used by the CFD codes to calculate the conditions behind the shock. Also the accuracy of the vibrational freezing model used has a large impact on the predicted temperatures. An extensive pitot pressure survey of the freestream would significantly improve the reliability of these calculations.

Second, problems with the PLIF technique have also contributed to discrepancies between the experimental and calculated temperatures. Significant laser-beam attenuation can be seen in Fig. 3.6(a), and there is also evidence that some of the transitions are partially saturated. Close examination of the $J'' = 38.5$ image indicates a small but non-negligible amount of signal in the freestream. This signal should not be present at the low temperatures that exist in the freestream for this high-J'' line. Since there are no nearby NO lines that contribute to the signal, we attribute the extra signal to a broadband spectral component of the laser pulse. Dreier et al. (1992) discuss this aspect of tunable excimer lasers, its causes and possible solutions. It is difficult to estimate the uncertainty that this broadband component

might introduce to the temperature measurement as it varies with wavelength and also fluctuates on a pulse-to-pulse basis.

For the temperatures and pressures considered in this experiment, contributions to the fluorescence signal from O_2 is negligible.

3.3.4 Higher Enthalpy Shots

Several shots were performed at a 14 MJ kg^{-1} condition to ascertain the effectiveness of the filtering used to eliminate the background contaminant emission. With the 35° half-angle symmetric wedge, we observed only a small amount of flow luminosity near the leading edge of the wedge. However, with the cylinder there was significant luminosity even at the 4.1 MJ kg^{-1} condition. For bluff-body work at higher enthalpies it would be necessary to improve the spectral filtering, and perhaps also the camera gating.

This tailored high-enthalpy condition was achieved with the following shock tunnel parameters: reservoir 4.34 MPa (630 psi) of air; compression tube 118.6 kPa (17.2 psia) mixture of He with 5.7% Ar; shock tube 30 kPa of air (BOC instrument grade). The diaphragm was the same as the low-enthalpy condition — mild steel of thickness 0.74 mm (0.029 inches) with a burst pressure of 46.9 MPa (6800 psi). The measured shock speed was 4.0 km/s and the nozzle reservoir pressure was 24.5 MPa.

3.4 Discussion

The aim of these experiments was to test if PLIF could be applied quantitatively to free-piston shock tunnels. The results indicate that this is feasible but that careful attention should be made to the following points in order to reduce experimental error:

- flow luminosity should be minimised by using reflective filters and short detector gating times. There was 40 ns of jitter in the delay between the camera gate opening and the laser firing. In this case, it was necessary that the gate was long enough to collect all of the fluorescence. When the gate is five times the fluorescence lifetime in duration, greater than 99% of the fluorescence is collected. If there were no time jitter, then the gate should be made as small as possible to maximise the signal-to-luminosity ratio.
- tuning via LIF in a flame was used here since this allowed the high-J'' transition to be observed. A cell containing NO could also be used for low-J'' lines

but since the collision-shift would be different between cell and flame, one or the other method should be used for all transitions but not both. Therefore, the laser should be tuned to each transition using the same technique to ensure that the overlap integral cancels in the signal ratio.

- interference from nearby transitions should be avoided by choosing isolated transitions. This should be checked for the range of temperatures and pressures to be encountered in the flowfield.
- interference from other chemical species should be avoided. For the NO γ-bands, interference from O_2 is the biggest concern.
- the laser energy measurement should be made as accurately as possible since it directly affects the PLIF signal. The spatial variation of the laser sheet should also be measured.
- radiative trapping can be avoided by using spectral filters that collect fluorescence from bands that terminate in less-populated vibrational levels.
- beam attenuation can only be avoided by choosing weakly absorbing transitions or varying the composition of the flow. When the composition of the flow can't be changed, pumping the less-populated (0,1) band near 237 nm can be employed to reduce the beam attenuation significantly.
- partial saturation of the transitions can also cause systematic errors.

This is by no means an exhaustive list, but summarises the more important points. Note that partial saturation and beam attenuation may be tolerated if it affects all the excitation transitions in the same manner. This *isointensity* approach requires choosing lines with similar line strengths, and through a rough knowledge of the temperature in the flow, similar absorption coefficients.

For the utilisation of the Raman-shifted tunable-excimer laser as a PLIF excitation source, we note the following:

- the tuning range is limited, which reduces the possibilities for line selection. A frequency-doubled dye laser would open up greater line selection possibilities and even the excitation of higher vibrational bands.
- a broadband component associated with the laser spectral profile causes weak excitation of nearby lines and therefore systematic error. The improvements of Meijer et al. (1986) may eliminate this problem.
- the stability of laser linewidth and wavelength was poor for the excimer laser used in these experiments, therefore introducing another random variable.

- cavity mode structure is less of a problem for the tunable-excimer laser than for a dye laser due to the longer cavity length.

If the problems associated with the broadband component and stability can be overcome or minimised, then the Raman-shifted tunable excimer laser can certainly be an effective excitation source for PLIF. However, the temperature range over which measurements can be performed remains limited to approximately 300 to 3000 K due to the small tuning range.

In Fig. 3.6, it can be seen that the width of the shadow is less than the model size. This effect is caused by the edge of the cylinder nearest the camera appearing larger than the cylinder cross section in the plane of the laser. This perspective effect partially obscures the fluorescence signal near the body. A similar effect occurs in the wedge case however it is not as obvious. The use of axi-symmetric models would alleviate this problem, but as mentioned previously, calculations of three-dimensional flows require significantly more labour. Also, with two-dimensional models the flow luminosity is integrated up along the line of sight of the camera. By using axi-symmetric models the amount of luminosity along the line of sight of the camera would be significantly reduced.

3.5 Summary and Suggested Improvements

PLIF imaging of NO in a shock-tunnel using a Raman-shifted tunable excimer laser flow has been presented. Hypersonic air flows over a cylinder and a wedge have been studied. The measured freestream temperatures show excellent agreement with theory and the measured temperatures behind the shock for the cylinder case agree to within experimental error. Shots performed at 14 MJ kg^{-1} on a wedge demonstrate the effectiveness of the filtering employed to remove background emission.

Some possible ways to improve the temperature measurements are:

- using a narrowband dye laser to increase the laser tuning range. It should be possible to find suitable transitions that reduce the effects of beam attenuation due to excessive absorption and the effects of transition saturation. This would also increase the possible temperature range of measurements, and allow excitation of higher vibrational bands for the reduction of beam attenuation and also the measurement of vibrational temperatures.
- improving the spectral and temporal filtering of the detection system to more effectively eliminate flow luminosity.

- improving the stability and character of the laser linewidth either by changing lasers or having a monitoring system is place. This could also be used to improve the accuracy of tuning to transitions.
- the use of axi-symmetric models would remove the shadowing effects caused by the two-dimensional models, and reduce flow luminosity.
- a nitrogen flow condition (with a trace amount of NO) should be used as a base measurement to reduce the effects of beam attenuation and interference from O_2. O_2 is also a major quencher of NO fluorescence and so an increase in signals would be expected.
- a pitot-pressure survey of the nozzle should be used to get a better idea of the nozzle-exit conditions.

In the next chapter we will investigate the operating conditions and performance of the shock tunnel. Chapter 5 will be concerned with addressing the concerns mentioned above relating to the PLIF measurement system.

Chapter 4

Shock-Tunnel Flows

4.1 New Operating Conditions

Four new operating conditions were designed to aid in the ongoing development of laser-diagnostic techniques and for CFD code validation. From both of these points of view, it is desirable to begin with simple flows and gradually increase the physical complexity (*e.g.*, by introducing chemical reactions). This allows the analysis of individual flow phenomena without interference from competing effects that may compromise data interpretation (see Chap. 1). For example, LIF signal interferences caused by laser excitation of O_2 can be minimised by designing a flow condition with a reduced concentration of O_2. The conditions used in Chap. 3 suffered from several competing effects and hence it is the purpose of the current section to identify what attributes are desirable when designing a new operating condition. By careful choice of the shock-tunnel operating conditions, it is possible to influence the level of vibrational and chemical activity, the chemical composition, the enthalpy (which affects flow luminosity, chemistry etc.) and the temporal behaviour of the reservoir and freestream conditions. These properties are discussed below in reference to the new conditions.

The first flow condition is a low-enthalpy N_2 condition.[†] For PLIF of NO, the amount of NO present in the freestream plays a critical role. Too much NO causes the laser beam to be significantly attenuated as it passes through the flow, whilst too little prevents the fluorescence signal from being observable. A compromise value of 1% was used here. The effects of chemistry are minimal for this condition because

[†]An argon condition was considered for the purpose of simulating a monatomic perfect-gas flow. However, in order to get a suitable amount of NO present in the freestream it was necessary to have a significant amount of N_2 or NO in the test gas (10%), which causes significant deviation from perfect-gas behaviour. Also, the O_2 freestream mole fraction was found to be 3 to 4 times greater than NO. These calculations were performed with STUBE.

it is low enthalpy and the test gas is composed mainly of N_2. However, vibrational excitation at the nozzle-reservoir temperature is significant and "freezing" of the vibrational temperature occurs during the nozzle expansion. Hence it is possible to use this condition to test vibrational-freezing models by comparing measurements of rotational and vibrational temperatures with CFD calculations. The low total enthalpy (5 MJ/kg) also ensures that flow luminosity will not be an insurmountable problem. This condition will be denoted as N_2 I.

The second operating condition is a low-enthalpy condition (5 MJ/kg) with air as the test gas (denoted as Air I). For this condition, the freestream contains significant amounts of oxygen atoms (0.4%), oxygen molecules (17%) and nitric oxide (7%). The N_2 I and Air I conditions both use exactly the same operating conditions apart from the initial test-gas composition. The third condition was a medium enthalpy (13 MJ/kg) condition with air as the test gas (denoted as Air II). At this higher enthalpy, real-gas effects are expected to occur. Finally a fourth condition (denoted N_2 II) was obtained by replacing the test gas in Air II with 1% O_2 in N_2.

The laser-induced fluorescence signal from NO is strongly dependent on the atomic and molecular oxygen concentrations in the flow. This is because O and O_2 are very efficient quenchers of electronically-excited NO molecules. Molecular oxygen also has absorption lines in the same spectral region as NO which may lead to laser-induced fluorescence from O_2 molecules contributing to the overall observed fluorescence signal. Thus, these contributions may cause significant errors in temperature measurements. The low-enthalpy N_2 condition, which has low concentrations of O and O_2 in the freestream (0.4% each), can therefore be used to ascertain the effect of quenching by O and O_2 and possibly the effects of interference with O_2 absorption lines.

It is desirable for the nozzle-reservoir conditions to remain steady throughout the period in which the laser measurement is performed. This eliminates the need for assumptions about the steadiness of the flow in the test section. It also reduces uncertainty in determining the nozzle-reservoir pressure at the time of the laser measurement. The nozzle-reservoir pressure is used to calculate the nozzle-reservoir conditions. A constant nozzle-reservoir pressure can be achieved by varying the operating conditions to *tune* the piston motion, resulting in a so-called "soft-landing" of the piston which is necessary to minimise piston damage (Hornung and Bélanger 1990, Itoh 1996). Tuning also has an influence on the test-time duration (see Sect. 4.2.3).

From this brief analysis we can summarise the desirable attributes for an operating condition which is to be used for development of the PLIF measurement technique. They are: low enthalpy (low flow luminosity and chemistry); nitrogen flow (low chemistry); low oxygen concentration (minimal interference with NO LIF); approximately 1% NO in freestream (low beam attenuation, but adequate signal); and tuned operating condition (minimal uncertainty in nozzle-reservoir pressure). The

N_2 I condition provides the condition with the least number of competing effects for the development and application of PLIF to the shock tunnel.

In line with the recommendations of Chap. 3, a pitot-pressure survey of the nozzle-exit conditions was performed to help characterise the freestream conditions. This tested the nozzle-exit flow quality and also determined the effect of boundary-layer growth on the nozzle expansion. Only the N_2 I condition was used for the remaining PLIF experiments in this thesis although a pitot-pressure survey was also conducted on Air I and Air II and the results summarised at the end of this chapter. No measurements were made for the N_2 II condition, but it is reasonable to expect similar pressure data as for the Air II condition because the pitot-pressure measurements are insensitive to the thermochemical state of the flow.[†]

The aim of this chapter is to describe the operation of the T2 shock-tunnel facility, the operating conditions, and the results of the pitot-pressure survey.

4.2 The T2 Shock Tunnel

The T2 shock tunnel was constructed in the mid-sixties and is the prototype for the larger T3 facility. Although much smaller in size, it is still capable of producing high-enthalpy flows and is still in extensive use today. Its primary function now is, however, to aid in the development of sophisticated measurement techniques, rather than to realistically simulate re-entry type flows. Its smaller size contributes significantly to its fast turnaround times (30 minutes) and ease of operation.

Figure 4.1 shows a schematic of the T2 shock tunnel (Stalker 1967). A 1.20-kg[‡] piston is free to move inside the 3.1-m compression tube which has an internal diameter of 76 mm. The shock tube is 1.98 m in length and has an internal diameter of 21 mm. Attached to the end of the shock tube is a converging-diverging nozzle which exits into a test section which has optical access through 4 window ports. For the current experiments, the primary diaphragm was made from mild steel and was 0.74-mm (0.029-inches) thick, which corresponds to a burst pressure of 46.9 MPa (6800 psi). The secondary diaphragm was made from 0.025-mm-thick (0.001-inches) mylar.

The present study employed a 7.5° half-angle axisymmetric conical nozzle as shown in Fig. 4.2. The throat of the nozzle is 6.35 mm in diameter, the length of the expanding section is 255 mm and the nozzle-exit diameter is 73.6 mm. Contoured

[†]For example, while the nozzle-exit temperature varies by 20–30% between the cases of vibrationally frozen and equilibrium flow, pitot pressure varies by only 2%. These calculations were performed with STUBE which is described in Sect. 4.5.

[‡]Add 25 g for o-rings and nylatron piston rings.

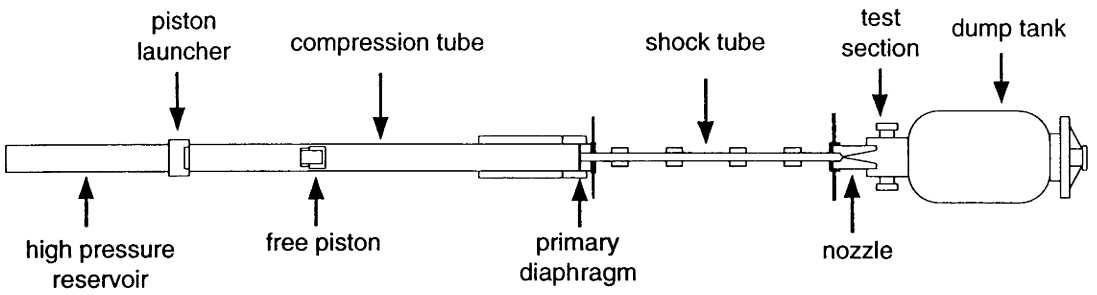

Figure 4.1: The T2 free-piston shock tunnel.

nozzles can be used to produce parallel flow at the nozzle exit. However, it has been shown that contoured nozzles can focus disturbances onto the centreline of the flow (Mudford 1992, Hannemann et al. 1996). In addition, the flow produced by contoured nozzles becomes unstable when operated far from the design conditions (Burke and Bird 1962). On the other hand, conical nozzles suffer from radial and axial flow gradients which may be significant for slender body studies. These gradients should be characterised so that they can be included in calculations of the nozzle-flow conditions.

4.2.1 T2 Operating Conditions

Table 4.1 shows the operating conditions for T2. The only parameters that were varied between the three conditions were the initial shock tube pressure P_1, test gas composition and the argon-to-helium ratio of the driver gas. The initial compression-tube total pressure C, the reservoir pressure R, and the diaphragm rupture pressure D, were all held constant. The compression ratio is given by

$$\lambda = \left(\frac{D}{C}\right)^{\frac{1}{\gamma}} , \tag{4.1}$$

where γ is the ratio of specific heats for the driver gas ($\frac{5}{3}$ for argon and helium). The ratio of argon to helium in the driver gas was varied in order to control the piston motion and produce a *tuned* nozzle-reservoir pressure trace.† The driver was approximately 30% and 6% argon for the low-enthalpy and high-enthalpy conditions, respectively. For all conditions, C = 118.6 kPa (17.2 psia) and D = 46.9 MPa

†*Examiner's note:* A much more important consideration is the effect that the argon has on the enthalpy of the test flow.

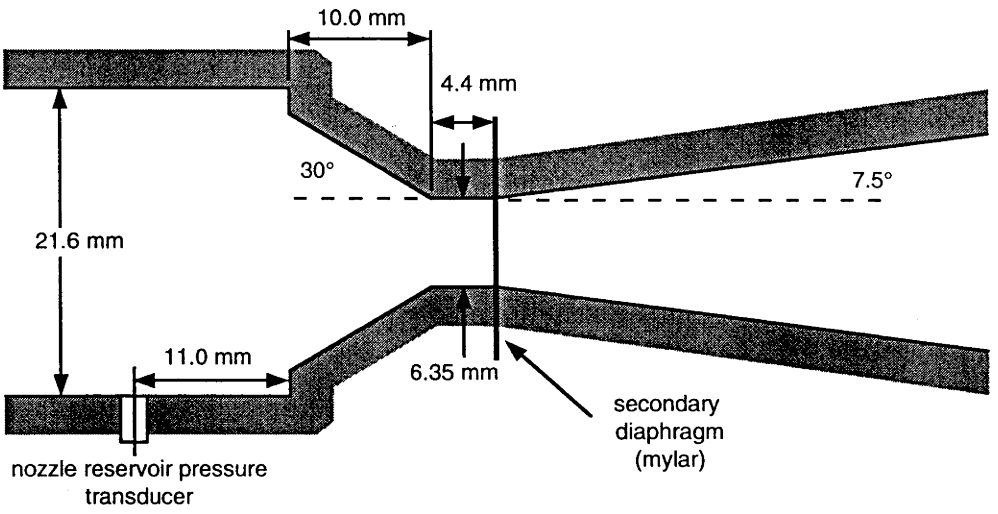

Figure 4.2: The T2 nozzle inlet geometry.

(6800 psi) which gives a compression ratio of $\lambda = 36.2$. The shock tube constant, K, is defined by

$$K = \frac{R\lambda}{D} \,. \tag{4.2}$$

For correct (*i.e.*, safe) operation of T2, it is held constant at approximately 3.3. The reservoir pressure was $R = 4.34$ MPa (630 psi) of air.

For the N_2 conditions, the test gas was $1.10 \pm 0.02\%$ of O_2 in N_2, while the air conditions used high-purity bottled air.

4.2.2 Pressure and Shock-Speed Measurements

The nozzle-reservoir pressure is measured with a PCB transducer (P/N 113A23, S/N 5960, 0.521 mV/psi) which is located 11 mm from the shock-tube end wall (Fig. 4.2). The average shock speed along the shock tube is determined from the transit time between the primary timing station (PCB P/N 111A22, S/N 6053) and the nozzle-reservoir pressure transducer. The distance between the stations is 1270 mm. The shock timing for each run is determined to within 1 μs from digital-storage oscilloscopes.

Condition	Compression tube initial pressure C (kPa)	Shock tube pressure P_1 (kPa)	Test gas composition
N_2 I	37.3 Ar, 81.3 He	100.0	1.1% O_2 in N_2
N_2 II	6.8 Ar, 111.8 He	40.0	1.1% O_2 in N_2
Air I	37.3 Ar, 81.3 He	100.0	Air
Air II	6.8 Ar, 111.8 He	40.0	Air

Table 4.1: The T2 operating conditions. For all conditions, D=46.9 MPa, R=4.34 MPa, the compression ratio λ is 36.2 and the shock tunnel constant, $K = R\lambda/D$, is 3.34.

To estimate the degree of shock-speed attenuation due to viscous effects, three transducers were used for several tunnel runs. A third transducer was placed 305 mm upstream of the nozzle-reservoir transducer. Figure 4.3 shows the transducer locations and the speeds determined from the transit times between the transducers. The speed can be extrapolated to the nozzle-reservoir region assuming the speed decreases in a linear fashion. For the pitot-pressure survey and PLIF experiments, the overall average speed was determined from the transit time between the first timing transducer and the nozzle-reservoir transducer. It is found that the extrapolated speed is 6.3 ± 0.5 % lower than the overall average for the low and high-enthalpy conditions. In the calculations below, the shock speed, corrected for attenuation, is used to determine the nozzle-reservoir conditions.

4.2.3 Test Time Limitations

Steady flow is established in the test section after the nozzle start-up processes (Smith 1966) have ceased and continues until the arrival of the driver gas. However, after an initial constant period, the reservoir pressure begins to fall due to either drainage of the test gas into the nozzle or piston-tuning effects. Figure 4.4 shows some typical nozzle-reservoir pressure traces. Although the current operating conditions are tuned, the nozzle-reservoir pressure is only constant between approximately 100 and 350 μs for the low-enthalpy condition and between approximately 50 and 200 μs for the high-enthalpy condition. Here, the times are measured from the primary shock arrival at the nozzle-reservoir transducer, approximately 10–15 μs before shock reflection. As the nozzle-reservoir pressure begins to fall, so does the the pressure at the nozzle exit.

The nozzle-transit time, t_{NT}, is the time required for a fluid element to flow from the reservoir to the model location. It is approximated for the current experiments by the shock-transit time, or, the time required for the primary shock to traverse the

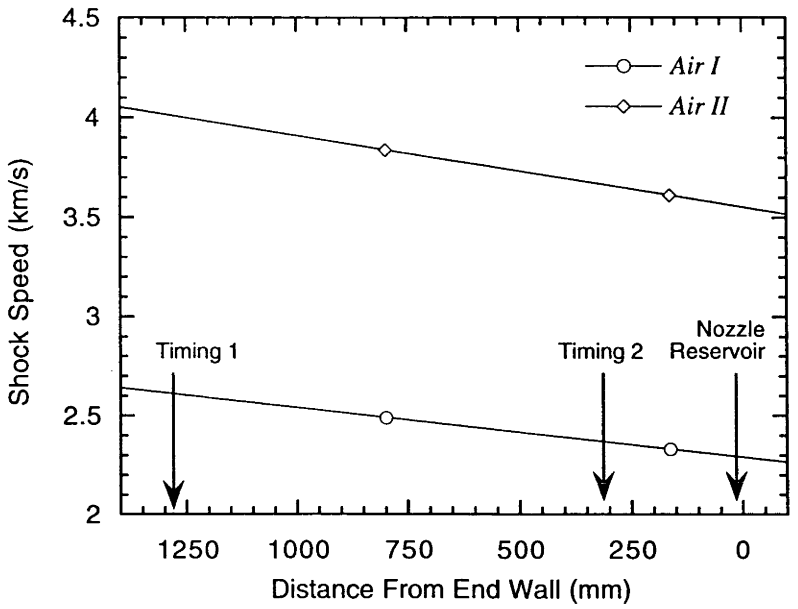

Figure 4.3: The speed of the primary shock is attenuated by viscous effects in the shock tube. Linear extrapolation is used to estimate the decrease in shock speed in the nozzle-reservoir region.

nozzle. For a nozzle-reservoir pressure which is changing with time, the freestream conditions at a time t are given by the nozzle-reservoir conditions at the time $t-t_{\mathrm{NT}}$. For Air I and Air II, t_{NT} = 67 and 46 μs respectively. Transit times for the N_2 conditions are the same as for the air conditions.

Figure 4.4(a) shows a 200 μs pressure plateau of approximately 28 MPa which then steadily decays at about 2 MPa per 100 μs. For the N_2 I and Air I conditions, the time of laser firing is at 350 μs (henceforth called the laser-time). Figure 4.4(b) shows the pressure traces for the high-enthalpy air condition. The period of constant reservoir pressure is significantly less ($\approx$ 150 μs) but the pressure decay rate is similar to the low-enthalpy condition (2 MPa per 100 μs). The laser-time for the condition was chosen to be at 250 μs. For both conditions, the laser-time corresponds (by design) to the end of the constant nozzle-reservoir pressure plateau (allowance has been made here for the nozzle transit time). This reduces uncertainty in the nozzle-reservoir pressure at the time of the laser-based measurement. The values for the nozzle-reservoir pressures were averaged over a large number of shots (40 for Air I; 20 for Air II) to arrive at averaged values. The averaged nozzle-reservoir pressure then served as a nominal value for calculation of the nozzle-reservoir and nozzle-exit conditions (Sect(s). 4.4 and 4.5).

Previous experimental work on T2 suggests that steady flow commences at about 100 μs after shock reflection and continues for a further 300 and 100 μs at low and

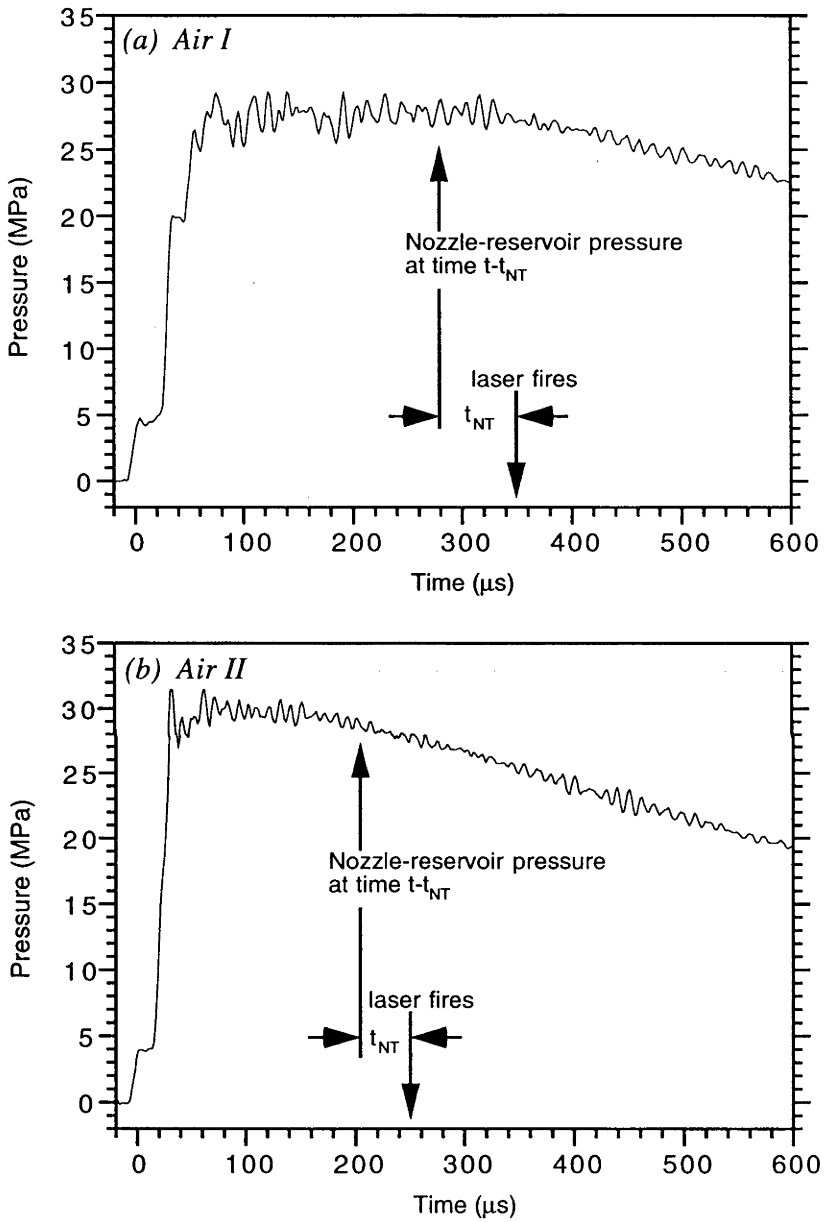

Figure 4.4: Typical nozzle-reservoir pressure traces for (a) Air I (b) Air II. The pressure traces for N_2 I and N_2 II appear the same as for the corresponding air conditions.

high enthalpies, respectively (Ebrahim 1975). Stalker and McIntosh (1973) used schlieren photographs of flow over a 35° wedge at different delays to determine the useful test time. They found the shock angle achieved a steady value and then rose some time after due to the arrival of helium in the test section. Kewley (1975) employed the same method for experiments in T2. However, he cautions that this method may overestimate the test time. To obtain good agreement with theoretical calculations of shock angles, it was necessary to make corrections for both flow divergence and boundary layer growth on the wedge. Kewley (1975) also used static pressure measurements on a flat plate, in conjunction with the wedge shock angles determined from interferograms, to determine the test time. However, despite being performed on the same facility with the same nozzle, the test times determined do not easily relate to the current operating conditions which use argon/helium drivers to produce tuned nozzle-reservoir pressure traces.

Surface heat-transfer measurements on flat plates (East et al. 1980) and mass spectrometry (Skinner and Stalker 1994, Slade et al. 1993, Stalker and Crane 1978, Crane and Stalker 1977) have also been used to determine driver gas arrival in free-piston shock tunnels. Mass spectrometry is generally considered the most suitable method for detecting small amounts of driver gas. However, the complexity and size of the apparatus do not make it a readily employable technique. To overcome this, Paull and King (1995) and Paull (1996) developed a simple gas-dynamical detector which consists of a duct which remains unchoked for uncontaminated flow and chokes when the flow achieves a certain level of contamination. A modified version utilising an inclined duct for higher sensitivity to driver-gas concentration was developed by Sudani and Hornung (1998) for use in the T5 shock tunnel. The results from these duct experiments agree well with the driver-gas arrival times predicted by the simple reflected-shock bifurcation theory of Davies and Wilson (1969). Sudani and Hornung (1998) also demonstrated the delayed onset of driver-gas contamination by use of slightly under-tailored[†] operating conditions, and the premature arrival of driver gas for over-tailored conditions. Numerical simulations of the shock tunnel dynamics by Chue and Itoh (1996) showed similar results for under-tailored conditions.

Early arrival of driver gas may be explained by jetting of cold driver gas into the nozzle-reservoir region via shock wave/boundary layer interaction (Davies and Wilson 1969, Stalker and Crane 1978). To overcome this, Dumitrescu (1996) proposed a boundary-layer suction technique which uses a slit in the shock-tube end wall to capture the boundary layer. However, implementation of this method on T5 by Sudani and Hornung (1997) produced negative results—the onset of driver-gas contamination was never delayed.

[†]Tailoring refers to the interaction of the reflected shock with the driver-gas/test-gas interface (contact surface). A tailored condition is one in which the reflected shock brings the contact surface to rest; under-tailoring occurs when the contact surface is moving away from the end wall after interaction with the reflected shock; and over-tailoring occurs when the contact surface is moving towards the end wall.

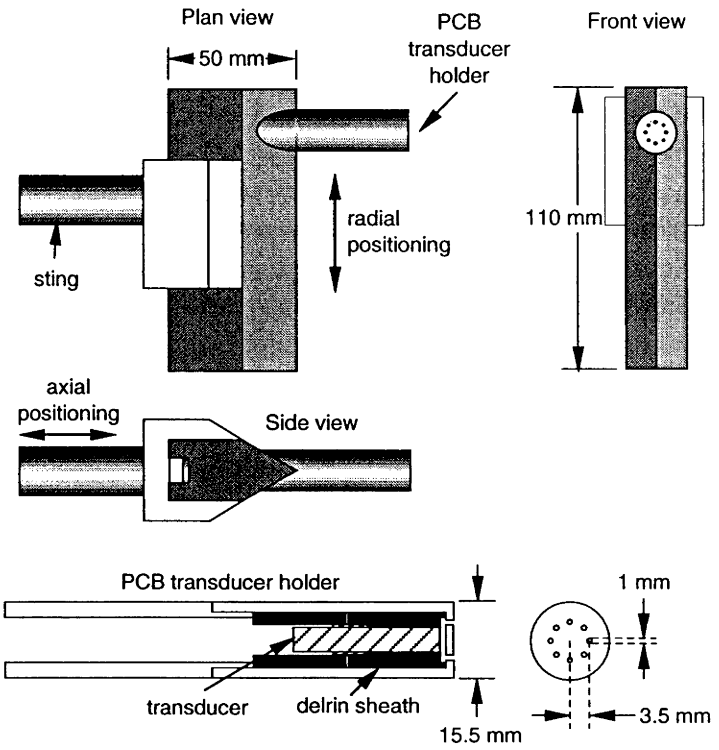

Figure 4.5: Schematic of pitot rake used in nozzle survey. The PCB transducer holder is shown enlarged.

No systematic study was undertaken in the current work to determine the arrival of the driver gas. Therefore the possibility exists that a significant level of contamination by driver gas may exist at the time of the laser measurement.

4.3 Pitot Pressure Survey

Pitot-pressure measurements still remain the standard way of calibrating nozzle-flow calculations for shock tunnels. However, pitot pressure is very insensitive to the chemical and thermodynamic state of the freestream, so caution is required when drawing conclusions from comparisons with CFD simulations. This again emphasises the need for freestream measurements of rotational and vibrational temperatures and species concentrations. Nevertheless, the pitot pressure can be used to determine the uniformity of the flow at the nozzle exit and also account for boundary-layer growth on the nozzle walls.

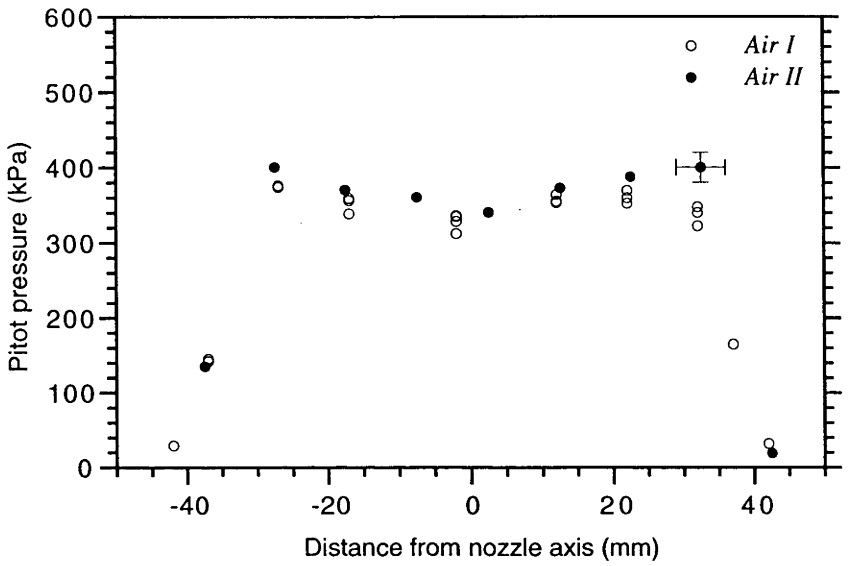

Figure 4.6: Flow uniformity at the nozzle exit. The measurements were taken at 28±2 and 16±2 mm from the nozzle exit for the Air I and Air II conditions, respectively.

A pitot pressure survey was conducted to characterise the nozzle-exit conditions. A schematic of the pitot rake is shown in Fig. 4.5 and includes a detailed view of the pressure transducer holder. A pressure transducer (PCB P/N 112A21, S/N 10663, 52.3 mV/psi) was mounted in the tube which has several 1-mm-diameter holes in one end to allow the gas to flow into the space in front of the transducer. This mounting protects the transducer from damage due to particulate matter in the flow. The transducer was positioned in the pitot rake which could be adjusted for different radial and axial positions at the nozzle exit. The signal from the pitot pressure transducer, along with the nozzle-reservoir pressure and timing-transducer outputs, were recorded on 2 digital storage oscilloscopes (Tektronix Model 2232). These signals were later transferred to a computer. Due to the large diameter of the transducer holder (15.5 mm), the spatial resolution of the pressure measurements was limited.

4.3.1 Flow Uniformity at Nozzle Exit

Figure 4.6 shows radial measurements of the pitot pressure at the nozzle exit. The pitot pressure was normalised for each tunnel run by the nozzle-reservoir pressure, and then multiplied by the averaged nozzle-reservoir pressure for the condition. This process gives a pressure in kPa which has effectively been corrected for the shot-to-

shot fluctuations in the pressure signals. The uncertainty indicated in Fig. 4.6 has been estimated to be ±20 kPa from the oscillations in the pitot pressure signal. The shock tunnel recoil of 9 ± 1 mm was included in the determination of the pitot-probe axial position at the nozzle exit. Figure 4.6 indicates a 60-mm-diameter core flow. The pressure increases in a linear fashion by approximately 15% between the centre of the flow and the edge. The cause of this pressure rise is not evident at this time, but is possibly related to the divergent nature of the flow.

4.4 Nozzle-Reservoir Conditions – ESTC

The nozzle reservoir conditions are calculated using the one-dimensional equilibrium shock tube code ESTC (McIntosh 1968). The inputs to ESTC are the primary shock speed u_s, the nozzle-reservoir pressure P_0, and the initial temperature T_i and pressure P_i of the shock tube. Thermophysical data relating to the elemental composition and electronic properties for each chemical constituent of the test gas is also input to the code. The reflected shock conditions are calculated using the conservation equations and then an isentropic expansion or compression is used to bring the calculated reflected shock pressure into agreement with the measured reservoir pressure. This expansion or compression corresponds to wave processes in the reservoir region which are caused by the interaction of the reflected shock with the contact surface and drainage into the nozzle. Equilibrium vibration and chemistry is assumed throughout, since the flow is brought to rest and, therefore, the characteristic flow time is much longer than the characteristic reaction time. Table 4.3 summarises the nozzle-reservoir conditions calculated using ESTC, with the uncertainties determined from varying each of the input parameters.

ESTC assumes that the flow is one-dimensional and inviscid. Viscous effects that reduce the shock speed (*e.g.*, wall boundary layers) are partially taken into account by the estimation of shock attenuation. Other effects such as heat losses due to radiation and conduction, shock tube impurities, and driver gas are not included. Jetting of cold driver gas into the nozzle-reservoir region via shock wave/boundary layer interaction may cause significant errors in the calculation (Davies and Wilson 1969).

4.5 Nozzle-Exit Conditions – STUBE

The nozzle-exit conditions are calculated using the quasi-one-dimensional nozzle flow code STUBE (Vardavas 1984). The gas in the nozzle reservoir is in thermochemical equilibrium due to the high pressure and temperature: however, as it rapidly expands through the nozzle, chemical and vibrational nonequilibrium effects

begin to dominate. The reservoir pressure P_0 and temperature T_0 serve as inputs to the code along with the nozzle shape and the necessary thermophysical and reaction rate data. All the calculations presented here used chemical nonequilibrium capabilities of STUBE (the code can also be run assuming chemical equilibrium). The excitation of vibrational modes could be frozen at the reservoir values, kept in equilibrium, or allowed to "freeze out" at some particular temperature during the expansion. The nozzle-exit conditions are summarised in Table 4.3.

4.5.1 Vibrational Freezing Model

To determine the vibrational-freezing temperature T_v, a vibrational-relaxation length l_v was calculated at each point along the nozzle centreline using the Landau-Teller model. This value was compared with the characteristic flow length l_f required for the vibrational energy to fall to $1/e$ of its local value.

The vibrational-relaxation time τ, according to the theory of Landau and Teller, is given by

$$\tau = C \, \frac{\exp(K_2/T)^{\frac{1}{3}}}{p} \, , \tag{4.3}$$

where T and p are the local temperature and pressure, and C and K_2 are constants which depend on the physical properties of the molecule (Vincenti and Kruger 1975, p. 204). The vibrational-relaxation time is then multiplied by the local velocity to give the local vibrational-relaxation length l_v. The constants are determined from fits to experimental data, which are very scarce, and which are also limited in the temperature range over which they are applicable (*e.g.*, 800–6000 K for N_2). The values used here are from Vincenti and Kruger (1975, p. 205). Due to the lack of data, only N_2-N_2, O_2-O_2 and NO-NO vibrational interactions are considered. When the flow contains more than one collision partner, the collision partner with the smallest value of C is chosen. The remaining species are assumed to have the same effectiveness in vibrational relaxation as the dominant partner. This causes the vibrational relaxation length to be under-predicted and leads to lower vibrational-freezing temperatures. With less energy trapped in the vibrational modes, the translational/rotational temperature is higher.

Equation 4.3 has many limitations. It is derived for diatomic molecules that are harmonic oscillators. The energy level transitions are so called "translation-vibration" (T-V) transfers where energy is exchanged between the translational and vibrational energy modes. However, in reality all molecules are anharmonic and other transfer mechanisms such as "vibration-vibration" (V-V) transfers are also important. Gilmore et al. (1996) observed that V-V transfers were significant in expanding N_2/O_2 mixtures. Other effects such as vibration-dissociation coupling have also

Condition	Vibrational Modes		
	Frozen	Nonequilibrium	Equilibrium
N_2 I	318	396	509
Air I	315	407	506
N_2 II	818	1108	1441
Air II	878	1098	1246

Table 4.2: Rotational temperatures at the nozzle exit (285 mm from throat) for different types of vibrational modelling.

been ignored (Olejniczak 1997).

The characteristic flow length l_f is approximated by first calculating, at each step along the nozzle expansion, the vibrational energy E_v from the local temperature T given by STUBE using (Vincenti and Kruger 1975)

$$E_v = \frac{\Theta_v}{\exp(\Theta_v/T)} \frac{\mathcal{R}}{\mathcal{M}} , \tag{4.4}$$

where Θ_v is the characteristic temperature for vibration of the molecule, $\mathcal{R}$ is the universal gas constant and $\mathcal{M}$ is the molecular weight. The rate of change of E_v is determined from the difference in E_v between successive steps, and a crude estimate for the vibrational energy to fall to $1/e$ of its local value is obtained from

$$l_f = \frac{E_v}{dE_v/dx} . \tag{4.5}$$

The vibrational temperatures are obtained by first performing an equilibrium vibration calculation and monitoring when the value of $\log(l_f/l_v)$ changes from positive to negative. The first molecular species to achieve this criterion is deemed to have frozen first and, on successive runs, is made to freeze out at this temperature. The process is repeated until vibrational freezing temperatures are obtained for all of the molecules. In the present case, only N_2, O_2 and NO were considered since they were the primary constituents of the flow. A comparison of the rotational temperatures at the nozzle exit are shown in Table 4.2. In each case, the temperature determined with the nonequilibrium vibrational model falls approximately halfway between the two extremes (*i.e.*, vibrational temperatures frozen at the nozzle reservoir temperature and vibrational temperatures in equilibrium with translational temperature).

4.5.2 Nozzle-Angle Corrections

The nozzle used in the experiments was a 7.5° half-angle conical nozzle. As the flow in the nozzle is established, boundary layers develop on the nozzle walls. STUBE assumes inviscid flow, so in order to correct for the effect of boundary layers, a reduced nozzle angle is used in the calculations. The effective angle, θ_{eff}, is determined by comparing pitot pressure measurements along the nozzle centreline with pitot pressure calculations from STUBE. The effective nozzle angle is varied until the best agreement between theory and experiment is found.

The pitot pressure P_{pitot} for a perfect gas is given by (Liepmann and Roshko 1957)

$$\frac{P_{\text{pitot}}}{P_\infty} = \frac{\left(\frac{2\gamma}{\gamma+1}M_\infty^2 - \frac{\gamma-1}{\gamma+1}\right)^{\frac{1}{\gamma-1}}}{\left(\frac{\gamma+1}{2}M_\infty^2\right)^{\frac{\gamma}{\gamma-1}}} , \tag{4.6}$$

where P_∞ and M_∞ are the freestream pressure and Mach number and γ is the ratio of specific heats. Equation 4.6 is known as the *Rayleigh supersonic pitot formula*. Rearranging Eq. 4.6, subtracting $\frac{2}{\gamma M_\infty^2}$ from both sides, and noting that $\frac{1}{2}\rho_\infty u_\infty^2 = \frac{\gamma}{2}P_\infty M_\infty^2$, gives

$$\frac{P_{\text{pitot}} - P_\infty}{\frac{1}{2}\rho_\infty u_\infty^2} = \frac{\gamma+1}{\gamma}\left[\frac{(\gamma+1)^2 M_\infty^2}{4\gamma M_\infty^2 - 2\gamma + 2}\right]^{\frac{1}{\gamma-1}} - \frac{2}{\gamma M_\infty^2} , \tag{4.7}$$

where ρ_∞ and u_∞ are the freestream density and velocity respectively. For a strong shock ($P_{\text{pitot}} \gg P_\infty$) this simplifies to

$$P_{\text{pitot}} \approx 0.91\rho_\infty u_\infty^2 , \tag{4.8}$$

where we have assumed $\gamma = 1.4$ (air) and $M_\infty = 7$.

When the perfect gas assumption fails, such as with chemically reacting and vibrationally excited flows, a more sophisticated analysis is required. This involves determining the stagnation conditions for the pitot probe at the freestream conditions of interest. This was done by Boyce (1995) for air and nitrogen flows to give the approximation

$$P_{\text{pitot}} \approx 0.95\rho_\infty u_\infty^2 , \tag{4.9}$$

which is also used in the current work.

Figure 4.7 shows the nozzle shape used by STUBE for the current calculations. The

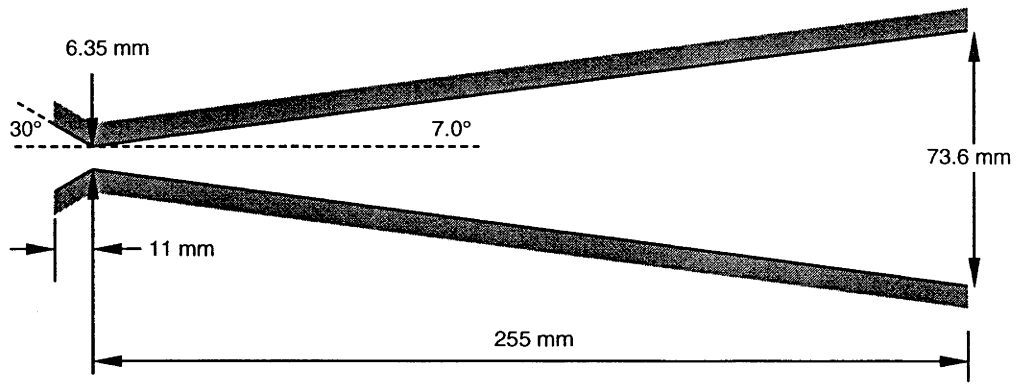

Figure 4.7: Nozzle shape and size used by STUBE code.

nozzle shape is given by

$$\frac{A}{A^\star} = B_1 + B_2 x + B_3 x^2 \,, \tag{4.10}$$

where A is the cross sectional area at distance x from the throat and $A^\star$ is the area at the throat. For a conical nozzle the coefficients are given by

$$\begin{aligned} B_1 &= 1 \\ B_2 &= \frac{2\tan\theta_{\text{eff}}}{r^\star} \\ B_3 &= \left(\frac{\tan\theta_{\text{eff}}}{r^\star}\right)^2 \,, \end{aligned} \tag{4.11}$$

where $r^\star$ is the radius at the throat. For $r^\star = 0.3175$ cm an inlet angle of 30° and outlet angle of 7.0°, the coefficients are:

$$\begin{array}{llll} \theta_{\text{eff}} = 30.0^\circ & B_1 = 1 & B_2 = -3.636852 & B_3 = 3.3066733 \\ \theta_{\text{eff}} = 7.0^\circ & B_1 = 1 & B_2 = 0.7734461 & B_3 = 0.1495547 \,. \end{array}$$

Note that STUBE takes its nozzle-input parameters in units of cm. Figure 4.8 shows plots of experimental pitot pressure versus calculated pitot pressures for each of the three operating conditions. The effective angle θ_{eff} is found to be equal to 7.0±0.2° for all three conditions and is assumed to be the same for the N_2 II condition.

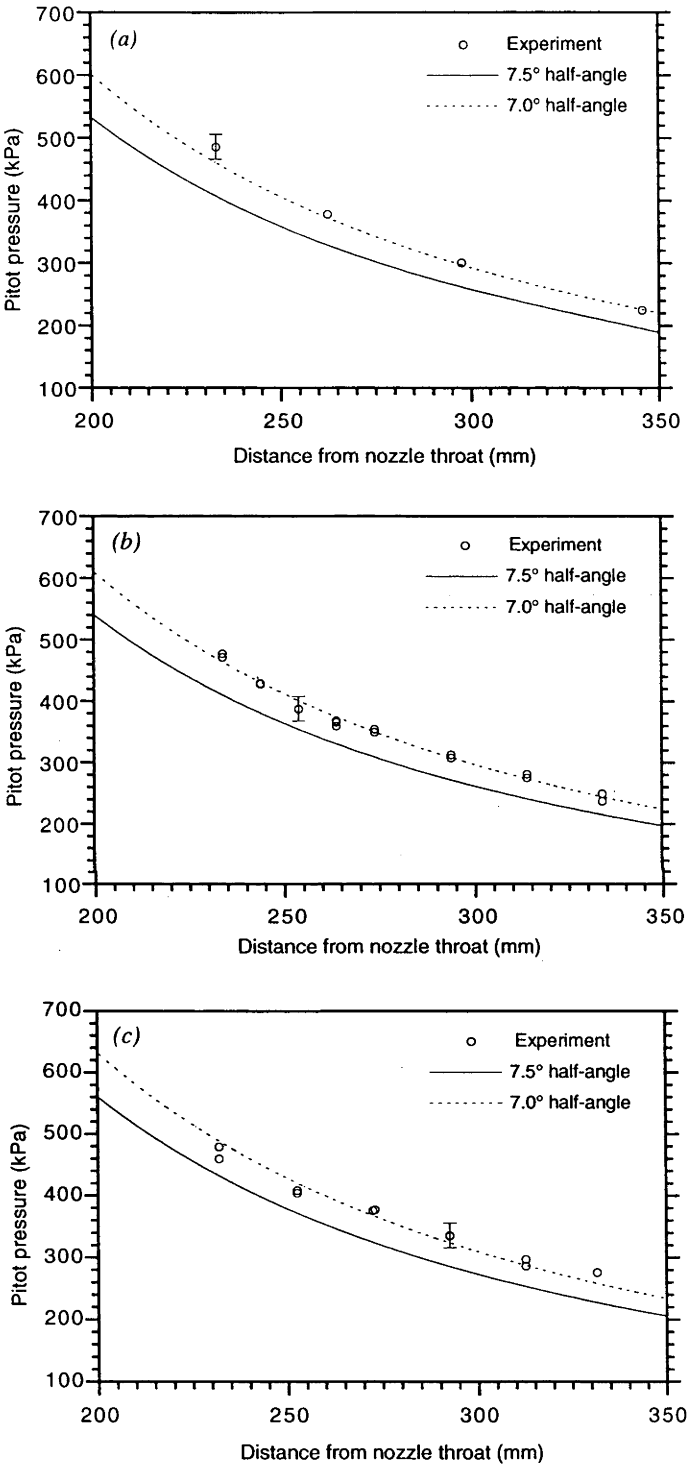

Figure 4.8: Corrections to nozzle angle due to the boundary layers on the nozzle walls : (a) N_2 I (b)Air I (c) Air II. The nozzle exit is 255 mm from the nozzle throat.

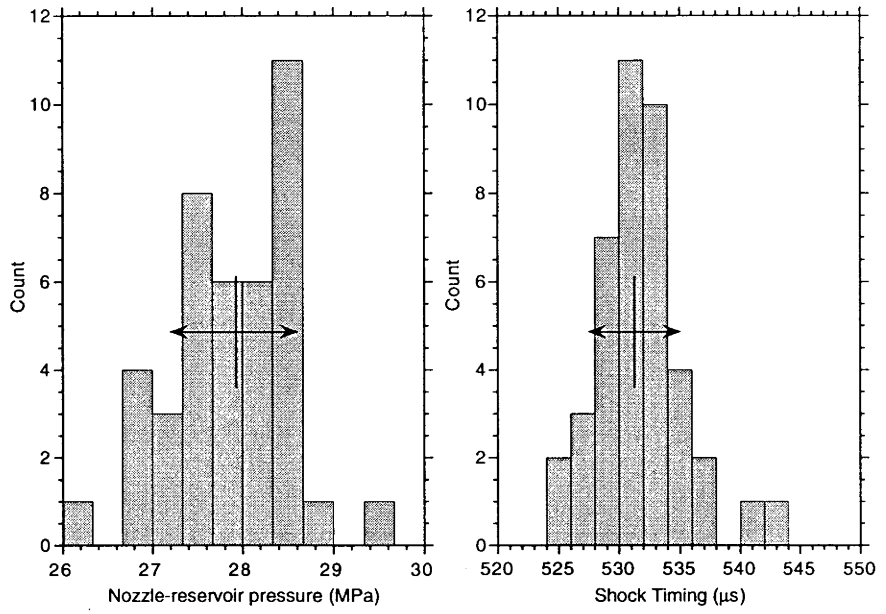

Figure 4.9: Histograms indicating the shot-to-shot variations in the nozzle-reservoir pressure and the shock timing for the Air I condition. The data is from 40 tunnel runs. The arrows indicate the standard deviation of the data.

4.6 Summary of Calculations

A summary of the nozzle reservoir and freestream conditions for each operating condition is given in Table 4.3. The uncertainties for the nozzle-reservoir conditions determined from ESTC were obtained by varying the the shock speed u_s and nozzle-reservoir pressure P_0. The uncertainties for the nozzle-exit conditions were obtained in a similar way (*i.e.*, by varying the reservoir temperature and pressure). These are *mean* operating conditions—the shock speed and nozzle-reservoir pressure have been averaged over many tunnel runs (40 for Air I; 20 for Air II). Shot-to-shot fluctuations can be caused by several factors:

- Variation in fill pressures. This is mainly due to operator error, and/or precision of the pressure gauges.
- Fluctuations in primary-diaphragm burst pressure. The diaphragms are cut from a sheet of cold-rolled steel. Each sheet is cut to produce a single batch of diaphragms. There are burst-pressure variations within a batch and also between batches. The variations in shock timing between batches can be on the order of 10 μs. Within a batch, the variations are much smaller. Only one batch of diaphragms ($\approx$ 500) was used in the current work to minimise burst-pressure fluctuations.

- Wear of piston rings. The motion of the piston changes as the piston rings wear. This is due to variations in friction between the rings and the compression tube walls, but also possibly due to driver gas leaking past the rings. The nylatron piston rings are replaced approximately every 40 shots.

Figure 4.9 shows histograms of the shot-to-shot fluctuations in the nozzle-reservoir pressure and the shock timing for 40 tunnel runs. The standard deviation of the data is used as the uncertainty in the mean.

In this chapter, we have described the design and characterisation of four new operating conditions for the shock tunnel using traditional pitot-pressure measurements. It has been observed that these pitot-pressure measurements are very insensitive to the thermochemical state of the flow and are therefore inadequate for CFD validation. This emphasises the need for rotational and vibrational temperature measurements at the nozzle exit. The nozzle-reservoir and nozzle-exit conditions have been determined with the use of the codes ESTC and STUBE. These calculated conditions will be used in the next chapter as an aid for designing a revised PLIF thermometry experiment.

Parameter	N_2 I		Air I		N_2 II		Air II	
Initial conditions:								
P_i (kPa)	100.0	0.5	100.0	0.5	40.0	0.5	40.0	0.5
T_i (K)	293	3	293	3	293	3	293	3
Timing (μs)	531.3	4	531.3	4	338.8	3.3	338.8	3.3
u_s (km/s)	2.39	0.02	2.39	0.02	3.75	0.04	3.75	0.04
$u_s^{attenuated}$ (km/s)	2.25	0.02	2.25	0.02	3.525	0.04	3.525	0.04
Nozzle-reservoir conditions (from ESTC):								
P_0 (MPa)	27.9	0.7	27.9	0.7	28.0	0.7	28.0	0.7
T_0 (K)	4219	50	3886	40	7621	60	6711	80
ρ_0 (kg/m^3)	22.3	0.5	24.7	0.6	11.6	0.3	12.5	0.3
h_0 (MJ/kg)	5.29	0.08	5.18	0.07	12.2	0.2	11.2	0.2
Nozzle-exit conditions (from STUBE):								
P_∞ (kPa)	4.40	0.2	4.7	0.2	5.9	0.2	6.46	0.2
T_∞ (K)	396	10	407	10	1108	35	1098	20
$\rho_\infty \times 10^2$ (kg/m^3)	3.74	0.08	4.0	0.2	1.76	0.05	1.94	0.06
u_∞ (km/s)	3.02	0.02	2.94	0.02	4.52	0.04	4.31	0.04
M_{frozen}	7.72	0.02	7.51	0.02	6.88	0.04	6.52	0.02
P_{pitot} (kPa)	324	10	327	10	342	10	343	10
Nozzle-exit species mole fractions:								
N_2	0.98179		0.74311		0.97413		0.70908	
O_2	0.00389		0.17110		0.00003		0.11546	
N	0.00005		0.000002		0.00408		0.000017	
O	0.00358		0.00287		0.02160		0.10374	
NO	0.01058		0.07332		0.00006		0.06260	
Ar	0.00000		0.00959		0.00010		0.00911	
Vibrational freezing temperatures:								
$T_v^{N_2}$ (K)	2150		2105		3310		3060	
$T_v^{O_2}$ (K)	1380		1320		1925		1840	
T_v^{NO} (K)	670		640		1040		995	
Miscellaneous parameters:								
θ_{eff}(°)	7.0	0.2	7.0	0.2	7.0	0.2	7.0	0.2
t_{NT} (μs)	67		67		46		46	
Laser fires (μs)	350		350		250		250	

Table 4.3: Summary of operating and flow conditions. The nozzle-exit conditions are given at 285 mm from the nozzle throat. Uncertainties are determined by varying the input parameters to the codes.

Chapter 5

Application Considerations

5.1 Introduction

In this chapter, we consider several improvements to the fluorescence imaging experiments presented in Chap. 3. First, we look at improving the rejection of flow luminosity while maintaining or increasing the fluorescence signal. Second, we characterise the various pieces of equipment used in the experiment. In particular, an excimer-pumped dye-laser system replaces the Raman-shifted tunable excimer laser previously used. The enhanced tuning range of the dye laser allows greater flexibility for selecting transitions, and enables the possibility of performing vibrational temperature measurements by pumping the (0,1) band as well as the (0,0) band. Finally, we use the calculated flow conditions from Chap. 4 to determine suitable transitions for making quantitative fluorescence measurements.

Another modification to the experiment is to use axisymmetric models as suggested in the summary of Chap. 3. This reduces the amount of flow luminosity compared with two-dimensional models (*e.g.*, cylinder) and also removes the shadowing effects discussed in Sect. 3.4. With these modifications, the goal of the revised experiments is to measure the rotational and vibrational temperatures in the freestream and on a hemisphere model for the N_2 I condition.

5.2 Spectral Filtering of Signal

The background flow luminosity is very strong and limits the application of optical techniques to the shock tunnel. For some techniques, such as schlieren photography and interferometry, a simple narrowband filter can be used to easily eliminate the

luminosity, even at the highest flow enthalpies and in the shock layer on blunt bodies where the luminosity is brightest. This is because they utilise detection of the transmitted laser beam which always has a much larger spectral intensity at the laser's wavelength than the luminosity. LIF, on the other hand, usually requires detection of a broadband signal which has a much lower spectral intensity than the original pump laser and, in some cases, the luminosity.

In general, separating the signal from the flow luminosity can be accomplished in three ways: spatially, temporally and spectrally. For techniques which have a laser-like signal beam (including coherent nonlinear techniques such as CARS and DFWM) the signal can be spatially filtered because the flow luminosity is isotropic. This is not possible for LIF because the fluorescence signal is also isotropic. Temporal filtering utilises the fact that the laser radiation is a very short pulse whereas the flow luminosity persists for the entire flow duration. The signal to background ratio can be increased by *gating* the detection system or temporally resolving the signal. In single-point LIF experiments, the signal is often detected with a fast photodetector to temporally resolve the fluorescence decay. In planar LIF measurements, gating is performed by using an image intensifier which can be switched on for periods as short as 5 to 10 ns. In luminous environments, image intensifiers are often used solely for their fast gating abilities rather than for signal amplification. Gating the signal at the point of highest fluorescence rate (*i.e.*, during the laser pulse) should maximise the signal-to-background ratio. The third method of filtering utilises the fact that the signal is much stronger than the background in certain spectral regions than in others. The signal to background ratio is increased by isolating these particular spectral regions.

5.2.1 Flow Luminosity

Figure 5.1 shows the spectral variation of flow luminosity from studies in the large free-piston shock tunnel HEG (Beck et al. 1993). The measurements were made using an intensified CCD camera at the output of a monochromator which was used to spectrally resolve the emission from a shock layer on a blunt body. The luminosity consists predominantly of a large number of discrete atomic spectral lines from metal impurities in the flow. Several studies have been performed to identify these contaminant species. Palma et al. (1993) identified species such as iron, chromium, nickel, molybdenum, copper, tin and aluminium from spectral analyses of radiation from the T3 free-piston shock tunnel. The exact origin of the contaminants is difficult to ascertain, but it is reasonable to assume that the contaminants are eroded from the shock-tube walls, entrained in the boundary layer, and then mixed with the test gas in the nozzle-reservoir region. The nozzle throat and any other parts of the facility that come into direct contact with the test gas may also contribute significantly. Beck et al. (1996) have suggested the use of a copper liner in the shock tube to reduce the contamination problem.

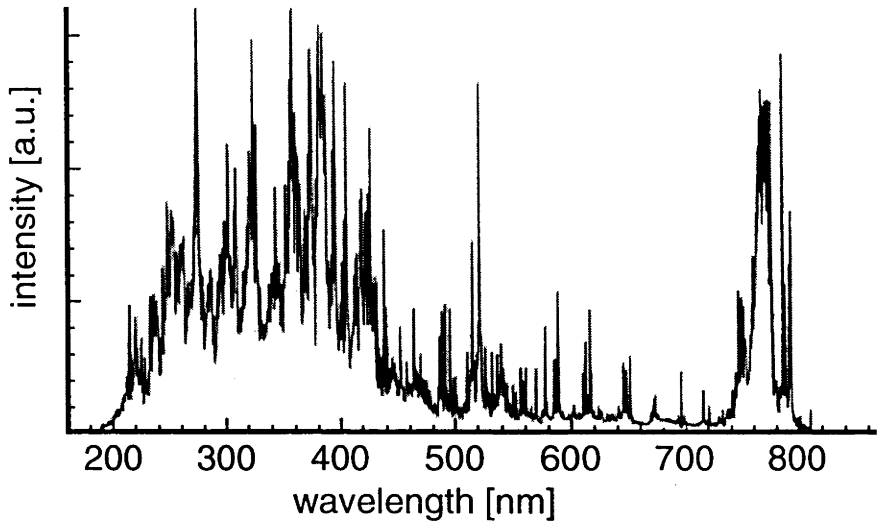

Figure 5.1: Spectral variation of flow luminosity from the HEG shock tunnel (from Beck et al. (1993)).

5.2.2 Signal-to-Background Ratio

We now derive expressions for the signal-to-background ratio to aid in quantifying the suitability of particular spectral filters for PLIF measurements. The fraction of the fluorescence signal S_{LIF} passed by a filter with spectral transmission T_{filter} and detected by a photodetector with a quantum efficiency Q_{eff} is given by

$$S = \frac{\int S_{\mathrm{LIF}} Q_{\mathrm{eff}} T_{\mathrm{filter}}\, d\lambda}{\int S_{\mathrm{LIF}} Q_{\mathrm{eff}}\, d\lambda}\,, \tag{5.1}$$

where the integrals are performed over all wavelengths. A similar fraction can be given for the fraction of background luminosity $S_{\mathrm{background}}$ passed by the filter:

$$B = \frac{\int S_{\mathrm{background}} Q_{\mathrm{eff}} T_{\mathrm{filter}}\, d\lambda}{\int S_{\mathrm{background}} Q_{\mathrm{eff}}\, d\lambda}\,. \tag{5.2}$$

The ratio S/B gives a measure of a filter's ability to reject background luminosity. However, without absolute values for S_{LIF} and $S_{\mathrm{background}}$, it can only be used to compare various filters rather than give an actual value for the signal-to-background ratio. Nevertheless, the filters used in the initial experiments in Chap. 3 serve as a reference value for determining the applicability of new filters and filter combinations. In the following analysis, the vibrational branching ratios from Piper and Cowles (1986) for NO are used to estimate the spectral variation in the LIF signal. The spectral variation of the background luminosity is approximated by taking

Filter	S	B	S/B	T^{226}_{filter}	T^{237}_{filter}	S^{226}_{LIF}	S^{237}_{LIF}
No Filter	1.00	1.00	1.00	1.000	1.000	21.01	28.01
UG5 (3 mm)	0.34	0.58	0.59	0.013	0.191	0.01	2.99
UG5.KrF	0.19	0.12	1.57	0.013	0.188	0.02	5.15
Hg 254	0.15	0.03	4.90	0.059	0.142	0.50	3.82
Narrowband	0.02	0.01	4.75	0.000	0.009	0.00	0.09
Mirror 15°	0.48	0.24	2.04	0.159	0.119	1.10	0.82
Mirror 30°	0.67	0.22	3.03	0.259	0.902	2.10	34.00
Mirror 15° ×2	*0.39*	*0.14*	*2.85*	*0.025*	*0.014*	*0.03*	*0.01*
Mirror 30° ×2	0.56	0.11	5.14	0.067	0.814	0.17	33.30
Mirror 15° ×4	0.32	0.10	3.28	0.001	0.000	0.00	0.00
Mirror 30° ×4	0.45	0.07	6.16	0.004	0.662	0.00	27.16

Table 5.1: PLIF filter analysis: S is the fraction of fluorescence transmitted by the filter; B is the fraction of background luminosity transmitted; $T^{\lambda}_{\text{filter}}$ the transmission of the filter at the wavelength λ; S^{λ}_{LIF} is the percentage of the total collected fluorescence signal that is transmitted at the wavelength λ. The emphasised filter is the one used in the current work.

values from Fig. 5.1 at 5-nm intervals.[†] Therefore, the integrals were replaced by summations at 5-nm intervals over the range 200 to 450 nm.

5.2.3 Filter Selection

The following criteria were considered when selecting a suitable filter:

- The best value of S/B to minimise competition from flow luminosity.
- A high transmission of total fluorescence signal. A compromise between good background rejection and high fluorescence throughput is necessary.
- Scatter at the laser wavelength from Mie scattering and scattering from the model should be minimised.
- The transmission of fluorescence from the (0,0) and (0,1) bands should be minimised to reduce the influence of radiative trapping.

[†]The data presented in Fig. 5.1 have been corrected neither for the spectral response of the CCD camera nor the transmission efficiency of the monochromator used. Nevertheless, they serve as a first order estimate, and since the luminosity is relatively constant between 250 and 400 nm, only a minor uncertainty is introduced.

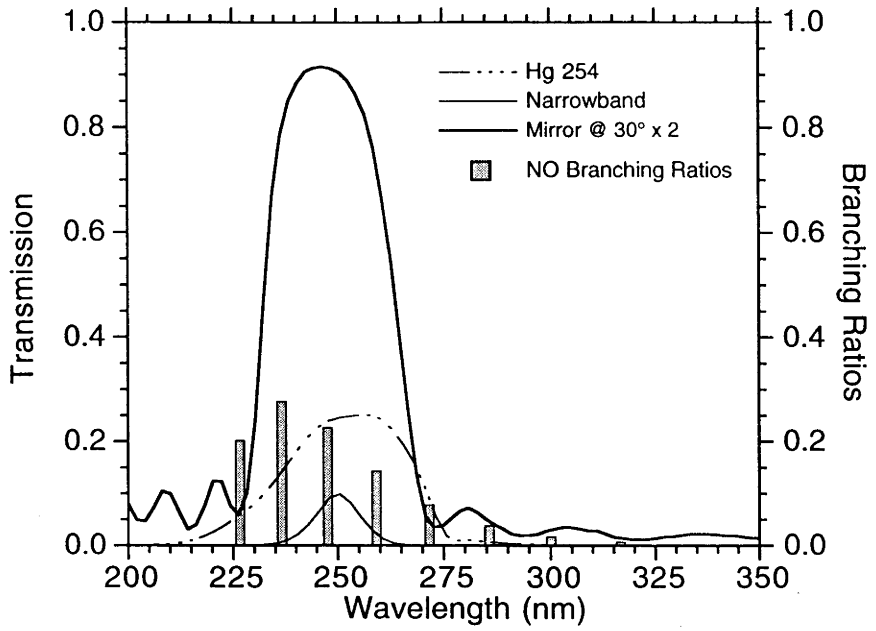

Figure 5.2: Comparison of spectral response curves between transmission filters and the custom-made reflective filter. The branching ratios for the NO bands are also shown to indicate the spectral regions where most of the fluorescence is emitted.

The last two points are addressed by having minimal transmission at 226 and 237 nm. Although pumping was performed only in the (0,0) band near 226 nm in Chap. 3, the possibility now exists that pumping of the (0,1) band near 237 nm may be used to derive vibrational temperatures. Therefore reduced transmission at 237 nm assists with reducing possible laser scatter at this wavelength.

As discussed in Chap. 3, reflective filters have the advantage of very high throughput compared with conventional interference style filters. To determine the ideal spectral characteristics (width and position) of a reflective coating for NO PLIF experiments, a test curve was designed and compared against other filter designs. When an ideal curve was achieved, the design characteristics were sent to the manufacturer. Two 76-mm-diameter mirrors were purchased with the designed reflective coating on one side only. The mirror coating that appears in the figures below was obtained from the spectral transmission curve measured on an ultraviolet spectrophotometer (Model SP800, Unicam Instruments Ltd). The transmission curve of the mirror was used to infer the reflection curve assuming negligible internal absorption losses. In the following discussion, we will refer to the reflection curve of the reflective filter as a transmission curve, since it is the reflected signal that is actually transmitted through to the detection system.

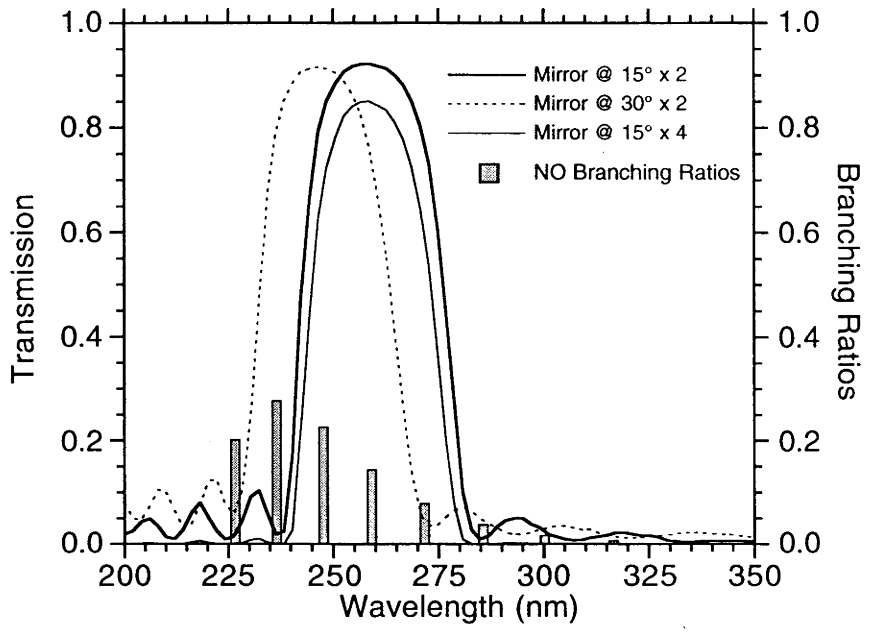

Figure 5.3: Spectral transmission curves for the custom-made mirror at different angles and with different numbers in series.

Table 5.1 compares several filters using the criteria listed above. Two commercially available interference filters are shown for comparison: a broadband filter, denoted Hg 254 (FWHM = 40 nm, centre = 254 nm) and a narrowband filter (FWHM = 12 nm, centre = 250 nm). Transmission curves for these filters and the custom-made mirror are shown in Fig. 5.2. The peak transmission is much less than for the reflective filters, however the conventional filters have much better rejection of background signal away from the centre wavelength. This is demonstrated numerically in Table 5.1 by the high S/B values and low S values. The background rejection for the reflective filters can be improved by placing several reflective filters in series. Calculations have been presented for two and four filters in series.

Another advantage of the reflective filter approach is that the transmission curve can be tuned by varying the angle of incidence. This is demonstrated in Fig. 5.3 where curves have been plotted for two different angles of incidence: 15° and 30°. The peak reflectivity shifts to lower wavelengths for higher angles of incidence. Only two filters were purchased for the current work even though a combination of four filters has better spectral characteristics. One disadvantage of using four filters in series is that the path length to the camera is increased by another 500 mm over the two-mirror case, thereby reducing the image magnification and collection angle.

The arrangement used for the remaining PLIF experiments was two mirrors in series at 15° incidence (emphasised in Table 5.1). This filter has a maximum reflectance of 0.9 at 260 nm and a FWHM of 35 nm. It passes 39% of the total fluorescence

signal compared with 19% for the UG5/KrF combination used in Chap. 3, and it rejects almost twice as much of the background luminosity. The transmission at the laser wavelengths occurs at the minima near 225 nm and 237 nm, thus reducing the influence of scattered light. The fluorescence collected from the (0,0) and (0,1) bands is 0.03% and 0.01% of the total signal, respectively, ensuring that radiative trapping is negligible. It is feasible that one may tune the filters to minimum throughput of scattered laser radiation by varying the angle of incidence, such that one of the minima coincides with the laser wavelength. Note that greater than 80% of the $v'' = 2, 3, 4$ bands are transmitted, while the $v'' = 0, 1, 5$ bands align with minima.

If pumping of only the (0,0) band near 226 nm is to be performed, then changing the angle of incidence of the mirrors to 30° will enhance the fluorescence signal by 17%. This gain in signal comes about because 80% of the (0,1) band is now collected. However, one should confirm if radiative trapping by reabsorption from the $v'' = 1$ state is appreciable. This may be the case if considerable population resides in the $v'' = 1$ state, which may occur for vibrationally-frozen flows. Note also that the S/B value is more than three times that of the UG5/KrF combination.

A comprehensive analysis of reflective filter design has been performed by Battles (1994) with the intention of minimising background fluorescence from O_2 in NO PLIF experiments. Interference from O_2 may occur at high temperature and pressures when exciting NO at 225 nm. Andresen et al. (1990) has used reflective filters for NO PLIF experiments performed with an ArF excimer laser at 193 nm. In NO PLIF experiments carried out on the large free-piston shock tunnel HEG, Beck et al. (1996) used four reflective filters in series to filter the fluorescence signal from flow luminosity. The current analysis was limited to a filter with bandwidth of approximately 40 nm. Bandwidths as low as 10–15 nm are possible, but at greater expense. An extension to the current work would be to determine if using a very narrow bandwidth filter to isolate a single fluorescence band, say the (0,1) band, would significantly improve the background rejection.

5.3 Equipment Characterisation

5.3.1 Laser Linewidth

When choosing transitions to excite in LIF experiments, it is necessary to determine if overlaps with nearby transitions are important. Thus a knowledge of the laser spectral linewidth is required. The laser linewidth is also important for modelling the LIF process, or calculating computational flow images (CFI) from CFD results. To determine the laser linewidth from a single laser pulse, an etalon can be used and an image of the fringes recorded on a CCD or linear array. However, for the current

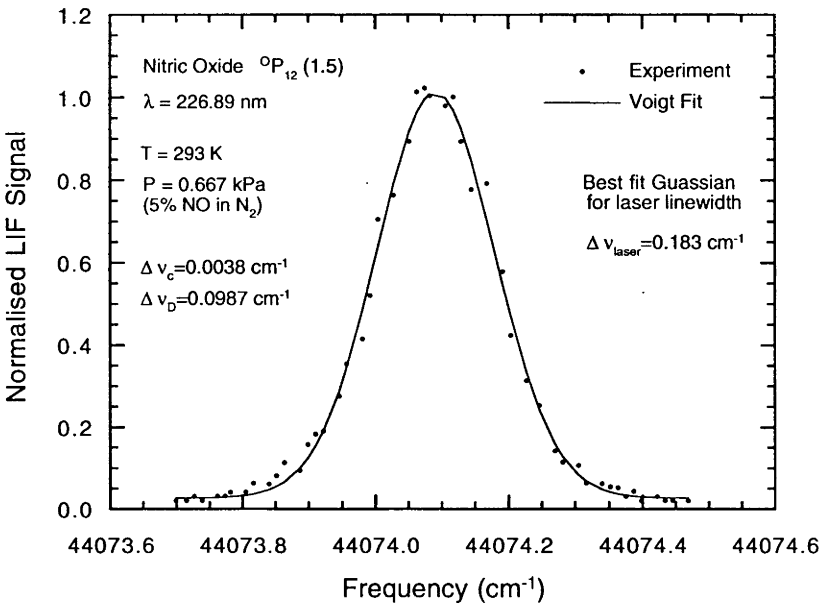

Figure 5.4: LIF excitation scan across an isolated NO transition used to determine the linewidth of the laser.

work no etalon with the correct characteristics (*i.e.*, UV transmission, high finesse) was available. An alternative method that delivers the pulse-averaged linewidth is to perform a LIF excitation scan over a single isolated transition and deconvolve the laser linewidth. This approach works well when the absorption linewidth is much less than the laser linewidth. This method was used here.

A cell at room temperature (293 K) was filled with 0.667 kPa (5 torr) of 5% NO in N_2. The collision- and Doppler-broadening widths at these conditions are 0.0038 cm^{-1} and 0.0987 cm^{-1}, respectively. The low pressure ensures a small contribution from collision broadening to the overall transition linewidth. This is desirable because accurate calculation of the collision width relies on accurate knowledge of the pressure and mixture composition, and also the collision-broadening coefficients for each collision partner. The Doppler width, on the other hand, relies only on knowledge of the temperature and molecular weight of NO, both of which are very well known. Hence a scan across a Doppler broadened line should allow easy determination of the laser linewidth.

The laser was tuned to the isolated NO transition $^{O}P_{12}(1.5)$ at 44074.15 cm^{-1}. The LIF was measured at right angles to the beam with a photomultiplier (Hamamatsu R466) and a 3-mm-thick UG5 filter to block scattered light at the laser wavelength. A UV photodiode (UDT Sensors P/N UV005) was used to monitor the laser energy before the test cell. At the low pressures used in this experiment, saturation of the molecular transition becomes appreciable and so reduction of the laser intensity

is necessary. The laser energy was varied to produce a plot of LIF signal versus incident laser energy. Neutral density filters were then placed in the beam to reduce the energy until the plot of LIF signal versus laser energy produced a linear response. When a linear response was established, an excitation scan across the transition was performed. Figure 5.4 shows the experimental data obtained from the scan and a best-fit Voigt profile achieved with a Gaussian laser profile of 0.18 ± 0.01 cm^{-1}.

5.3.2 Intensified CCD Camera Linearity

The same intensified CCD camera as described in Sect. 3.2.2 was used for the dye-laser experiments. In the previous experiment, the linearity of the detector was verified by imaging NO LIF in the shock tunnel dump tank at a gain of 7.8. This analysis is repeated here in more detail. Calibrated UV neutral density filters were used to vary the laser sheet energy. Fifty images were taken at each energy and the central 100 × 100 pixels of the image were averaged. The thermal background noise of the camera was also measured for each energy measurement by covering the lens and again acquiring fifty 'dark' images. The averaged laser energy was simultaneously measured for the same fifty pulses with a calibrated UV photodiode. Each measurement was corrected for background and laser-energy fluctuations and the mean signal of the 100 × 100-pixel area plotted. The results at four different gains appear in Fig. 5.5. The curve for gain 6.6 indicates that the fluorescence was linear with laser intensity up to 1.0 mJ.

Several problems exist with this method of testing the ICCD linearity. It was not possible to test the linearity over the full dynamic range of the camera due to shot noise. The standard deviation in the mean for a single image varied with gain: from 7% of the mean signal at a gain of 6.5 to 30% at a gain of 7.5. Therefore, the maximum mean signal that could be measured without a significant number of pixels saturating (*i.e.*, exceeding 255 counts) due to shot noise was limited to about 100 counts, as indicated in the figure. The offset, or background level, for the CCD camera was 15 counts, thus making the maximum possible signal for a single pixel 240 counts. For a gain of 7.5, the highest point on the corresponding curve in Fig. 5.5 occurs at an average value of 100 counts per pixel. Another contributing factor to this low value may be due to a non-uniform signal across the 100 × 100-pixel region of interest. At a gain of 6.6 the shot noise was less of a problem, but the laser energy could only be increased to 1.0 mJ. The result of this was that the ICCD was only tested up to 50 counts. Higher laser energies are necessary to test the camera at this gain setting, however given that the camera was linear up to 100 counts at the higher gains it is safe to assume that it also linear at this lower gain.

The intensifier linearity can also depend on the temporal width of the signal. The conditions used in this test would result in a relatively long fluorescence lifetime whereas measurements at higher pressures or in the presence of other quenching

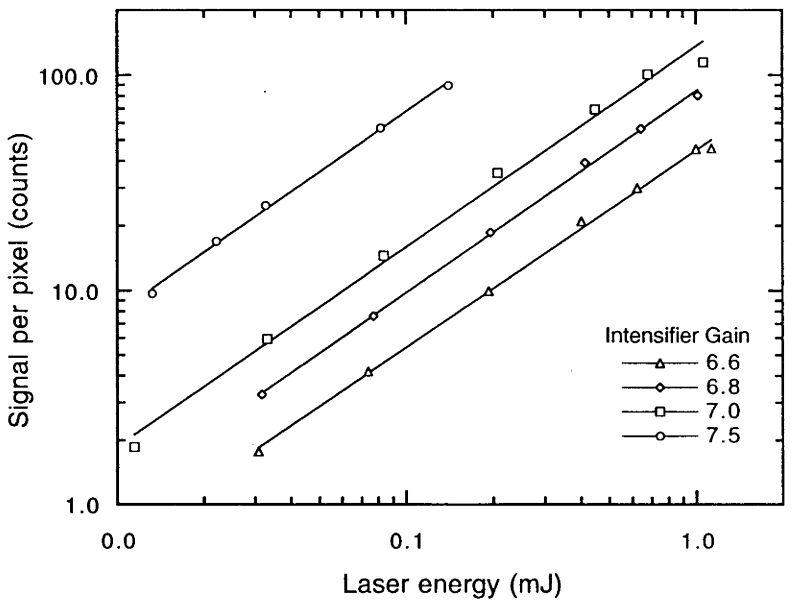

Figure 5.5: The linearity of camera response is verified for four different intensifier gains.

species would have much shorter lifetimes and therefore different saturation levels.

The data demonstrate the camera response is linear up to at least 100 counts above the background level. More work is required to test the camera thoroughly across a wider range of conditions. In particular, shorter fluorescence lifetimes should be used. However, the maximum average signal obtainable will always be limited by shot noise. In the experiments that follow, the peak measured signals were kept to about this 100-count limit.

As mentioned previously, the detector has a limited dynamic range. Some added flexibility can be obtained by being able to vary the gain control of the camera. This allows higher gains to be used with weak transitions to fill the dynamic range more appropriately, and lower gains for stronger transitions. A similar process to that described above was used to measure the fluorescence signal as a function of gain. An exponential fit to the data produces the following relation:

$$\text{Signal per pixel} = 1.51 \times 10^{-8} \exp(3.35G) \ , \tag{5.3}$$

where G is the dial reading on the 10-turn potentiometer used to vary the intensifier gain. G varies between 6.5 and 7.5 in the current work. This relation may be used to scale LIF images obtained at different gains.

5.3.3 Laser Energy Monitoring System

The same laser-sheet monitoring system as described in Sect. 3.2.2 was used for the dye-laser experiments. Total laser beam energies were also measured with the photodiode. Ideally, one could use the sheet-profiling system to account for both spatial variation of sheet energy and also fluctuations in the total beam energy. This would be an improvement because only about 50% of the total beam energy appears in the useful part of the laser sheet, so fluctuations of the spatial distribution of laser energy within the beam could introduce uncertainties. In order to do this, the system must be calibrated at each wavelength because the spectral response of the system (*i.e.*, dye, CCD) varies significantly between 225 and 245 nm. Also, it should be calibrated for various settings of the camera aperture, which is used to adjust the fluorescence signal so that it fills the dynamic range of the CCD. A calibration measurement *was* made at each wavelength, unfortunately however, it was discovered later that the calibration had changed over successive tunnel runs. The reason for this was that a homemade beam attenuating device used to control the laser intensity at the laser exit had the unfortunate side effect of also varying the beam polarisation, which in turn affected the splitting efficiency of the sheet beamsplitter, and thus the calibration. Therefore, the spatial profile of the laser sheet is used to correct spatial variations in the laser energy, while the photodiode signal is used to correct for fluctuations in the total beam energy. This method assumes that the fraction of energy going into the centre part of the laser sheet is constant, which is a good assumption if the sheet cross section remains relatively constant. A comparison of the sheet cross sections for several laser pulses showed this indeed to be the case.

The spectral response of the UV-enhanced photodiode between 200 and 300 nm is shown in Fig. 5.6. It is very important to take the spectral variation of the photodiode response into account when performing quantitative measurements. The uncertainty in the measurement of the laser energy directly affects the LIF signal uncertainty, and, therefore, the accuracy of the temperature measurements. Also shown on the plot are the positions of the transitions used in the experiment for the three vibrational bands. The photodiode was calibrated against a joulemeter at 225 nm so that the amount of energy in a 1-cm-wide section of the laser sheet could be estimated from the photodiode signal. The calibration constant at 225 nm was measured to be 14.8 mJ/V. This value varies if the sheet-forming optics change, which was the case for the shock-layer measurements where a higher energy density was required. A 40-mm-focal-length cylindrical lens replaced the 20-mm-focal-length lens to make a narrower sheet. In this case, the calibration constant should be divided by 3.1.

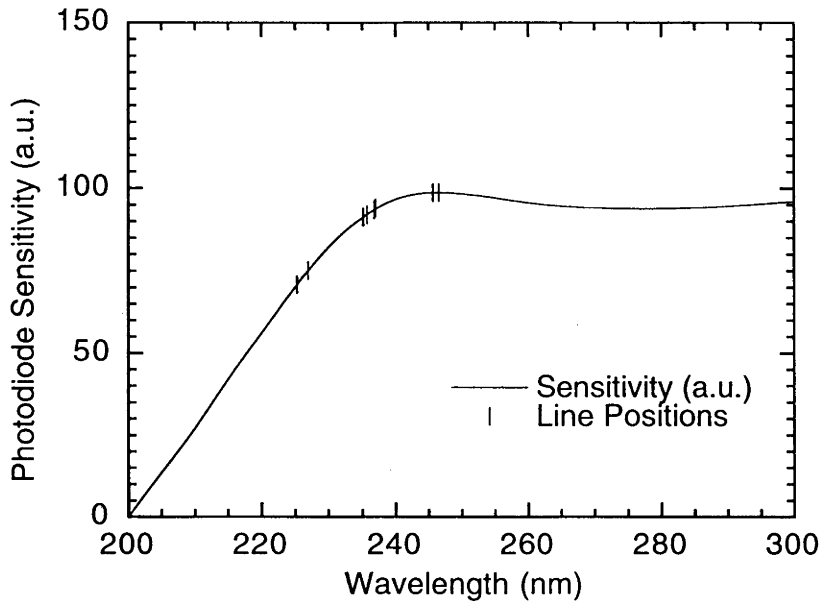

Figure 5.6: The spectral response of the UV enhanced silicon photodiode used to measure the total beam energy. The curve is taken from the manufacturer's specifications.

5.3.4 Sheet Thickness

The laser sheet thickness (*i.e.*, the smallest sheet dimension) was measured by traversing a knife edge through the beam in the test section while measuring the transmitted energy with a photodiode. The waist of the beam is intentionally placed some distance before the test section so that the beam has slightly diverged when it reaches the test section. This reduces the beam irradiance and therefore the likelihood of saturation of the LIF excitation transition. Assuming the profile is Gaussian, the half-width of the sheet is defined as the distance for the intensity to drop to $1/e^2$ of the sheet-centre value. The sheet thickness is twice this value, and the value obtained from this method is 0.8 ± 0.1 mm. This measurement can be used for estimating the irradiance of the sheet and hence the degree of saturation for excitation transitions.

5.4 Transition Selection

The theory of two-line thermometry has been described in Sect. 2.7.1. Equation 2.71 suggests a large ΔE value for optimum temperature sensitivity (*i.e.*, a large energy separation between the absorbing states for the two transitions). However, for very

large differences in the absorbing state energies, the signal can vary significantly and exceed the dynamic range of the camera. Here that restriction is relaxed because of the calibration of the intensifier gain control described in the previous section.

The important criteria that need to be considered when choosing transitions are:

1. *A large value of* ΔE. This improves the temperature sensitivity as defined by Eq. 2.71. Importantly, it reduces the influence of other error sources (*e.g.*, beam attenuation, saturation, interferences, laser mode fluctuations). When choosing transitions for rotational temperature measurements, it is necessary to keep the vibrational energy G_v constant (*i.e.*, same vibrational band) to remove vibrational temperature dependence and to also have a large difference in the rotational energy F_J. Alternatively, for vibrational thermometry, a large variation in G_v is desirable while it is ideal to keep F_J constant to remove any rotational temperature dependence.

2. *Isolated transitions.* When a transition i is excited by a laser pulse, the fractional contribution to the total LIF signal caused by the laser profile overlapping nearby transitions is given by

$$\xi_{\text{Inter}} = 1 - \frac{S_i}{\sum_j S_j} , \tag{5.4}$$

where S_i is the signal from the transition i alone, and the sum is over all transitions j that the laser profile overlaps. This is a measure of the transition's isolation from other transitions. Transition pairs are treated as single isolated transitions for this calculation.

3. *Laser-beam attenuation.* In situations where the beam attenuation is appreciable, significant systematic errors may occur in the temperature measurement. The influence of beam attenuation can be negated if both transitions produce the same fractional drop in signal. However, the absorption coefficient depends on the temperature, pressure, and species number density, so a rough knowledge of the environment before the measurement is necessary in order to use this approach. Recall from the definition of absorption coefficient (Sect. 2.3.2) that the irradiance at frequency ν after traversing a distance ℓ [cm], assuming uniform flow (*i.e.*, $Y(\nu)$ is constant), is given by

$$I_\nu(\ell) = I_\nu(0)\exp[-k_\nu \ell] = I_\nu(0)\exp[-S_{12}Y(\nu)\ell] , \tag{5.5}$$

and therefore the fractional drop (absorbance) in the spectrally integrated irradiance at distance ℓ is

$$\xi_{\text{BA}} = 1 - \frac{\int I_\nu(\ell)d\nu}{\int I_\nu(0)d\nu}$$

$$
\begin{aligned}
&= 1 - \frac{\int I_\nu(0) \exp[-S_{12}Y(\nu)\ell] d\nu}{I_{\text{total}}(0)} \\
&= 1 - \frac{I_{\text{total}}(0) \int L_\nu(0) \exp[-S_{12}Y(\nu)\ell] d\nu}{I_{\text{total}}(0)} \\
&= 1 - \int L_\nu(0) \exp[-S_{12}Y(\nu)\ell] d\nu \qquad (5.6)
\end{aligned}
$$

where $I_\nu(x) = I_{\text{total}}(x) L_\nu(x)$ has been used.

4. *Partial transition saturation.* This can lead to discrepancy in the temperature measurements if it is not accounted for. Measurements of absolute saturation intensities are notoriously difficult, primarily because of the difficulty associated with measuring the beam area. Nevertheless, if it is necessary to work in the partially saturating regime to increase signal strengths, the effects can be negated by choosing lines with similar $B_{J'J''}$ coefficients so that the degree of saturation will be the same for both transitions. Alternatively, this restriction can be relaxed and different $B_{J'J''}$ coefficients chosen, if the laser energy is varied to maintain the same level of saturation for both transitions. The validity of the assumption that saturation effects cancel in the signal ratio depends on many factors. If the saturated signal can be written as the product of the linear signal and a saturation correction factor, where the functional dependence of the correction term is not necessarily known but is the same for both transitions, then the correction factor will cancel in the signal ratio. This should be a reasonable assumption for low levels of saturation (*i.e.*, $< 10\%$). Transition pairs would tend to have different saturation characteristics from isolated single transitions. The saturation correction term would also tend to vary between different transition pairs as the ratio of the two $B_{J'J''}$ coefficients varied. For example, a transition pair consisting of a strong and a weak transition would tend to saturate in a different manner to one composed of transitions of equal strengths. For this reason, transition pairs are avoided in the current work. Note that the Einstein Coefficients $B_{J'J''}$ should be used, and not the Hönl-London factors $S_{J'J''}$ which omit the vibrationally-dependent part of the line strength.

5. *Minimum signal.* Although the effective dynamic range of the camera has been increased by calibration of the gain control, there is still a minimum detectivity for the camera. This is determined by the maximum linear camera gain, the background noise and flow-luminosity levels.

There are some 650 useful lines in the (0,0) band of NO. The (1,1) band starts at 224.5 nm and this determines the lower limit of useful transitions in the (0,0) band. To sift through these spectral lines for the optimum transitions for thermometry, a FORTRAN computer program was written. This line-selection program is called LINUS and was run on a Macintosh PowerPC. Selection criteria are entered and the lines that are not rejected by the program are displayed at the end of the

calculation. This allows the user to fine-tune the selection criteria to produce a short list of candidate transitions from which the final choice can be made. The spectroscopy of NO and the calculation of line positions and strengths is described in Appendix A. Below, we treat the selection of transitions for the cases of freestream and shock layer separately because of their particular unique issues.

In the experiment, tuning of the laser to the chosen transition is accomplished by monitoring LIF in a flame. The collision-induced frequency shift in the flame and in flow are different, and so a detuning between the laser and transitions in the flow is included in the calculations. The laser was tuned 0.02 cm^{-1} below the absorption transitions in the freestream and 0.09 cm^{-1} above the transitions in the shock layer.

5.4.1 Freestream Transition Selection

The freestream conditions are taken from Table 4.3 for the N_2 I condition. The absorption lines are not broadened significantly due to the low temperature and pressure and a large number are relatively well isolated (160 lines have <1% interference). The lines are predominantly Doppler broadened with a Gaussian FWHM of 0.11 cm^{-1}, compared with the laser Gaussian FWHM of 0.18 cm^{-1}. The fluorescence lifetime is 114 ns due to the low quenching rate. The conditions are summarised in Table 5.2 for both the freestream and shock layer.

Table 5.3 shows the chosen transitions. All of the transitions have very low beam attenuation and are well isolated. Hence, these effects are not expected to contribute significantly to temperature uncertainties. The influence of saturation is minimised by choosing lines in weak branches and choosing single transitions. The laser energy can be varied to achieve the same level of saturation on each transition. Transitions were chosen in different vibrational bands with similar values of F_J so that they could be used for vibrational temperature measurements. A vibrational temperature can be obtained by using lines 1 and 3, 2 and 4, or by using lines 1 and 5. The corresponding values of $\Delta E/kT_{\text{vib}}$ are 4.0, 4.0, and 8.0, respectively, assuming that T_{vib}=670 K. This implies that the temperature measurement will be very insensitive to errors in the LIF signal ratio, even if T_{vib} is as high as 1500 K. For rotational temperatures, lines 1 and 2, and lines 3 and 4, can be used to make independent measurements. The $\Delta E/kT_{\text{rot}}$ value for a rotational temperature of 396 K is 3.5, which also provides excellent temperature sensitivity.

5.4.2 Shock-Layer Transition Selection

The conditions immediately behind the normal part of the shock on the hemisphere are calculated using the NSHOCK routine contained within STUBE. However, to

Parameter	Freestream	Hemisphere Shock Layer
Temperature (K)	396	4146
Pressure (kPa)	4.4	295
$\Delta\nu_D$ (cm^{-1})	0.11	0.37
$\Delta\nu_c$ (cm^{-1})	0.02	0.23
$\Delta\nu_s$ (cm^{-1})	-0.006	-0.11
Γ	0.71	0.26
Q (s^{-1})	3.8×10^6	2.7×10^8
R (s^{-1})	4.0×10^8	8.3×10^9
Lifetime (ns)	114.1	3.6
I_{sat}-Analytic (kW/cm^2)	24–580	800–40,000
I_{sat}-Numerical (kW/cm^2)	289±4	15,646±230
I_{sat}-Experiment (kW/cm^2)	160±22	13,400±180

Table 5.2: Shown are the calculated conditions for the two environments on which thermometry is performed. The freestream conditions are at 285 mm from the nozzle throat. The hemisphere shock-layer conditions are determined using STUBE. $\Delta\nu_D$ is the Doppler width, $\Delta\nu_c$ is the collision width, $\Delta\nu_s$ is the collision shift, and Γ is the dimensionless overlap integral. The quenching, Q, and rotational energy transfer, R, rate constants are determined from the equations presented in Sect. 2.4. The three saturation irradiances are determined as follows: Analytic—using Eq. 2.59 and assuming zero and fully-relaxed rotational redistribution, respectively; Numerical—obtained from the five-level numerical model developed in Sect. 2.6.2 using a XeCl-excimer-laser pulse shape ($\approx$ 25 ns); Experiment—using the experimental reference value and scaling to the required conditions using Eq. 2.54. The freestream and shock-layer I_{sat} calculations are for the ${}^OP_{12}(2.5)$ and $P_1(35.5)$ transitions, respectively. See Sect. 5.4.3 for a discussion of saturation irradiances.

account for the energy frozen in the vibrational modes in the freestream, a nozzle-flow calculation was performed using STUBE, assuming vibrational equilibrium. The conditions thus obtained (T_∞=508 K, P_∞=5.5 kPa, u_∞=3.06 km/s) are used as input to STUBE to determine the post-shock conditions. This approach ensures that the correct amount of energy is included in the calculation, since STUBE doesn't account for energy initially locked in the vibrational modes when performing the normal shock calculation. The conditions are shown in Table 5.2. As a check, a similar calculation was performed with ESTC, producing identical results. The flow behind the shock is in vibrational equilibrium as verified by calculations of the vibrational and flow length scales by STUBE.

As indicated in Table 5.2, the lines are significantly broader than the laser profile. This causes more interference from nearby transitions (only 29 lines have <1% interference) and also higher beam attenuations. The high quenching rate produces a

	v''	Transition Branch	J''	Frequency (cm^{-1})	F_J (cm^{-1})	G_v (cm^{-1})	$B_{J'J''}$ (cm/J)	ξ_{Inter} (%)	ξ_{BA} (%/cm)
Freestream									
1.	0	$^{O}P_{12}$	2.5	44069.416	73.58	948.66	146.99	0.03	0.496
2.	0	R_2	23.5	44382.109	1045.85	948.66	144.88	0.27	0.115
3.	1	R_2	2.5	42229.348	73.41	2824.76	96.86	0.23	0.006
4.	1	R_2	23.5	42516.527	1035.33	2824.76	225.70	0.00	0.003
5.	2	$^{S}R_{21}$	8.5	40562.179	71.37	4672.68	116.47	0.22	0.0004
Hemisphere Shock Layer									
6.	0	P_1	35.5	44393.186	2101.89	948.66	166.45	1.83	0.43
7.	1	P_1	35.5	42540.026	2078.94	2824.76	259.29	2.09	0.35
8.	2	P_1	35.5	40714.251	2056.80	4672.68	241.72	1.41	0.17

Table 5.3: Transitions selected for thermometry in the freestream and hemisphere shock layer. F_J is the rotational energy; G_v is the vibrational energy; $B_{J'J''}$ is the Einstein absorption coefficient in units of $s^{-1}(W/cm^2/cm^{-1})^{-1}$; ξ_{Inter} indicates the isolation of the transition; and ξ_{BA} is the percentage beam attenuation per cm path length. The spectroscopic values were calculated using the equations in Appendix A.

very short fluorescence lifetime, thereby significantly reducing the signal. However, the saturation irradiance is also increased, so higher laser energies can be used to counter the effects of quenching. The three transitions listed in Table 5.3 can only be used to give a vibrational temperature. However, since vibration is in equilibrium behind the shock, this also gives the rotational temperature. Nevertheless, a measurement of the rotational temperature would have been desirable to confirm vibrational equilibrium. It was found during the experiment that the freestream signal produced by exciting low-J lines was far greater than the shock-layer signals. The high freestream signals caused saturation of the camera and also an anomalous effect on the shock-layer signals.[†] This effect was avoided by exciting high-J lines which had very little or no freestream signal. The $\Delta E/kT_{\text{vib}}$ value is 1.3, assuming that T_{vib}=4146 K.

[†]Possible causes of the irregular shock-layer signals include: scattering of freestream signal from parts of the shock tube into the camera, especially the closed port opposite the observation window; ghost images from the reflective filters (the backs of the mirrors were uncoated, but perhaps should be anti-reflection coated in the future); intensifier microchannels in the freestream saturating and bleeding into nearby channels.

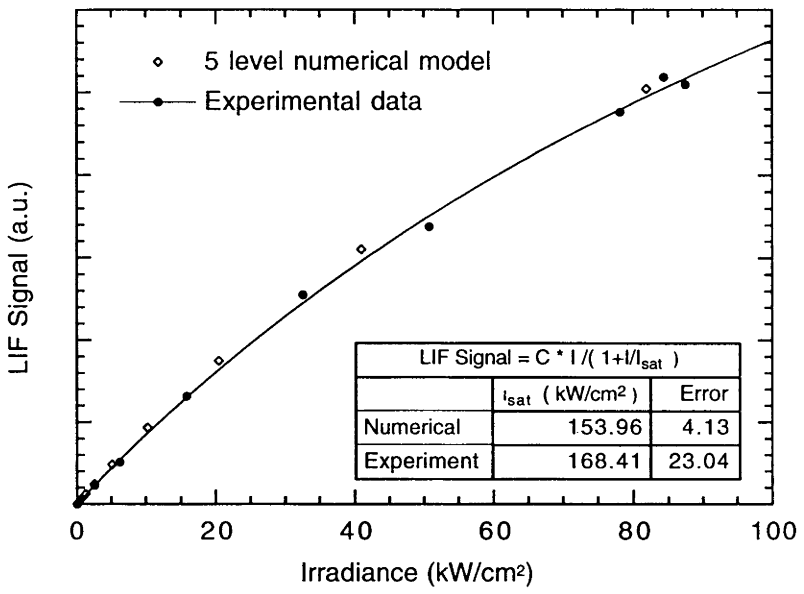

Figure 5.7: Saturation irradiance measurement for the $R_2(20.5)$ transition of the (0,0) band at a pressure of 1.33 kPa and a temperature of 300 K. The saturation irradiance is determined by fitting the function $I/(1 + I/I_{\text{sat}})$ to the data.

5.4.3 Saturation Irradiances

A saturation measurement was performed with a mixture of NO in N_2 in the shock-tunnel dump tank using the PLIF experimental setup to achieve the same temporal, spatial and spectral laser characteristics as for the experiment. The results are shown in Fig. 5.7. Each experimental data point is obtained by averaging a 100×100 pixel region in the centre of the LIF image, and averaging over 50 laser pulses to reduce the influence of laser-mode fluctuations. The laser energy was varied with calibrated UV neutral-density filters. Corrections were made for the total laser-energy fluctuations and background noise on the camera. The saturation irradiance is determined by fitting the function $I/(1 + I/I_{\text{sat}})$ to the data.

A saturation irradiance of 168±23 kW/cm^2 was measured for the $R_2(20.5)$ transition of the (0,0) band at a pressure of 1.33 kPa and a temperature of 300 K. This compares very well with the saturation irradiance of 154±4 kW/cm^2 obtained from the five-level numerical model developed in Sect. 2.6.2 using a XeCl-excimer-laser pulse shape ($\approx$ 25 ns). The uncertainties were obtained from the curve fits to the experimental and numerical data, and hence the numerical value does not reflect the large uncertainty in quenching and RET rates due to lack of cross-section data. The analytic values calculated from Eq. 2.59 are 3.3 and 560 kW/cm^2, obtained by assuming zero and fully-relaxed rotational redistribution, respectively.

The experimentally-determined saturation irradiance was used to calculate the saturation irradiances for other transitions at the freestream and shock-layer conditions, using Eq. 2.54. Table 5.2 shows the freestream and shock-layer I_{sat} values calculated for the ${}^{O}P_{12}(2.5)$ and $P_1(35.5)$ transitions, respectively. These saturation irradiances correspond to about 320 μJ and 32 mJ for each centimetre of a 0.8 mm thick sheet. Typical sheet energies for the experiment were 7 and 850 μJ per cm for the freestream and shock-layer experiments, respectively, which produce I/I_{sat} values of 2.2% and 2.7%.

Chapter 6

Laser-Induced Fluorescence Imaging : Dye-Laser Results

6.1 Introduction

In the previous chapter, modifications to the PLIF experiments of Chap. 3 were detailed. In particular, the spectral filtering of the signal was redesigned, careful analysis of the transition selection process was performed, and characterisation of the experimental apparatus presented. This chapter describes the experiments and the results obtained using the dye-laser system. Temperature measurements are performed in the freestream at the nozzle exit of the shock tunnel and also in the shock layer on a hemisphere.

6.2 Experiment

6.2.1 Apparatus

The experimental arrangement is shown in Fig. 6.1. The laser source is a frequency-doubled excimer-pumped dye laser producing approximately 6 mJ of radiation at 225 nm. The excimer laser is the same dual-chamber model used in the previous Raman-shifting experiments. The output of the amplifier chamber, operating as an unstable resonator, is used to pump the dye laser with approximately 250 mJ of 308-nm broadband radiation. The dye laser (Lambda Physik, Scanmate II) is operated with different Coumarin laser dyes (Lambdachrome LC4500, 4700, 4800) to produce 40 mJ of tunable, narrowband radiation between 450 and 490 nm. This

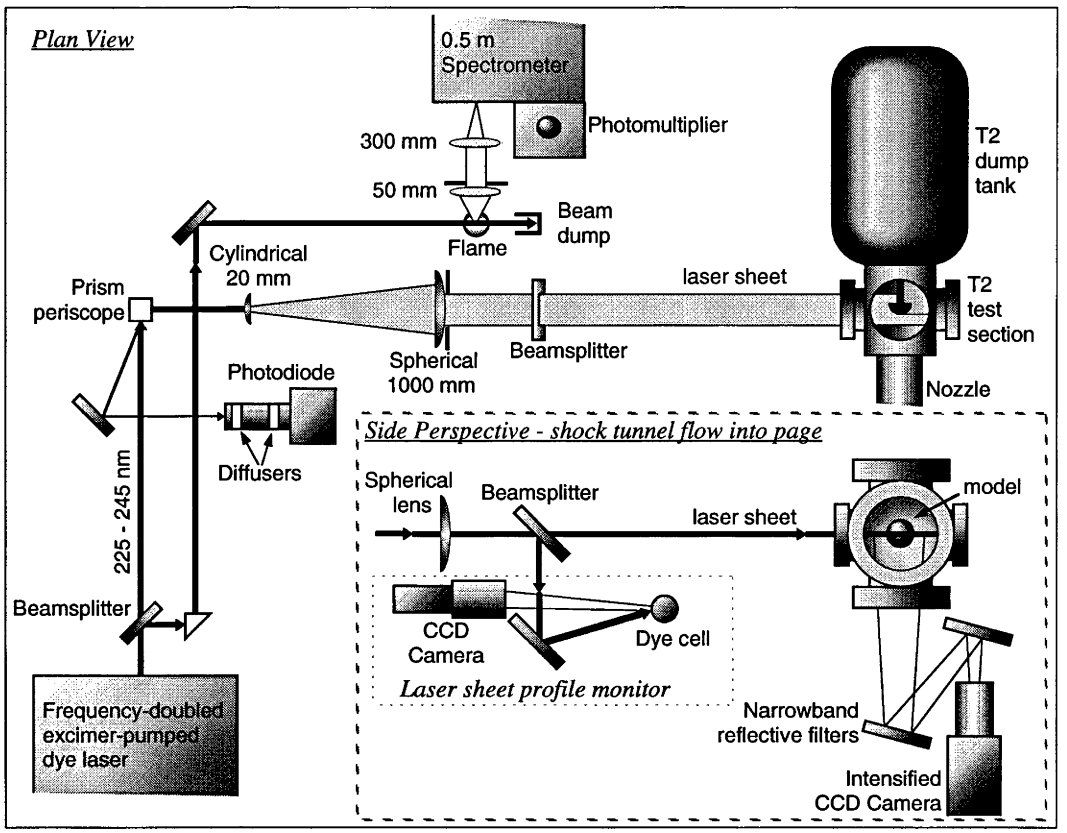

Figure 6.1: Experimental apparatus for LIF imaging experiments.

blue light is then frequency doubled with a BBO I crystal to produce about 6 mJ of UV radiation. Software was written for controlling the dye-laser tuning and excimer-laser triggering from a separate computer. The computer was also used to acquire data from LIF excitation scans.

Approximately 10% of the laser radiation was split off with a beamsplitter (uncoated fused silica) and directed through a small turbulent flame to perform LIF excitation scans. Flow meters were used to measure and maintain a constant flow rate of H_2 and O_2 to the flame in a ratio of approximately 6 to 1. A fuel-rich mixture was chosen to maximise the NO LIF signal. The NO is produced by entrainment of the air in the flame. The LIF is collected at right angles to the beam with a 25-mm-diameter, 50-mm-focal-length lens. The fluorescence is collimated and then imaged onto a 0.5-m spectrometer with a 300-mm-focal-length lens. The spectrometer was operated as a 9-nm bandpass filter which allows detection of LIF from the NO (0,1) or (0,2) vibrational bands. The filtered fluorescence is detected with a photomultiplier (Hamamatsu R446) and the output signal is conditioned and digitised with a homemade gated integrator.

The remaining laser radiation passes through a periscope to bring the beam to the same level as the shock-tunnel test section. The sheet-forming optics consist of a cylindrical lens and a large spherical lens (1000-mm focal length, 100-mm diameter). A 20-mm-focal-length cylindrical lens was used for the freestream measurements to produce a 80-mm wide sheet, while for the hemisphere shock-layer measurements a 40-mm-focal-length cylindrical lens was used to produce a narrow, high intensity, 20-mm-wide sheet. The sheet energy distribution was monitored with a dye cell and CCD camera as described in Sect. 3.2.2. The laser sheet was focussed before the test section so that the sheet thickness at the test section was 0.8 mm (see Sect. 5.3.4). The total beam energy was monitored with a back reflection from a prism using a UV-sensitive photodiode. The spectral calibration of the photodiode is detailed in Sect. 5.3.3.

The fluorescence from the test section is collected at right angles to the sheet and reflected from two mirrors and into the intensified CCD camera. The mirrors are the reflective filters discussed in Sect. 5.2, and are placed at 15° angle of incidence. The intensified CCD is described in detail in Sect. 3.2.2, and is characterised in Sect. 5.3.2.

6.2.2 Procedure

The experimental procedure is the same as that described in Sect. 3.2.4. The only difference was that the delay between shock reflection and firing the laser was 350 μs.

6.2.3 Imaged Region

An alignment grid printed on a piece of paper was back illuminated with a tungsten light source and used to define the imaging region of the camera. This grid allowed the distance from the nozzle exit to be measured and also the camera to be oriented so that the horizontal axis corresponds to the flow direction in the LIF images. For these experiments, only half of the freestream was imaged. The imaged region is defined by the box in Fig. 6.2 which shows a rotational temperature map at the nozzle exit. The region is 50×52 mm. The camera actually views about a 55-mm wide region, but the laser sheet is reduced to 50 mm so that the edges of the sheet observed in the LIF image can be correlated with the sheet-energy correction image. The imaged region starts at 16 ± 2 mm from the nozzle exit and includes a portion of the centreline as well as the edge of the core flow. Here, allowance has been made for the recoil of the shock tunnel when it is fired, which causes the nozzle to move 8 ± 1 mm further away from the model. The portion of the temperature map below the imaged region in Fig. 6.2 is the reflection of temperature about the centreline.

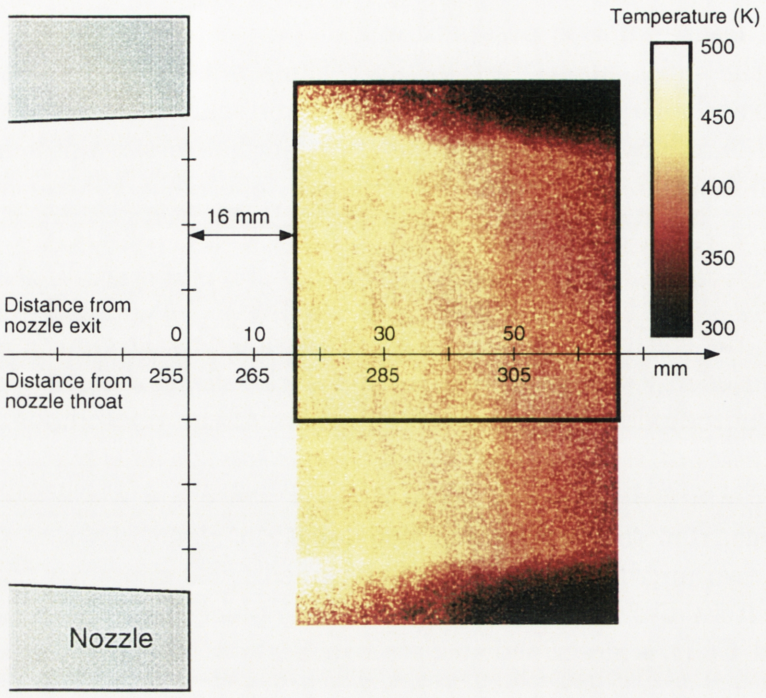

Figure 6.2: Schematic of nozzle exit. The box indicates the region imaged by the camera. The imaged region is 50×52 mm. The image shown is a rotational temperature map which has been reflected about the flow centreline.

This allows the width of the core flow to be visualised and provides a reference for determining the size of flow features.

6.2.4 Driver-Gas Contamination

Figure 6.3 shows a series of LIF images obtained during an experimental run. It can be seen that there are regions of no LIF signal, primarily in the centre of the nozzle flow. The regions appear to have turbulent structure, and in some cases the LIF signal vanishes completely in these regions. Of the 68 tunnel runs performed for the freestream measurements, some 22 showed these turbulent dark regions and another 8 had anomalously low signal. These dark regions may be explained as pockets of driver gas[†] that have arrived prematurely, perhaps due to instabilities at the contact surface or jetting of driver gas into the nozzle-reservoir region via shock wave/boundary layer interaction (see Sect. 4.2.3). The driver gas has no NO in it and thus produces no LIF signal. It is interesting to note that very little mixing has occurred, as indicated by the higher contrast of some of the driver-gas pockets. At later test times, LIF images display a gradual uniform decrease in intensity which

[†] *Examiner's note:* This is speculative. Another possibility is 'dust clouds'.

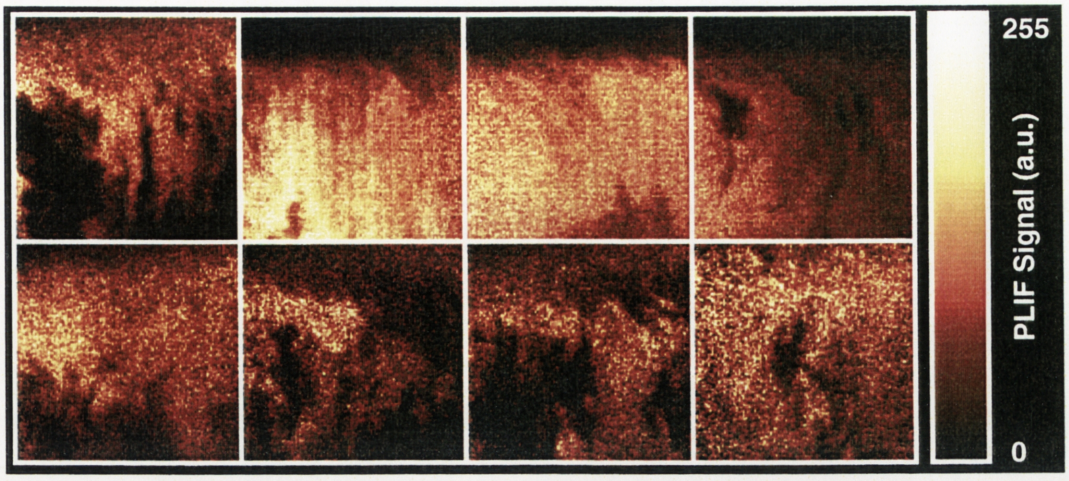

Figure 6.3: A montage of LIF images showing pockets of driver-gas contamination. Each image is half of the core flow as indicated by the camera viewing region in Fig. 6.2. Approximately one third of the images acquired showed this contamination.

may be due to either a drop in the nozzle-reservoir pressure and hence nozzle-exit density, or an increased proportion of driver gas uniformly mixed with the test gas, or both.

The shock-tunnel literature generally discusses a gradual increase in the driver gas concentration in the flow, rather than the sudden arrival of cold pockets of driver gas. Previous techniques for driver-gas detection may be insensitive to these discrete quantities of driver gas arriving prematurely, especially if the detectors were used away from the centreline. Also, for a flow velocity of 3 km/s, a pocket of driver gas 20-mm long would only take 7 μs to traverse a stationary point in the flow, and thus driver-gas detectors would require a suitably fast time response. Static pressure, mass spectrometry and heat-transfer measurements may easily miss these driver-gas pockets. They should, however, be observable with schlieren photography or interferometry due to the density differences between the driver gas and test gas. There is a vast amount of shock-tunnel data from schlieren photography and interferometry in the literature which do not report such findings, and therefore it is possible that these driver-gas pockets may be an artifact peculiar to the current test facility.[†]

In the analysis below, the LIF images with signs of driver-gas contamination have been rejected. The images with anomalously low signal have also been rejected

[†] *Examiner's comment.* Detection of these structures by schlieren or interferometry is unlikely due to: freestream densities are usually very low so that even major density variations are below the detection limits of these techniques; and both methods are integrated across the flow which, when combined with the turbulent nature of the regions, could disguise their presence.

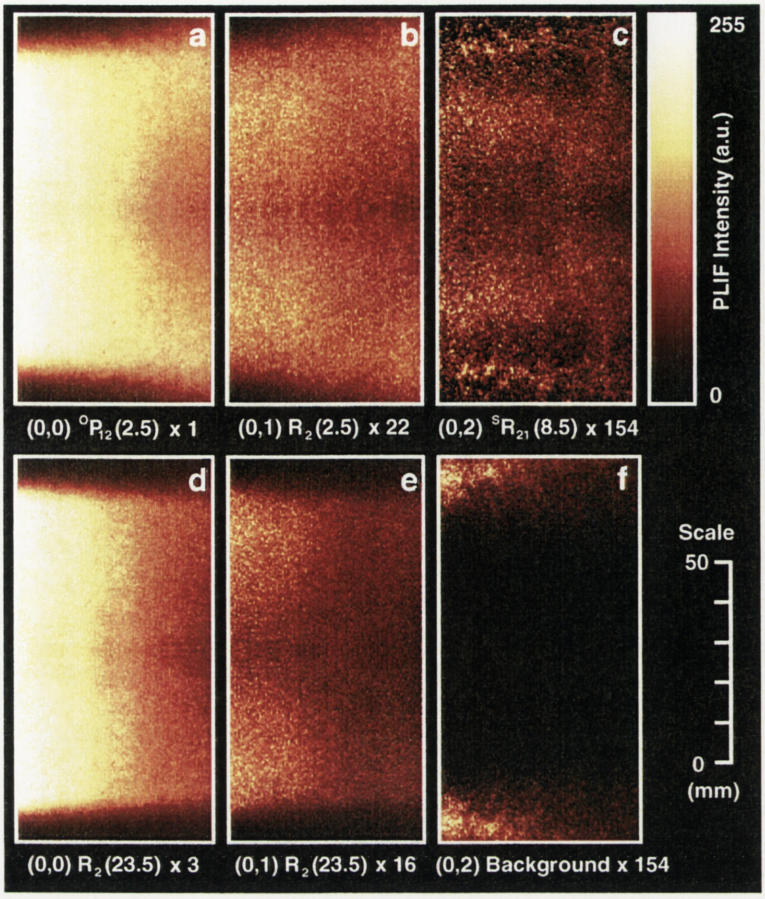

Figure 6.4: Averaged LIF images of the freestream. The flow is from left to right. Images (a), (b) and (c) are for the low-J lines and show the same characteristic shape. Images (d) and (e) are for the high-J lines. Image (f) is the signal produced when the laser is detuned from a transition at 245 nm. Image (c) includes the correction for the non-resonant background (f).

assuming that the cause is related to the facility and is not a statistical fluctuation associated with the LIF process. If, in fact, the reason for the low signal is due to laser-mode fluctuations then this selection process would cause an artificially high averaged signal. However, the number of images rejected on the basis of low signal is small compared to the total number of images taken and is not expected to introduce any significant uncertainty.

6.3 Freestream Results

Figure 6.4 shows the averaged LIF images taken of the freestream at the nozzle exit. The images were acquired at different camera gains and the numbers in Fig. 6.4

	v''	Transition Branch	J''	Total shots	Driver Gas	Averaged	Gain
Freestream: Gate = 650 ns							
1.	0	$^{O}P_{12}$	2.5	12	4	8	6.5
2.	0	R_2	23.5	12	4	8	6.8
3.	1	R_2	2.5	18	10	8	7.2
4.	1	R_2	23.5	14	6	8	7.2
5.	2	$^{S}R_{21}$	8.5	10	4	6	7.5
		Detuned		5	0	5	7.5
Hemisphere: Gate = 100 ns							
6.	0	P_1	35.5	5	0	5	6.6
7.	1	P_1	35.5	5	0	5	6.6
8.	2	P_1	35.5	5	0	5	6.6
		Laser off		6	0	5	6.6

Table 6.1: Summary of the experimental conditions for the freestream and hemisphere temperature measurements.

indicate the relative magnitude of the signals (*e.g.*, the signal from the (0,0)$R_2(23.5)$ transition is approximately 3 times less than that from the (0,0)$^{O}P_{12}(2.5)$ transition). This scaling factor also accounts for the spectral response of the photodiode used to measure the laser energy (see Sect. 5.3.3). Each image in Fig. 6.4 is the average of 6–8 tunnel runs. Each image obtained from a single tunnel run was corrected for camera background offset, absolute laser energy, and the variation of the laser energy across the image. The background on the intensified CCD was observed to fluctuate from frame to frame. Each image was corrected for the background by scaling a standard background image against a region in the image that was known to have no signal (*i.e.*, laser scatter, fluorescence or emission).

Table 6.1 indicates the camera settings and the number of images averaged for each transition. Several 'no laser' shots were also performed to verify that there was no flow luminosity. The fluorescence lifetime in the freestream is approximately 114 ns and so an intensifier gate of 650 ns was used. This allows greater than 99% of the signal to be collected and about 40 ns between the start of the gate and the laser pulse to account for time jitter in the triggering system.

The reflective filters efficiently block the laser wavelength when excitation is performed in the (0,0) and (0,1) bands. However, elastically-scattered laser light is not filtered out by the detection system for excitation of the (0,2) band near 245 nm. To account for this, several runs were performed with the laser detuned from any NO transitions. The average of 6 such images is shown in image (f) of Fig. 6.4. The signal occurs in the edge of the core flow, most likely due to Mie scattering from particulate matter that has been entrained in the nozzle-wall boundary layer.

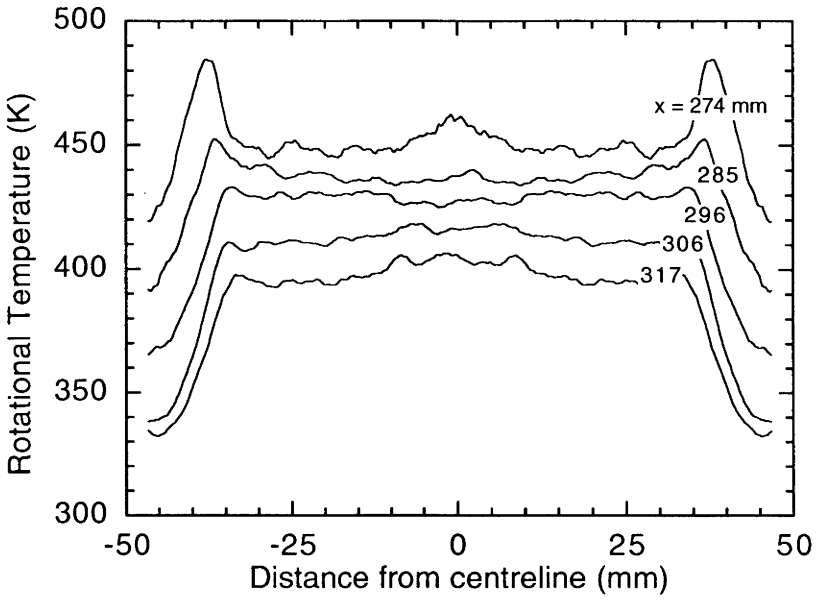

Figure 6.5: Cross sections through the rotational temperature map perpendicular to the flow direction. The temperature map is derived from transitions in the (0,0) band. The cross sections are labelled by the distance x from the nozzle throat. The data in each cross section from -5 mm to -50 mm are the reflection of the data about the centreline.

There is no signal in the central core of the flow. Image (c) is a corrected LIF image obtained by subtracting image (f) to account for the elastically-scattered laser light.

6.3.1 Rotational Temperatures

A rotational temperature map was calculated by taking the ratio of images (a) and (d) in Fig. 6.4 and using Eq. 2.68. The temperature map produced is shown in Fig. 6.2. However, a more quantitative assessment can be made by examining the vertical cross sections given in Fig. 6.5. Each cross section was made by averaging a 50-pixel-wide vertical slice through the image. The pixel density was 9.2 pixels/mm, and so this corresponds to approximately a 5-mm wide slice. The data was further smoothed by running a 20-pixel-wide (2 mm) integration window through the data. The cross sections are at 10-mm intervals and clearly show the decrease in temperature with distance from the nozzle exit. The first slice, corresponding to 274-mm from the nozzle throat, shows a marked temperature rise at the edge of the core flow. This temperature rise is due to the nozzle-wall boundary layer, which on closer examination of the image in Fig. 6.2, can be seen to agree very well with the position of the nozzle wall. Slices taken further downstream show a relatively

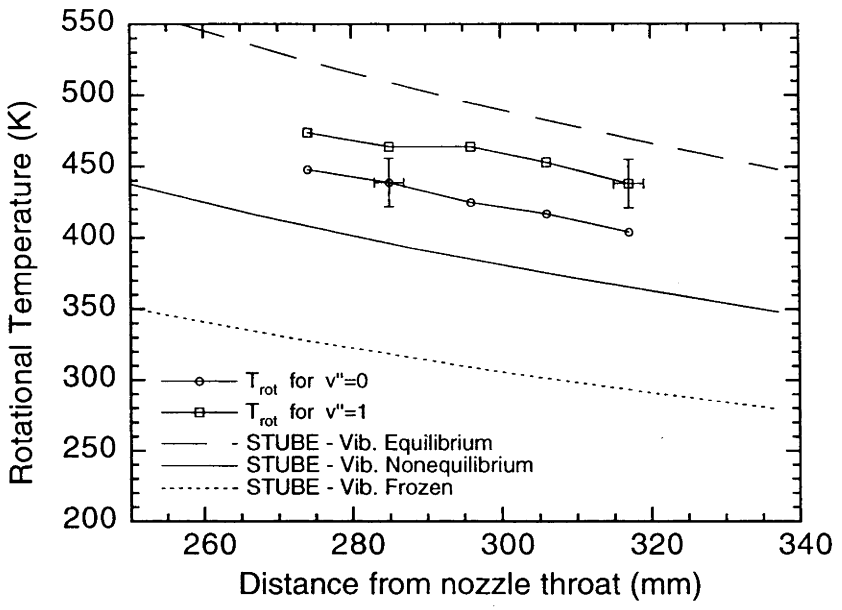

Figure 6.6: Rotational temperatures along the centreline of the flow compared with STUBE calculations. The experimental temperatures are from obtained from exciting the (0,0) and (0,1) vibrational bands. The temperature error bars are due to laser-mode fluctuations.

uniform temperature profile. A second temperature map was made from transitions in the (0,1) band and showed similar characteristics, however the signal-to-noise ratio was significantly poorer.

There are random and systematic contributions to the uncertainties in the temperature measurements. The random errors are due to shot noise and fluctuations in the laser spectral profile. Since high spatial resolution is not a concern here, but temperature accuracy is, the temperature can be averaged over a small region to eliminate the contributions from shot noise to the uncertainties. Hence, the temperature was averaged over a 2 × 10 mm region at several points along the flow centreline. The results are shown in Fig. 6.6 for temperatures determined from transitions in (0,0) and (0,1) bands. The standard deviation in the averaged signal is 2% and 7%, respectively. Each 2 × 10 mm region corresponds to approximately 900 pixels, so the standard error in the mean due to shot noise becomes negligible ($2/\sqrt{900} \approx 0.07\%$). Averaging images from 8 tunnel runs for each transition has also reduced shot-noise contributions.

The temperatures derived from exciting the (0,1) band are higher than those from the (0,0) band excitation by about 30 K. Shown for comparison are the temperatures calculated from STUBE using the reservoir conditions given in Table 4.3 of T_0 = 4219 K and P_0 = 27.9 MPa. The measured (0,0) band temperatures are

slightly higher than the calculated temperatures by approximately 40 K. However, both measurements have the same characteristic downward trend as the calculations from STUBE, and they also fall between the frozen- and equilibrium-vibration calculations. The error bars in Fig. 6.6 are due to the laser-mode fluctuations, as described below. The two experimental temperatures agree with each other to within the experimental uncertainties.

The major factors influencing the calculated nozzle-exit rotational temperature are the vibrational relaxation modelling and nozzle-reservoir conditions. There is little influence from chemical effects because the flow is 98% N_2. To verify this, STUBE was executed assuming chemical equilibrium, and the resulting temperature was only 1 K higher. In Sect. 4.5.1, it was suggested that the vibrational modelling would underpredict the vibrational freezing temperatures. If the vibrational temperatures were higher, then more energy would be locked up in the vibrational modes and therefore the rotational temperature at the nozzle exit would be lower. Hence, the measured temperatures are systematically higher than the temperatures predicted by STUBE, even after taking into account the limitations of the vibrational-relaxation modelling.

6.3.2 Random Uncertainties

The major uncertainty in the freestream measurement is due to fluctuations in the laser spectral profile. More precisely, it is due to the fluctuation in the distribution of energy amongst the cavity modes of the laser. In a preliminary test using mixtures of NO and N_2 in the dump tank at room temperature, an estimate of the pulse-to-pulse fluctuations due to mode fluctuations was made. At 10 kPa and 300 K, the standard deviation in the mean LIF signal from 80 laser pulses was 15%. Each pulse was corrected for absolute laser energy fluctuations so as to isolate the contribution from mode fluctuations. For a dye laser cavity of 30 cm, the cavity mode spacing is 0.017 cm^{-1}, which corresponds to 11 modes excited under the 0.18 cm^{-1} FWHM laser profile. The absorption line width for the test conditions was about 0.14 cm^{-1}, while the homogeneous width was 0.06 cm^{-1}. Hence one would expect 8–10 modes under the total absorption profile and about 4 under the homogeneous profile. This can cause a relatively large error, and at the freestream conditions is even more significant. The freestream homogeneous width is 0.02 cm^{-1}, only marginally larger than the mode spacing, which means that the fluctuations would be even more severe than the test case. McMillin (1993) used a computer model of the laser-mode structure to estimate the uncertainty in the overlap integral due to fluctuations in the energy of the modes. However, this assumes that the homogeneous width is much larger than the mode spacing, so that the interaction remains homogeneous. This assumption is tenuous in the present experiment. The most reliable way to determine this value is to measure it experimentally.

A large percentage of the tunnel runs suffered from driver-gas contamination. Nonetheless, it was possible to find a common driver-gas-free region in a majority of the images and therefore to obtain a measure of the LIF signal fluctuations for each transition. The standard deviation in the mean LIF signal for the four $v'' = 0$ and 1 transitions varied from 21% to 28%. These four values were averaged to give a value of 25%. A total of 50 images were used to arrive at this value and therefore it is likely to be a reasonable estimate of the uncertainty due to laser-mode fluctuations.

The uncertainty in a single measurement due to laser-mode fluctuations is 25%. The uncertainty in the average of eight LIF images is 9.4%. The uncertainty in the temperature is given by

$$\frac{\delta T}{T} = \frac{kT}{\Delta E}\frac{\delta R}{R}\,, \tag{6.1}$$

where the error in the signal ratio R is obtained by combining the relative uncertainties from the two signals S_{f1} and S_{f2} according to

$$\frac{\delta R}{R} = \sqrt{\left(\frac{\delta S_{\mathrm{f1}}}{S_{\mathrm{f1}}}\right)^2 + \left(\frac{\delta S_{\mathrm{f2}}}{S_{\mathrm{f2}}}\right)^2}\,. \tag{6.2}$$

For the freestream rotational temperature measurements, $\Delta E/kT = 3.25$, and therefore the uncertainty in the rotational temperature due to laser-mode fluctuations is 4%.

Other sources of random error include the laser-energy measurements, camera gain and gate repeatability, time jitter in the laser system, laser-tuning inaccuracies and flow repeatability. All of these uncertainties are negligible in comparison with the laser-mode fluctuations.

6.3.3 Systematic Uncertainties

Systematic uncertainties have been reduced or avoided by careful experiment design and transition selection as indicated in Table 5.3. The estimated errors due to beam attenuation, signal interference and saturation produced a combined error of less than 1 K. Even in the shock layer, where beam attenuation is greater than 1% per cm path length, the contribution to the temperature uncertainty is only 0.7%. The low uncertainties are due to the particular signal contributions cancelling partially or fully in the signal ratio, and also due to the favourable values of $\Delta E/kT$. It is possible that transition overlaps or other interferences may occur that are not predicted by the calculations, but these can only be discovered by temperature verification experiments. Other possible sources of systematic error include the photodiode spectral response, radiative trapping and calibration of the camera gain

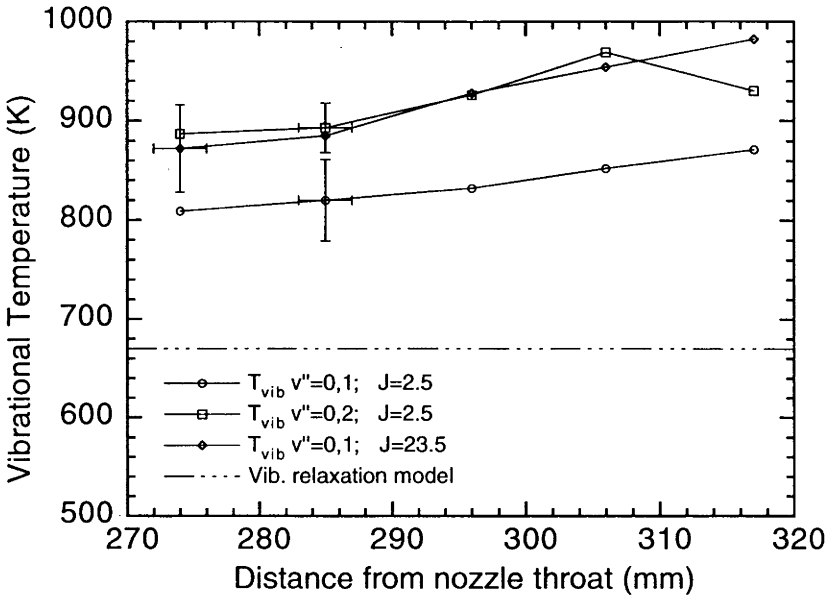

Figure 6.7: Averaged vibrational temperatures at various points along the centreline of the flow compared with STUBE calculations.

control.

6.3.4 Vibrational Temperatures

Freestream vibrational temperatures were also determined from the LIF images shown in Fig. 6.4. Three vibrational temperatures may be determined. First, the (0,0)$^{O}P_{12}(2.5)$ and (0,1)$R_2(2.5)$ transitions are used to determine a temperature. The energy separation is 1876 cm^{-1}, and for a vibrational temperature of approximately 900 K, $\Delta E/kT = 3.0$. Another measurement can be made of the same temperature by using the (0,0)$R_2(23.5)$ and (0,1)$R_2(23.5)$ transitions. Finally, a measure of the temperature using the $v'' = 2$ level can be obtained by combining (0,0)$^{O}P_{12}(2.5)$ and (0,2)$^{S}R_{21}(8.5)$ transitions. Despite the difference in rotational quantum number, these two transitions have approximately the same values of $F_{J''}$ so that the rotational-temperature dependencies cancel. For the last measurement, $\Delta E = 3724$ cm^{-1}, and therefore $\Delta E/kT = 6.0$, making this measurement very insensitive to measurement uncertainties.

A similar approach is taken to the rotational measurements to reduce shot-noise uncertainties by averaging the temperature over a 2 × 10 mm region. Figure 6.7 shows the vibrational temperatures at various distances from the nozzle exit along the flow centreline. The temperature error bars are due to laser-mode fluctuations,

which amount to 5% for the $v'' = 0, 1$ measurements, and 3% for the $v'' = 0, 2$ measurements.

The first observation that can be made from Fig. 6.7 is that the vibrational temperatures are significantly higher than those predicted from the vibrational model presented in Sect. 4.5.1. At a distance of 285 mm from the nozzle throat, the measured temperatures are 820, 885 and 893 K, compared with the value from the vibrational relaxation model of 670 K. The underprediction of the vibrational freezing temperature was expected due to the lack of vibrational relaxation data. The $(0,0)^{O}P_{12}(2.5)/(0,1)R_2(2.5)$ measurement is 70–100 K lower than the other two measurements.

The estimated systematic uncertainties for the vibrational temperature measurements due to beam attenuation and signal interference are $\delta T/T \approx +0.7\%$ and $\approx +0.3\%$, respectively. Uncertainties due to saturation are negligible because the laser energy was varied to achieve the same amount of saturation for each transition. The Doppler width decreases by 8.0% between 225 and 245 nm, which causes the overlap integral to increase by 2.2%. This produces measured temperatures that are systematically high by +0.4%. Combining these uncertainties, the estimated systematic error for the vibrational measurements is +0.85%, or +7 K.

The next surprising observation is that the measured vibrational temperature is rising with distance from the nozzle exit rather than being constant as expected. The laser-mode fluctuations cause the signal in the whole image to fluctuate, not to vary within an image. The upward trend in the temperature is evident in all the three of the temperature measurements so it is unlikely to be caused by a single erroneous image. Whether this is an artifact of the flow, or of the measurement technique, it is difficult to say. After the excitation process, the fluorescence and signal-collection processes are identical for all transitions. Therefore, for the temperature rise to be caused by a technique error, the error must occur in the absorption process. The overlap integral increases by ≈3% across the imaged region (30 mm) for each transition. However, the ratio of overlap integrals remains relatively constant, thereby cancelling the effects due to the variations in the temperature and pressure. Temperature verification experiments are required to verify that the temperature rise is caused by a measurement error.†

†*Examiner's suggestion:* Camera non-linearities may be responsible for the rise in vibrational temperatures with distance from the nozzle exit. The data for the $v'' = 1$ and $v'' = 2$ levels were taken at high intensifier gains. The signals decrease with distance from the nozzle exit (see Fig. 6.4), and if the upstream signals saturated the intensifier, the temperature behaviour observed in Fig. 6.7 would result. The camera linearity could not be tested completely as described in Sect. 5.3.2

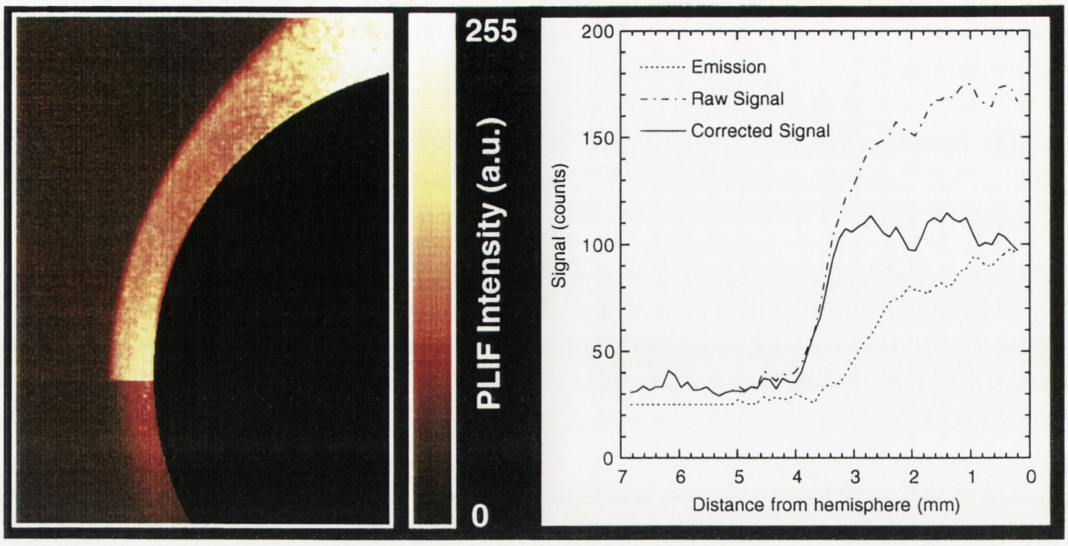

Figure 6.8: Flow over the 25-mm radius hemisphere. The top half of the image is the combined LIF and flow luminosity signal, while the bottom half is the flow luminosity only. The inset shows streamwise cross sections through stagnation region. The LIF and luminosity images are the averages of 5 and 6 tunnel runs respectively.

6.4 Hemisphere Results

The hemisphere has a 25.4-mm radius and was placed at 286 ± 2 mm from the nozzle throat. The stagnation region pressure and temperature were calculated to be 295 kPa and 4146 K using STUBE. For LIF imaging in the hemisphere shock layer, higher intensities could be utilised due to the higher saturation intensities. This was also desirable due to the competition from flow luminosity, which made it necessary to increase the LIF signal as much as possible. As a result, a lower camera gain of 6.6 could be employed which also reduced the level of shot noise. The laser sheet was about 25-mm wide and 0.8-mm thick and passed through the stagnation point on the hemisphere. The laser intensity was estimated to be approximately 425 kW/cm^2 which gives an $I/I_{\text{sat}} \approx 0.03$ in the stagnation region. Laser-mode fluctuations are not a significant problem in the shock layer because the Doppler and homogeneous widths are both larger than the laser linewidth.

Five images were taken for each vibrational band and corrected for CCD background, laser scatter, flow luminosity, laser sheet profile and total laser energy. The $P_1(35.5)$ transition was used for the three vibrational bands, $v'' = 0, 1$ and 2. The flow luminosity was strongest at the stagnation point and amounted to about 25% of the CCD's dynamic range (60 counts out of 256), even when the intensifier gate was at its minimum of 100 ns.

Flow over a hemisphere is shown in Fig. 6.8. The top half of the image is the combined LIF and flow luminosity signals, while the bottom half is emission only. The inset shows streamwise cross sections through the stagnation region for the emission and combined signals, and also the corrected LIF signal after subtracting the emission. The emission signal rises slowly behind the shock while the corrected LIF signal rises rapidly at the shock and then remains relatively constant. This might at first suggest that the luminosity is nonuniform in the shock layer. However, it should be remembered that the emission signal is integrated along the line of sight to the camera. If the emission were emitted uniformly in the shock layer, then viewing from the side would produce a signal that increased gradually between the shock and the body, as is observed in Fig. 6.8. Thus, the shape of the emission does not necessarily suggest that the stagnation region is nonuniform.

To correct for the flow luminosity, 6 tunnel runs were performed with 'no laser'. The emission was observed to fluctuate significantly (10–60 counts) as the primary shock speed varied ($\approx$3%) from shot-to-shot. A general trend of more emission with higher shock speeds was definitely observed, but unfortunately the large magnitude of the fluctuations negated the possibility of making an accurate fit of shock speed against emission intensity. The standard deviation for the 6 luminosity images was 30% of the mean. The fluctuations in the flow luminosity are the major source of uncertainty in these shock-layer measurements.

The emission needs to be subtracted from the raw LIF signal before it is corrected for variations in the laser sheet energy, otherwise the emission signal will be scaled as well. Without any way of determining the magnitude of the emission contribution to the LIF signal from an individual tunnel run, the data cannot be corrected. Therefore, to correct for the flow luminosity in each image, it was assumed that the LIF signal was approximately constant behind the shock. This is a reasonable assumption based a CFD analysis performed by Danehy et al. (1997), who used the 2D-axisymmetric inviscid code of Mundt (1992). The code includes nonequilibrium chemistry and vibration was assumed to be in equilibrium. The results from the analysis indicate a relatively uniform stagnation region for the current freestream conditions. Based on this assumption, the averaged emission image was scaled appropriately and subtracted from each individual LIF image to obtain a corrected image with an approximately constant signal in the stagnation region (Fig. 6.8). Each image was then corrected for variations in the laser-sheet-intensity profile. The five images from each vibrational band were then averaged to produce three final images, one for each band. A vibrational temperature map was then derived using the multi-line method described in Sect. 2.7.4.

Figure 6.9 shows the measured vibrational temperature map. The bottom half of the image in Fig. 6.9 is a temperature map calculated using the CFD code described by Danehy et al. (1997). Also shown in Fig. 6.9 is a streamwise slice through the stagnation region. The measured vibrational temperature is 4500 $\pm$ 270 K. This uncertainty was obtained by assuming that the correction procedure for the emission

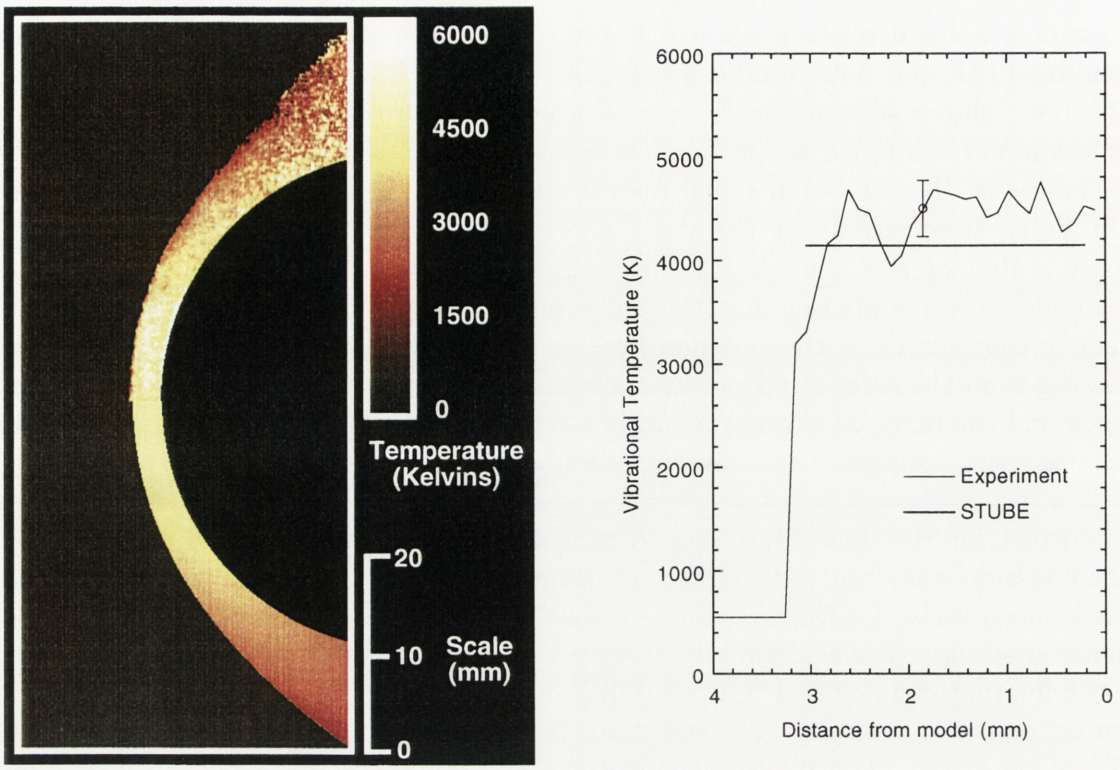

Figure 6.9: Vibrational temperature measurements in the shock layer on a hemisphere. The top half half of the image (left) is the measured vibrational temperature map and the bottom half is the calculated temperature map. The plot (right) shows a horizontal cross section through the stagnation region.

used above is valid. A conservative estimate of 10% was used for the uncertainty in the correction procedure for a single image. Five images were averaged which gives the error in an averaged LIF image of 5%. Combining images and using $\Delta E/kT = 1.18$ gives a temperature uncertainty of 6%, or 270 K. If, on the other hand, we were to simply subtract the averaged emission image from each LIF image, then the uncertainty in the corrected image would be on the order of the emission fluctuations, or 30%. The uncertainty in the temperature would become 18%, or 800 K.

The systematic uncertainties due to beam attenuation and signal interferences are $+0.7$ and -0.4 %. A more significant error occurs due to the variation in the Doppler width between 225 and 245 nm. The Doppler width decreases by 8.3% and, therefore, the overlap integral increases by 4.2%. This produces a temperature uncertainty of +3.5%, or +160 K. However, the overlap-integral ratio is relatively insensitive to changes in the temperature, pressure and detuning, and thus it is possible to correct for this uncertainty because it can be calculated relatively accurately.

Note that it is difficult to find suitable rotational levels with the same energy spacing to make a rotational temperature measurement at this temperature. Utilising the higher vibrational bands reduces the overall measurement inaccuracies by increasing the value of ΔE. Also, at 4500 K the signal from the excitation of the $v'' = 2$ level is 44% of that from excitation of the $v'' = 0$ level. This variation in signal strength is easily measurable with the limited dynamic range of the current detection system even without varying the camera gain. The use of even higher levels may also be feasible. However, a rotational temperature measurement would have the advantage that both transitions would be at approximately the same wavelength, thus removing the need for spectral corrections to the laser energy measurements, changing of laser dyes, corrections due to overlap-integral variations, and concerns with filtering of elastic laser scatter.

Note that in Fig. 6.9, the discrepancy between theory and experiment for the shock stand-off distance can be attributed entirely to the incorrect assumption of vibrational equilibrium in the CFD code (Danehy et al. 1997). Unfortunately, the assumption of vibrational equilibrium can not be altered for this CFD code.

6.5 Discussion

Here we discuss the important points presented in the results section and suggest possible improvements to the technique.

- *Laser-mode Fluctuations.* Several approaches are possible to reduced the influence of mode fluctuations. First, the direct approach would be to measure the mode energy distribution with an etalon. As explained by McMillin (1993), to resolve the mode structure would require a finesse of approximately 60 in the UV which is difficult to achieve at a reasonable cost. An alternative approach is to use a reference cell at similar conditions to the freestream, and split off part of the laser beam to perform LIF in the cell simultaneously with that from the shock tunnel. Fluctuations in the LIF images can then be reduced by normalising with the reference cell LIF signals. This approach was used by Wollenhaupt et al. (1997) to reduce the standard deviation in the temperature measurements by a factor of 3 over the absolute energy correction alone.

- *Redundant temperature measurements.* The rotational measurement made with the $v'' = 1$ transitions is 40 K higher than that from the $v'' = 0$ transitions. Similarly, one of the measured vibrational temperatures is significantly lower than the other two. Both of these measurements have the $(0,1)R_2(2.5)$ transition in common. If it is accepted that the fluorescence image from this transition is approximately 20% below its true mean value due to laser-mode fluctuations, this correction drops the rotational temperature by 6% (30 K)

and raises the vibrational temperature by 7% (60 K), bringing both temperatures into excellent agreement with the other measurements. However 20% is a relatively large change even for laser-mode fluctuations. It may also be possible that some systematic error has reduced the signal for this transition causing the measurement discrepancies. In particular, the camera gain was varied to make these measurements and perhaps backlash in the gain control knob has contributed. Interference from other transitions would increase the signal rather than decrease it. Temperature verification experiments may indicate unexpected systematic errors, and may also be used to verify the data analysis technique. Performing redundant temperature measurements by using multiple transitions, as in the present experiment, is a useful method for highlighting possible systematic errors.

- *Flow repeatability.* The flow conditions vary from shot to shot. The standard deviation in the shock timing is 4 μs which corresponds to a 10 K uncertainty in the calculated freestream temperature (see Sect. 4.6). The values used for the CFD calculations were obtained from the average of many tunnel runs used during the pitot-pressure survey. Improved agreement between theory and experiment could be obtained by using the measured shock speeds and nozzle-reservoir pressures for the actual tunnel runs from which the PLIF results were taken. Care must be taken such that the runs used for one transition do not have significantly different shock speeds from those used for the others. In the current experiment, the shock speeds only varied enough to change the freestream temperature by about 5 K. Therefore, flow repeatability cannot be used to explain the discrepancies between experiment and CFD.

- *Flow luminosity.* Emission in the shock layer is the main source of uncertainty in the hemisphere stagnation-point measurements, since the broadened absorption linewidths have removed the uncertainty due to laser-mode fluctuations. The flow luminosity can be either decreased, or, more importantly, accounted for in the analysis procedure. The fluorescence lifetime is approximately 4 ns, and so the total signal duration, including laser pulse length of 25 ns, is approximately 45 ns. A shorter gate could therefore be employed to reduce the emission by at least a factor of 2. However, there will still remain some contribution from the emission. The emission signal needs to be observed in the LIF image in a region where there is no LIF signal. Then its magnitude can be determined, and the averaged emission image scaled appropriately to correct the raw LIF image. On a wedge or cone, this is possible because the laser sheet is blocked by the model and so luminosity is observable on opposite side to the LIF. For the hemisphere, another object may be added to the flowfield downstream which will produce an emission signal. It is important, however, that this object does not disrupt the flow around the hemisphere. An alternative approach would be to use a second camera gated just before the laser pulse, or perhaps even an ungated camera to record the luminosity. An unintensified CCD should be adequate for this purpose.

	Measured	Calculated
Freestream T_{rot} (K)	439 ± 20	396 ± 10
Freestream T_{vib} (K)	890 ± 30	670
Hemisphere T_{vib} (K)	4500 ± 270	4146

Table 6.2: Summary of the measured and calculated temperatures. The hemisphere measurement is systematically high by 160 K due to variations in the spectral-overlap integral.

- *Shock attenuation.* The disagreement between the measured rotational freestream temperatures and the calculated temperature from STUBE brings into question the correction to the shock speed made in Sect. 4.2.2. The shock speed is more likely to decrease rapidly at the start of the shock tube and be relatively constant near the nozzle-reservoir region. However, the estimation of the shock attenuation was made by placing a third transducer 305 mm upstream of the nozzle-reservoir transducer, and the average speed between these last transducers is only 1% faster than the corrected speed that was actually used. Therefore, in this case, the linear extrapolation could only introduce at most a 1% error in the shock speed.

  Improved agreement between the measured freestream rotational temperature of 439 ± 20 K and STUBE is achieved by increasing the nozzle-reservoir temperature to 4535 K. This corresponds to an incident shock speed of 2.38 km/s, which is very close to the unattenuated average shock speed of 2.39 km/s. A nozzle-reservoir temperature of 4535 K gives a temperature of 4485 K immediately behind the normal part of the shock on the hemisphere. Therefore, a higher nozzle-reservoir temperature also gives improved agreement with the hemisphere shock layer temperature of 4500 ± 270 K. In fact, if the accuracy of the hemisphere measurements could be improved, they could be used to test the validity of the ESTC nozzle-reservoir temperatures. The total temperature can drop through the nozzle expansion but not increase, so that this measurement would provide a minimum for the nozzle-reservoir temperature.

The temperatures measured in this chapter at 285 mm from the nozzle throat are summarised in Table 6.2. The original STUBE calculations are also presented for comparison. The measured rotational and vibrational temperatures shown in Table 6.2 are those obtained without the use of the $(0,1)R_2(2.5)$ transition.

Chapter 7

Conclusions and Recommendations

7.1 Summary

PLIF temperature measurements were performed in a free-piston shock tunnel. A single laser/camera system was used to measure rotational and vibrational temperatures in the freestream and in the shock layers on a wedge, a cylinder and a hemisphere. Two different laser sources were used to excite NO via the $A^2\Sigma^+ \leftarrow X^2\Pi$ transition between 225 and 245 nm. The first was a Raman-shifted tunable excimer laser which was restricted to excitation of the (0,0) band near 226 nm, and, therefore, was only utilised for rotational-temperature measurements. The other was an excimer-pumped frequency-doubled dye laser which was used to access the first three vibrational bands (v'=0,v''=0–2) and to perform rotational and vibrational temperature measurements. The primary goal of this thesis was to investigate the viability and the application considerations of using PLIF in free-piston shock tunnels. Temperature measurements were compared with computations from CFD codes in an ongoing procedure of testing and validation.

The flows were produced by the T2 free-piston shock tunnel at relatively low enthalpies of approximately 5 MJ/kg and Mach numbers of approximately 7. The flows were characterised with a pitot-pressure survey at the nozzle exit and the results compared with a quasi-one-dimensional nozzle flow code, STUBE. Modifications were made to the code to include vibrational freezing effects. The modelling of vibrational freezing was tested by choosing a flow condition free of chemical and other effects that might compromise data interpretation. To this end, measurements of vibrational and rotational temperatures in the freestream for a low-enthalpy nitrogen condition were performed.

7.1.1 Summary of Raman-Shifted Tunable Excimer Laser Results

Air flows over a cylinder and a wedge were studied by Raman-shifting the 248-nm output of a tunable excimer laser to 225 nm. Three transitions were chosen within the 75 cm^{-1} tuning range, with rotational quantum numbers J''=18.5, 27.5 and 38.5. Rotational temperatures measured in the freestream were in agreement with CFD calculations, whilst shock-layer temperatures on the wedge and cylinder were both lower than the calculated temperatures. The shock-layer calculations depend strongly on the freestream conditions which are usually determined from nozzle-flow calculations.

For the utilisation of the Raman-shifted tunable excimer laser as a PLIF excitation source, the following points are concluded. The tuning range is limited which reduces the possibilities for line selection, and, therefore, restricts the thermometry to temperatures between approximately 300 and 3000 K. A broadband component associated with the laser spectral profile causes weak excitation of nearby lines and therefore results in a systematic error. However, cavity-mode structure is less of a problem for the tunable-excimer laser than for a dye laser due to the longer cavity length. This is one real advantage over dye-lasers, and is used to good effect in experiments that excite NO with ArF excimer lasers at 193 nm. If the problems associated with the broadband component can be overcome or minimised then the Raman-shifted tunable excimer laser can certainly be an effective excitation source for PLIF.

Following these initial thermometry experiments, several improvements were implemented. A new operating condition for the shock tunnel was designed to have a low concentration of NO (1%) in a mostly-N_2 flow (98%). It was characterised with a pitot-pressure survey which determined the influence of boundary layers on the nozzle walls. The boundary-layer influence manifests itself as a reduced nozzle-angle when using the inviscid nozzle-flow code STUBE, and this reduced angle was measured to be $7.0 \pm 0.2°$. The pitot-pressure survey also indicated a slight non-uniformity in the radial pressure distribution at the nozzle exit. The pressure in the centre of the flow was 15% less than that at the edges. Other improvements included the design of the reflective filters to improve the rejection of flow luminosity, and the inclusion of a dye laser for greater flexibility in transition selection.

7.1.2 Summary of Dye-Laser Results

A low-enthalpy N_2 condition was employed for the investigation of the vibrational freezing phenomena without interference from other effects (such as chemistry) which may compromise the data interpretation. Rotational and vibrational temperatures were measured in the freestream using a frequency-doubled dye laser.

The dye laser allowed greater flexibility in transition selection and also vibrational temperatures to be measured. The freestream rotational temperatures showed the same characteristic drop with distance from the nozzle exit as the calculated values, but were approximately 40 K higher than those calculated. The measured NO vibrational temperature of 890 $\pm$ 30 K was higher than the calculated value of 670 K. This was anticipated because the vibrational-freezing model underpredicts the vibrational-freezing temperature due to a lack of vibrational relaxation data. The vibrational temperature was observed to rise with distance from the nozzle exit rather than remain constant as expected. No explanation for this behaviour could be found.[†] A vibrational temperature of 4500 $\pm$ 270 K was measured in the stagnation region on the hemisphere. This measurement was estimated to be systematically high by 160 K due to variations in the overlap integral between 225 and 245 nm. The measured temperature was higher than the value calculated using STUBE of 4146 K. The measured freestream and hemisphere temperatures are higher than those calculated, which questions the validity of the nozzle-reservoir temperature used in the CFD calculations and the method used to obtain it. The uncertainties in the freestream measurements were dominated by laser-mode fluctuations, whereas, in the shock-layer, the major contributions were from flow luminosity and variations in the overlap integral.

7.2 Conclusions

Several important application issues have been considered for the use of PLIF as a diagnostic tool on shock tunnels. These include: spectral filtering of the fluorescence signal to improve the rejection flow luminosity; and modelling of the LIF process to numerically determine the influence of beam attenuation, signal interferences etc., to assist in the selection of appropriate transitions for thermometry. A comparison of two different laser sources for performing PLIF of NO was also performed.

LIF has been used to image flow non-uniformities and to aid in the characterisation of the nozzle flow. In particular, the premature arrival of discrete quantities of driver gas[‡] was observed in the freestream in approximately one third of the tunnel runs. The LIF images from these contaminated flows had to be omitted to prevent erroneous temperature measurements. This discovery may have significant consequences for free-piston shock tunnel research.

The process of CFD validation should commence with the study of simple flows (*i.e.*, continuum, no real-gas effects) and gradually increase complexity of the flow. This approach was employed here to study vibrational freezing, by using a low-enthalpy N_2 flow which removed the competing effects produced by chemical reactions.

[†] *Examiner's note:* Camera non-linearities may be the cause. See footnote in Sect. 6.3.4.

[‡] *Examiner's note:* This is speculative. Another possibility is 'dust clouds'.

In conclusion, PLIF thermometry has been applied to a free-piston shock tunnel with good results. Successful measurement of rotational and vibrational temperatures indicate that PLIF is a valuable technique for the validation of CFD codes. Validated CFD codes are crucial to aerospace design, enabling the accurate prediction of physical and chemical effects influencing vehicle aerodynamics.

7.3 Recommendations for Future Work

The experimental results present some interesting possibilities for future experiments. Some recommendations for future work are presented here:

- *Driver-gas visualisation.* The use of PLIF to visualise the premature arrival of driver gas is an unexpected outcome of the current experiments. It was observed that up to 30% of the tunnel runs showed discrete pockets of driver gas at the nozzle exit. The premature arrival of driver gas in the test section may be due to the jetting of driver gas into the test gas in the nozzle reservoir via shock wave/boundary layer interaction. Modifications to the operating conditions (*e.g.*, undertailoring), or nozzle-inlet design, may be tested to see if they delay or remove the arrival of the pockets of driver gas. LIF imaging may also serve as a useful tool for determining the useful test time of the flow as well as the uniformity of the freestream.

- *Fluctuations in flow luminosity.* The flow luminosity provided the largest uncertainty in the shock-layer measurements because of the inability to accurately subtract it from the LIF signal in the analysis. The magnitude of the emission may be obtained by measuring it in a region of the image where there is no LIF signal. For flows over cones and wedges, the emission can be measured on the opposite side of the model to the LIF. For the hemisphere case, another object may need to be introduced to the flow downstream to produce an isolated emission signal. This procedure may allow the accurate correction for emission and therefore the accurate measurement of the stagnation temperature on the hemisphere. An alternative approach would be to use a second camera gated just before the laser pulse, or perhaps even an ungated camera to record the luminosity. An unintensified CCD should be adequate for this purpose.

- *Temperature verification experiments.* The major problem with the current system is that there is no capability for testing or calibrating of the thermometry. A test cell capable of producing various temperatures and pressures in a controlled way would be ideal for this purpose. Wollenhaupt et al. (1997) uses such a cell for testing of LIF thermometry and to reduce errors due to fluctuations in the spectral overlap integral. Without this system verification, there is always a certain lack of knowledge about the precision of the

temperature measurements. A temperature measurement was performed on a NO/N_2 mixture in the T2 test section at room temperature as an attempt to provide a basic level of confidence and identify any pitfalls with the implementation procedure or data analysis. After some initial difficulties, correct temperatures could be obtained using the two-line thermometry technique. The main difficulty with this setup was the long path length between the test section window and the viewing region of the camera. The 150 mm path length caused the measurement to be very sensitive to beam attenuation, and it wasn't until transitions with similar absorption coefficients were used that correct temperatures were obtained.

- *Laser-mode fluctuations.* The use of the same test cell as mentioned above for normalising LIF signal from the shock tunnel could significantly reduce the influence of mode fluctuations in the freestream measurements. For a temperature measurement performed by averaging 8 images for each transition, the uncertainty in the temperature due to mode fluctuations would fall from 4% to 1.3%, at which point it would begin to become comparable with other experimental uncertainties.

- *Saturation and beam attenuation.* The measurements here were performed with low beam attenuation and saturation. Both of these could be significantly increased to improve the magnitude of fluorescence signals without introducing significant measurement error. However, verification experiments are recommended to ensure that the correct temperatures can be recovered either by post-measurement corrections or by cancellation of the effects in the signal ratio.

- *Nozzle-reservoir conditions.* Some doubt exists over the use of an attenuated shock speed to determine the nozzle-reservoir conditions. PLIF temperature measurements inferred that the nozzle-reservoir temperature may be higher than that calculated from ESTC. The effects not taken into account in ESTC (viscous, radiation and conduction losses; driver gas; shock tube impurities) would all tend to lower the nozzle-reservoir temperature. Further work needs to be done on testing the accuracy of the calculated nozzle-reservoir conditions.

The problem of verifying the vibrational-freezing model has been reduced to a problem of two unknowns: the vibrational freezing temperature of N_2 and nozzle-reservoir temperature. The freestream rotational temperature is dependent on the vibrational-freezing temperature of N_2 and also the nozzle-reservoir temperature. If freestream and nozzle-reservoir temperatures are known, then the N_2 vibrational-freezing temperature can be indirectly determined, thus closing the problem. Measuring the nozzle-reservoir temperature is not an easy task. A minimum temperature may be obtained from stagnation temperature measurements on a hemisphere. Alternatively, the N_2 vibrational-freezing temperature may be measured experimentally, for example with broadband CARS, and, therefore, allow indirect determination of the nozzle-reservoir temperature.

Once confidence is gained with the modelling of vibrational freezing, the problem may be enriched by changing the test gas composition, or increasing flow enthalpy, to introduce chemical effects.

Appendix A

Spectroscopy of Nitric Oxide $A^2\Sigma^+ \leftarrow X^2\Pi$

This appendix briefly describes the $A^2\Sigma^+ \leftarrow X^2\Pi(0,v'')$ electronic transition in NO. It is presented as a working catalogue of equations and constants for calculating line positions and transition strengths. Sufficient data is provided to calculate the rotational energy levels for the v''=0–7 vibrational levels of the $X^2\Pi$ state and the v'=0 level of the $A^2\Sigma^+$state. The equations have been extracted from various sources, but most notably from the excellent review by Di Rosa (1996). In particular, you will find here the information necessary to calculate energy levels, transition energies, Einstein coefficients and Boltzmann fractions, all of which are essential knowledge for performing PLIF thermometry. The equations have been fully implemented as FORTRAN code and compared against published data. For a more complete understanding of the spectroscopy of the NO $A^2\Sigma^+ \leftarrow X^2\Pi$ system see Di Rosa (1996) and Reisel et al. (1992).

A.1 NO $X^2\Pi$ Energy Levels

The ground state of NO is intermediate between Hund's coupling cases (a) and (b) (Herzberg 1989, p. 218). However, for low J the coupling is closer to case (a) and spin-orbit interaction splits the ground electronic state $X^2\Pi_\Omega$ into the two multiplet terms $^2\Pi_{1/2}$ and $^2\Pi_{3/2}$, with a separation of approximately 120 cm^{-1}. Each rotational level in each multiplet term is also split by Λ-type doubling, thereby producing two levels of opposite parity for each J. The energy levels for the two multiplet terms are labelled by F_1 and F_2. The $^2\Pi_{3/2}$ term is associated with F_2 levels ($J = N - 1/2$) and the $^2\Pi_{1/2}$ term is associated with F_1 levels ($J = N + 1/2$). For a given Ω ($= 1/2, 3/2$), the rotational quantum number has the values $J =$

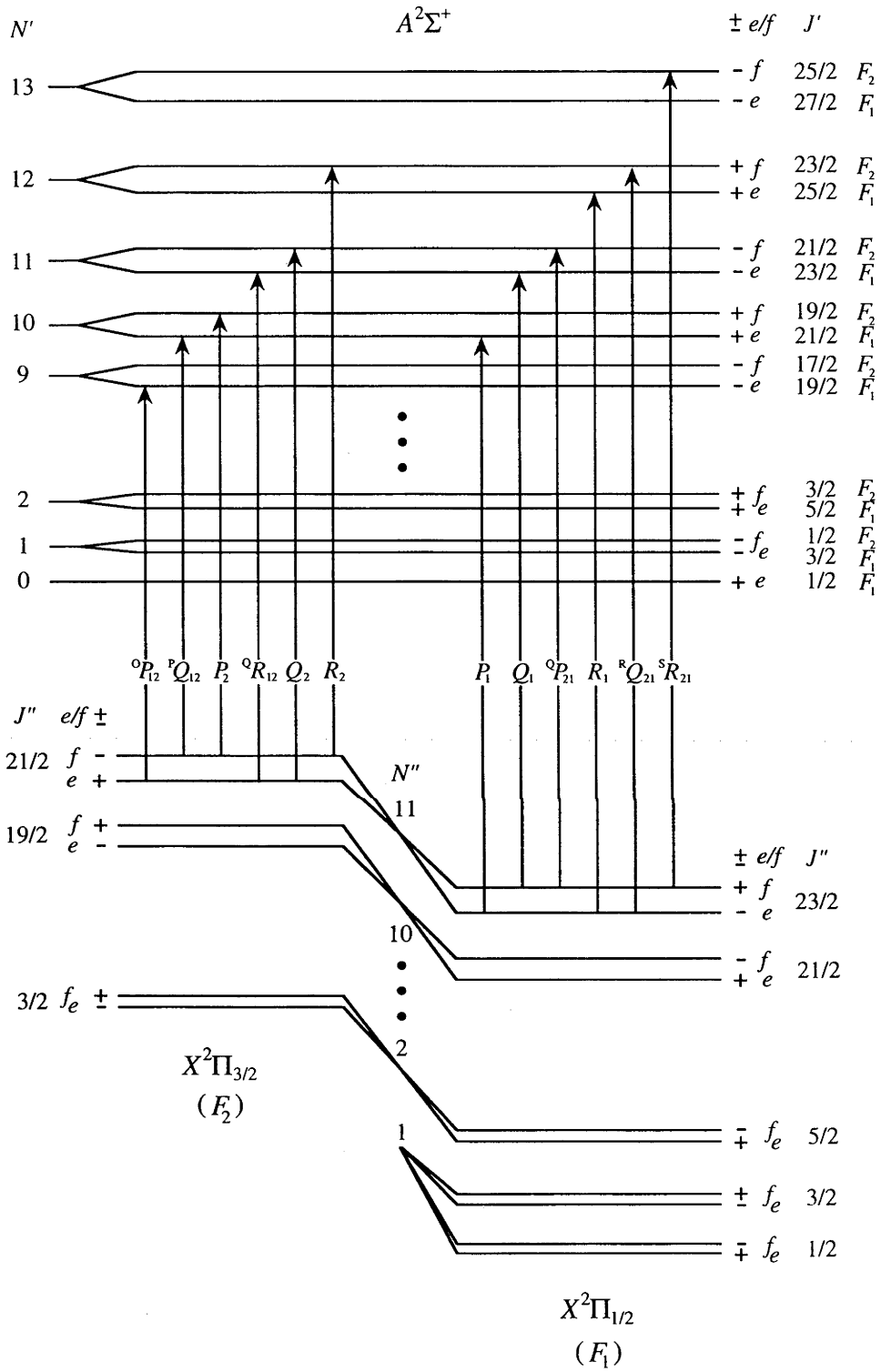

Figure A.1: Energy level diagram for $A^2\Sigma^+ \leftarrow X^2\Pi(0,0)$ transition of NO. (After Di Rosa (1996)). Note the level splittings are not to scale.

$\Omega, \Omega+1, \Omega+2, \ldots$, and also note that J cannot be less than Ω. Therefore, for the $^2\Pi_{1/2}$ state $J = 1/2, 3/2, 5/2, \ldots$, and for the $^2\Pi_{3/2}$ state $J = 3/2, 5/2, 7/2, \ldots$, etc. Fig. A.1 shows the first few energy levels of each electronic state for the $A^2\Sigma^+ \leftarrow X^2\Pi(0,0)$ transition in NO.

The rotational energies for levels F_1 and F_2 are given by (Almy and Horsfall 1937)

$$F_i(J,v) = B_v(J^* - \tfrac{3}{4}) - D_v\left[(J^*)^2 - (J^*/2) + \tfrac{13}{16}\right] + (-1)^i B_v\sqrt{\alpha}\ , \tag{A.1}$$

where i=1,2 represents the multiplet term F_1 or F_2 and where

$$J^* = J(J+1)\ , \tag{A.2}$$

$$\alpha = \frac{(\lambda-2)^2}{4} + \left(\frac{4J^*+1}{4}\right)\left[1 + \mu(4J^*+1-2\lambda) + \mu^2\left(\frac{4J^*-1}{2}\right)^2 - \mu^2\right]\ , \tag{A.3}$$

$$\mu = D_v/B_v\ . \tag{A.4}$$

B_v and D_v are the usual rotational constants which are dependent on vibrational level v''. Accurate values have been given for the $v'' = 0, 1$ levels of $NOX^2\Pi$ but they can also be calculated for higher v'' from expressions such as

$$B_v = B_e - \alpha_e(v+\tfrac{1}{2}) - \gamma_e(v+\tfrac{1}{2})^2\ , \tag{A.5}$$

$$D_v = D_e + \beta_e(v+\tfrac{1}{2})\ . \tag{A.6}$$

The spin-orbit coupling constant λ has a J dependence given by

$$\lambda = \frac{A + A_D(J-0.5)^2}{B_v}\ , \tag{A.7}$$

where A is the spin-orbit splitting constant and A_D is the spin-orbit distortion constant, both of which vary with v''.

The Λ-type doubling splits each spin-orbit term into two, thus producing the four series of energy levels — $F_{1e}, F_{1f}, F_{2e}, F_{2f}$. Therefore, to the value $F_i(J,v)$ in Eq. A.1 we add the Λ-type doubling term given by

$$\Phi_i(J) = (\tfrac{1}{2})(J+\tfrac{1}{2})\left\{\left[+(-1)^i + X^{-1}(2-\lambda)\right](\tfrac{1}{2}p+q) + 2X^{-1}q(J-\tfrac{1}{2})(J+\tfrac{3}{2})\right\} \tag{A.8}$$

according to the rule $F_{i\pi}(J,v) = F_i(J,v) + (-1)^i[\mp]\Phi_i(J)$ where the upper $(-)$ sign in $[\mp]$ goes with parity e and the lower sign with parity f (parity designations are discussed in Section A.3). The constants p and q are the Λ-type doubling coefficients.

Constant	Value [cm^{-1}]	Reference
B''	1.696190	Freedman and Nicholls (1983)
B'	1.986285	"
D''	5.326×10^{-6}	"
D'	5.43×10^{-6}	"
p''	1.1882×10^{-2}	"
q''	5.43×10^{-5}	"
A''	123.0372	"
A''_D	-5.8×10^{-4}	Engleman and Rouse (1971)
ω''_e	1904.405	"
ω'_e	2374.307	"
$\omega_e x''_e$	14.187	"
$\omega_e x'_e$	16.106	"
$\omega_e y''_e$	2.400×10^{-2}	"
$\omega_e y'_e$	-4.645×10^{-2}	"
$\omega_e z''_e$	-9.300×10^{-4}	"
T'_e	43904.67	"
T''_e	0.0	-
γ'	-2.678×10^{-3}	Timmermann and Wallenstein (1981)

Table A.1: Constants for the NO $A^2\Sigma^+ \leftarrow X^2\Pi(0,0)$ band.

Hence, writing this rule out explicitly, we have

$$\begin{aligned} F_{1e} &= F_1 + \Phi_1 \\ F_{1f} &= F_1 - \Phi_1 \\ F_{2e} &= F_2 - \Phi_2 \\ F_{2f} &= F_2 + \Phi_2 \ . \end{aligned} \tag{A.9}$$

The value of X is given by

$$X = \left[\lambda(\lambda-4) + (J+\tfrac{1}{2})^2\right]^{0.5} \ . \tag{A.10}$$

The final expression for the energy levels in either electronic state is given by

$$T = T_e + G(v) + F(J,v) \ , \tag{A.11}$$

where

$$G(v) = \omega_e(v+\tfrac{1}{2}) - \omega_e x_e(v+\tfrac{1}{2})^2 + \omega_e y_e(v+\tfrac{1}{2})^3 + \omega_e z_e(v+\tfrac{1}{2})^4 \ . \tag{A.12}$$

For the NO $X^2\Pi$ state, we define the arbitrary zero-point energy as that point within the ground state with zero vibrational and rotational energy and zero spin-orbit splitting. Hence the system origin T_e is zero for the $X^2\Pi$ ground state. Table A.5 contains a sample calculation for the NO $X^2\Pi(0,0)$ band using the constants in Table A.1. The spectroscopic constants B, D, A, A_D, p and q all vary with v'', and so, when calculating rotational energy levels for other vibrational levels in the $X^2\Pi$ state, the appropriate values should be used (see Table A.4). Huber and Herzberg (1979) is a good general source for spectroscopic constants.

A.2 NO $A^2\Sigma^+$ Energy Levels

The upper state $A^2\Sigma^+$ is described by Hund's case (b). It exhibits spin-rotation splitting only, the magnitude of which is given by γ'. Hence, for each value of $N = N' = 0, 1, 2 \ldots$, we have two energy levels given by

$$F_1(N,v) = B_vN(N+1) - D_vN^2(N+1)^2 + \tfrac{1}{2}\gamma N \quad \text{(A.13)}$$

$$F_2(N,v) = B_vN(N+1) - D_vN^2(N+1)^2 - \tfrac{1}{2}\gamma(N+1)\ , \quad \text{(A.14)}$$

where $J' = N' + 1/2$ for F_1 levels and $J' = N' - 1/2$ for F_2 levels. B_v and D_v are the rotational constants for the A-state and values for the $v' = 0$ level are given in Table A.1.

A.3 Selection Rules, Parity and e/f Designations

Each rotational level has a positive (+) or negative (−) parity, depending on whether the total wavefunction remains unchanged for an inversion of the molecule about its origin. For the $A^2\Sigma^+$ state, this spatial-inversion parity is given by

$$A^2\Sigma^+ \quad \text{parity} = (-1)^{N'}\ , \quad \text{(A.15)}$$

where N' is the rotational quantum number for case (b) coupling. For the $X^2\Pi$ state there are two levels for each J'' due to Λ-type doubling, one being positive and the other negative. The e and f designations are determined for each J according to (Brown et al. 1975)†

$$\text{if parity} = (-1)^{J-\frac{1}{2}} \text{ then level is of type } e$$

$$\text{if parity} \neq (-1)^{J-\frac{1}{2}} \text{ then level is of type } f\ , \quad \text{(A.16)}$$

†This rule applies only to molecules with half-integral J-values.

${}^{\Delta N}\Delta J_{\alpha\beta}(J'')$	$\Delta J_{\alpha\beta}(N'')$	$\Delta N_{\alpha\beta}(N'')$	ΔN	ΔJ	α	β
P_1	P_1	P_1	-1	-1	1	1
R_2	R_2	R_2	1	1	2	2
${}^{S}R_{21}$	R_{21}	S_{21}	2	1	2	1
${}^{O}P_{12}$	P_{12}	O_{12}	-2	-1	1	2
R_1	R_1	R_1	1	1	1	1
${}^{R}Q_{21}$	Q_{21}	R_{21}	1	0	2	1
Q_1	Q_1	Q_1	0	0	1	1
${}^{Q}P_{21}$	P_{21}	Q_{21}	0	-1	2	1
Q_2	Q_2	Q_2	0	0	2	2
${}^{Q}R_{12}$	R_{12}	Q_{12}	0	1	1	2
P_2	P_2	P_2	-1	-1	2	2
${}^{P}Q_{12}$	Q_{12}	P_{12}	-1	0	1	2

Table A.2: Summary of different notations used to describe transitions in the NO $A^2\Sigma^+ \leftarrow X^2\Pi$ system.

or, if the e/f designation is known, the spatial-inversion parity is

$$\begin{aligned} &\text{for } \ e \ \text{ levels, parity} = +(-1)^{J-\frac{1}{2}} \ , \\ &\text{for } \ f \ \text{ levels, parity} = -(-1)^{J-\frac{1}{2}} \ . \end{aligned} \tag{A.17}$$

Therefore, for each level calculated according to Eqs. A.9, a parity can be determined. For example, in agreement with Fig. A.1, the f levels with $J = 23/2$ have parity $= -(-1)^{11} \equiv +$, and the e levels with $J = 23/2$ have parity $= +(-1)^{11} \equiv -$.

The selection rules for transitions induced by electromagnetic radiation are $\Delta J = 0, \pm 1$ and $+ \leftrightarrow -$, or alternatively, in terms of e and f labels they are

$$\begin{aligned} \Delta J = \ \ 0 \quad & e \leftrightarrow f \\ \Delta J = \pm 1 \quad & e \leftrightarrow e, \ \ f \leftrightarrow f \ . \end{aligned} \tag{A.18}$$

The transition energies calculated from the above equations recover the line positions to within +0.2/-0.1 cm^{-1} compared with experimental values (Di Rosa 1996).

A.4 Transition Notation

Applying the appropriate selection rules, we find the $A^2\Sigma^+ \leftarrow X^2\Pi$ system contains twelve branches: six *main* branches and six *satellite* branches. The rotational line strengths for main branches increase with increasing N, while for satellite branches they decrease with increasing N. The most general way to label the transitions is by using the notation ${}^{\Delta N}\Delta J_{\alpha\beta}(J'')$ where $\Delta N = N' - N''$, $\Delta J = J' - J''$, α indicates the term (F_i) in the upper state and β indicates the term in the lower state. Case (b) notation would require $\Delta J_{\alpha\beta}(N'')$ while the alternative notation $\Delta N_{\alpha\beta}(N'')$ is also found in the literature. The letters O, P, Q, R, S are used to represent the numbers $-2, -1, 0, +1, +2$, respectively. By convention, like indices are not repeated and it therefore follows that any branch with two subscripts is a satellite branch. Table A.2 summarises the different notations.

Four of the satellite branches fall very close to four of the main branches. Their separation is determined by the spin-rotation constant γ for the $A^2\Sigma^+$ state since both transitions originate from the same level in the ground state. The separation is usually much less than a linewidth, but increases with N. Because of this overlap, the two lines are usually written using an abbreviated notation (*e.g.*, $Q_1{+}^{Q}P_{21}(27.5)$).

A.5 Einstein A and B Coefficients

From Eq. 15 in Reisel et al. (1992), the Einstein A coefficient for the $nv'J' \leftarrow mv''J''$ transition is given by[†]

$$A_{J'J''} = \frac{g'_n}{g''_n}\left(\frac{\nu_{J'J''}}{\nu_{v'v''}}\right)^2 A_{v'v''} S_{J'J''}\left(\frac{2J''+1}{2J'+1}\right) , \tag{A.19}$$

where, for the NO $A^2\Sigma^+ \leftarrow X^2\Pi$ transition, $g'_n = 2$, $g''_n = 4$, $\nu_{v'v''}$ is the frequency of the vibrational transition, $\nu_{J'J''}$ is the frequency of the rovibronic transition and $S_{J'J''}$ is the normalised Hönl-London factor. The Hönl-London factors can be calculated from the equations of Earls (1935) (see Table A.3) and normalised in the manner described by Di Rosa (1996) such that

$$\sum_{J'} S_{J'J''} = 1 , \tag{A.20}$$

[†]Reisel et al. (1992) uses Hönl-London factors that are normalised to $2J'' + 1$ while those presented here are normalised to unity. Hence, the factors defined here are equal to the those of Reisel et al. (1992) divided by $2J'' + 1$.

For $J = J'' > \frac{1}{2}$	
P_1 ${}^{O}P_{12}$	$\dfrac{(2J+1)^2 \pm (2J+1)U(4J^2+4J+1-2\lambda)}{32J} \left[\dfrac{4}{2J+1}\right]$
P_2 ${}^{Q}P_{21}$	$\dfrac{(2J+1)^2 \pm (2J+1)U(4J^2+4J-7+2\lambda)}{32J} \left[\dfrac{4}{2J+1}\right]$
Q_1 ${}^{P}Q_{12}$	$\dfrac{(2J+1)[(4J^2+4J-1) \pm U(8J^3+12J^2-2J-7+2\lambda)]}{32J(J+1)} \left[\dfrac{4}{2J+1}\right]$
Q_2 ${}^{R}Q_{21}$	$\dfrac{(2J+1)[(4J^2+4J-1) \pm U(8J^3+12J^2-2J+1-2\lambda)]}{32J(J+1)} \left[\dfrac{4}{2J+1}\right]$
R_1 ${}^{Q}R_{12}$	$\dfrac{(2J+1)^2 \pm (2J+1)U(4J^2+4J-7+2\lambda)}{32J(J+1)} \left[\dfrac{4}{2J+1}\right]$
R_2 ${}^{S}R_{21}$	$\dfrac{(2J+1)^2 \pm (2J+1)U(4J^2+4J+1-2\lambda)}{32J(J+1)} \left[\dfrac{4}{2J+1}\right]$
For $J = J'' = \frac{1}{2}$	
R_1 ${}^{S}R_{21}$	$\frac{1}{6}\left[\dfrac{4}{2J+1}\right]$
Q_1 ${}^{R}Q_{21}$	$\frac{1}{3}\left[\dfrac{4}{2J+1}\right]$

$$U = \sqrt{\lambda^2 - 4\lambda + (2J+1)^2}$$

$$\textstyle\sum_{J'} S_{J'J''} = 1$$

Table A.3: Normalised Hönl-London factors $S_{J'J''}$ for NO $A^2\Sigma^+ \leftarrow X^2\Pi$ transitions. These are the expressions of Earls (1935) multiplied by $4/(2J''+1)$ to satisfy the normalisation condition. Note the positive square root is to be used for U and the intensities of the other unlisted branches for $J = \frac{1}{2}$ are identically zero.

	Constant [cm^{-1}]							
v''	B''	D'' $\times 10^6$	A'' $\times 10^{-2}$	A''_D $\times 10^4$	p'' $\times 10^2$	q'' $\times 10^5$	$\nu_{v'v''}$	$A_{v'v''}$ $\times 10^6[s^{-1}]$
0	1.69619	5.326	1.230372	-5.8	1.1882	5.43	44140.8	1.002
1	1.67830	5.4	1.2295	-3.2	1.15	1.5	42264.7	1.375
2	1.66080	5.4	1.2272	-3.2	1.15	1.5	40416.9	1.124
3	1.64330	5.4	1.2246	-3.2	1.15	1.5	38597.1	0.7147
4	1.62624	5.4	1.2211	-3.2	1.15	1.5	36805.3	0.3905
5	1.60782	5.4	1.2184	-3.2	1.15	1.5	35041.4	0.1925
6	1.59040	5.4	1.2153	-3.2	1.15	1.5	33305.4	0.08801
7	1.57227	5.4	1.2123	-3.2	1.15	1.5	31597.4	0.03799

Table A.4: Spectroscopic constants for $NOX^2\Pi(v''=0\text{–}7)$. All constants are in units of cm^{-1} unless given explicitly. $A_{v'v''}$ $[s^{-1}]$ and $\nu_{v'v''}$ $[cm^{-1}]$ are from Piper and Cowles (1986). Values for $v'' = 0$ are repeated here from Table A.1 while the remaining values are from Engleman and Rouse (1971).

where the sum is over all J' that combine with the level J''. In practice, this means multiplying the equations of Earls by $4/(2J''+1)$. Note there are only three transitions that originate from a level with a given J'' of a particular parity and multiplet term. For example, consider the three transitions in Fig. A.1 originating from the level $J'' = 23/2$ with parity e in the $^2\Pi_{1/2}$ state. They are the P_1, R_1 and $^RQ_{21}$ transitions with Hönl-London factors 0.32380, 0.33578 and 0.34042, respectively, which sum exactly to one in accordance with Eq. A.20.

The Einstein B coefficients $[s^{-1}(W/cm^2/cm^{-1})^{-1}]$ are given by Eqs. 20 and 21 of Reisel et al. (1992) as†

$$B_{J'J''} = \frac{1}{8\pi hc^2\nu^3_{J'J''}}\left(\frac{2J'+1}{2J''+1}\right)A_{J'J''} \tag{A.21}$$

and

$$B_{J''J'} = \frac{2J''+1}{2J'+1}B_{J''J'}\ , \tag{A.22}$$

where h [Js] is Planck's constant, c [cm/s] is the speed of light and $\nu_{J'J''}$ $[cm^{-1}]$ is the transition frequency. Combining Eqs. A.21 and A.22 and inserting the values

†Reisel et al. (1992) uses units of $s^{-1}(J\ m^{-2}\ Hz^{-1})^{-1}$.

for g'_n and g''_n, we obtain

$$B_{J'J''} = \frac{1}{16\pi hc^2\nu^3_{J'J''}}\left(\frac{\nu_{J'J''}}{\nu_{v'v''}}\right)^2 A_{v'v''}S_{J'J''} \ . \tag{A.23}$$

The use of Hönl-London factors which are normalised to unity removes the rotational degeneracy terms $(2J+1)$ from this last equation. In general, the ratio of frequencies in Eq. A.23 is only a small correction factor. To convert the B coefficients to SI units, the relation

$$B\ [\mathrm{s}^{-1}(\mathrm{W/cm^2/cm^{-1}})^{-1}] \times 10^{-6} \times c^2 = B\ [\mathrm{s}^{-1}(\mathrm{Jm^{-2}\ Hz^{-1}})^{-1}] \tag{A.24}$$

is used, where c [cm s^{-1}] is the speed of light.

A.6 Boltzmann Fractions

The Boltzmann fraction of a state J, multiplet term i and parity π is given by[†]

$$f_{\mathrm{B}} = \frac{2J''+1}{Z_{total}}\exp\left[-\frac{1}{k}\left(\frac{G(v'')}{T_{\mathrm{vib}}} + \frac{F''_{i\pi}(J'',v'')}{T_{\mathrm{rot}}}\right)\right] \ . \tag{A.25}$$

Here we have indicated the rotational and vibrational contributions to f_{B} and made the distinction between the rotational temperature T_{rot} and vibrational temperature T_{vib}. $F''_{i\pi}(J'',v'')$ is the rotationally dependent part of the energy of the absorbing state and $G(v'')$ is the vibrational energy (given by Eqs. A.9 and A.12 respectively). $k = 0.695\ \mathrm{cm^{-1}/K}$ is the Boltzmann constant. The explicit inclusion of a vibrational temperature is a unique addition to the original equations provided by Di Rosa (1996) and allows us to calculate Boltzmann fractions for the case of vibrational nonequilibrium—a common phenomena in hypersonic wind-tunnel facilities. Z_{total} is the total partition function given by

$$\begin{aligned} Z_{\mathrm{total}} &= \left\{2\sum_{v''=0}^{7}\sum_{i=1}^{2}\sum_{J''=0.5}^{90.5}(2J''+1)\exp\left[-\frac{1}{k}\left(\frac{G(v'')}{T_{\mathrm{vib}}} + \frac{F''_{i\pi}(J'',v'')}{T_{\mathrm{rot}}}\right)\right]\right\} \\ &+ \left\{\frac{kT}{B'(v=0)} \times \frac{2\exp[-T'_e/kT]}{1-\exp[-G'(0)/kT]}\right\} \ , \end{aligned} \tag{A.26}$$

where, as usual, double-primed variables refer to $X^2\Pi$ and single primed to $A^2\Sigma^+$. Hence, we have a summation over all J'' within a particular multiplet term i; the second summation ensures that all of the multiplet terms i are included; the third summation is over the first eight vibrational levels; and finally a multiplication by 2

[†]Recall $i = 1$ for $^2\Pi_{1/2}$ and $i = 2$ for $^2\Pi_{3/2}$.

which adequately accounts for Λ-type doubling. The last term in braces is a corrective term for the $A^2\Sigma^+$ state and is negligible for all but the highest temperatures. With the constants in Table A.4, we can now calculate the total partition function, and hence the Boltzmann fraction, for each rotational level in the first several vibrational levels of the X-state. Di Rosa (1996) has determined the accuracy of the Z_{total} calculation at 2000 K, when the summation is up to $v'' = 3$ and $J'' \approx 90$, to be within 0.1% of the asymptotic limit.

		$^2\Pi_{1/2}$					$^2\Pi_{3/2}$		
N''	J''	$-/+$	e/f	$F_1(J'')$	N''	J''	$-/+$	e/f	$F_2(J'')$
1	1/2	+	e	-59.828	2	3/2	−	e	64.983
1	1/2	−	f	-59.816	2	3/2	+	f	64.983
1	3/2	−	e	-54.818	3	5/2	+	e	73.582
1	3/2	+	f	-54.794	3	5/2	−	f	73.582
2	5/2	+	e	-46.462	4	7/2	−	e	85.621
2	5/2	−	f	-46.426	4	7/2	+	f	85.621
3	7/2	−	e	-34.762	5	9/2	+	e	101.097
3	7/2	+	f	-34.714	5	9/2	−	f	101.908
4	9/2	+	e	-19.717	6	11/2	−	e	120.011
4	9/2	−	f	-19.657	6	11/2	+	f	120.011

Table A.5: Sample calculation of NO $X^2\Pi(v'' = 0)$ rotational energy levels. Energies are in units of cm^{-1}. The vibrational energy is $G(v'' = 0) = 948.659$ cm^{-1}.

			$A^2\Sigma^+$		
N'	J'	$-/+$	e/f	$F_1(N')$	$F_2(N')$
0	1/2	+	e	0.000	
1	3/2	−	e	3.971	
1	1/2	−	f		3.975
2	5/2	+	e	11.915	
2	3/2	+	f		11.922
3	7/2	−	e	23.831	
3	5/2	−	f		23.840
4	9/2	+	e	39.718	
4	7/2	+	f		39.730
5	11/2	−	e	59.577	
5	9/2	−	f		59.592
6	13/2	+	e	83.406	
6	11/2	+	f		83.424
7	15/2	−	e	111.226	

Table A.6: Sample calculation of NO $A^2\Sigma^+(v' = 0)$ rotational energy levels. Energies are in units of cm^{-1}. The vibrational energy is $G(v' = 0) = 1183.121$ cm^{-1}.

References

Abbitt, III, J., Hartfield, R. J. and McDaniel, J. C. (1991), 'Mole-fraction imaging of transverse injection in a ducted supersonic flow', *AIAA Journal* **29**, 431–435.

Allen, M. G., Davis, S. J. and Donohue, K. (1990), 'Planar measurements of instantaneous species and temperature distributions in reacting flows: A novel approach to ground testing instrumentation', *AIAA Paper 90-2383* .

Allen, M. G., McManus, K. R. and Sonnenfroh, D. M. (1995), 'PLIF imaging in spray flame combusters at elevated pressure', *AIAA Paper 95-0172* .

Allen, M. G., Parker, T. E., Reinecke, W. G., Hartmut, H. L., Foutter, R. R., Rawlins, W. T. and Davis, S. J. (1993), 'Fluorescence imaging of OH and NO in a model scramjet combuster', *AIAA Journal* **31**, 505–512.

Allen, M. G., Reinecke, W. G., Legner, H. H., Foutter, R. R., Rawlins, W. T. and Davis, S. J. (1992), 'Instantaneous temperature and concentration imaging in supersonic air flow behind a rear-facing step with hydrogen injection', *AIAA Paper 92-0137* .

Almy, G. M. and Horsfall, Jr., R. B. (1937), 'The spectra of neutral and ionized boron hydride', *Physical Review* **51**, 491–500.

Altkorn, R. and Zare, R. N. (1984), 'Effects of saturation on laser-induced fluorescence measurements of population and polarisation', *Annual Review of Physical Chemistry* **35**, 265–289.

Anderson, Jr., J. D. (1989), *Hypersonic and High Temperature Gas Dynamics*, McGraw-Hill.

Anderson, Jr., J. D. (1990), *Modern Compressible Flow: With Historical Perspective*, 2nd edn, McGraw-Hill.

Andresen, P., Meijer, G., Schlüter, H., Voges, H., Koch, A., Hentschel, W., Oppermann, W. and Rothe, W. (1990), 'Fluorescence imaging inside an internal combustion engine using tunable excimer lasers', *Applied Optics* **29**, 2392–2402.

Battles, B. E. (1994), Quantitative Fluorescence Measurements of Nitric Oxide and the Hydroxyl Radical in High Pressure Methane Flames, PhD thesis, Stanford University.

Beck, W. H., Müller, T. and Wollenhaupt, M. (1993), Application of spectroscopic diagnostic techniques to studies on HEG: Preparatory LIF work and emission spectroscopy results, *in* '15th International Congress on Instrumentation in Aerospace Simulation Facilities'.

Beck, W. H., Wollenhaupt, M., Rosenhauer, M., Müller, T. and Jourdan, J. (1996), 'Status of the development and implementation of optical spectroscopic techniques on the DLR high enthalpy shock tunnel HEG', *AIAA Paper 96-2221* .

Berg, J. O. and Shackleford, W. L. (1979), 'Rotational redistribution effect on saturated laser-induced fluorescence', *Applied Optics* **18**(13), 2093–2094.

Bertin, J. J. (1994), *Hypersonic Aerothermodynamics*, AIAA, Washington DC.

Boyce, R. R. (1995), Computational Fluid Dynamics Code Validation using a Free Piston Shock Tunnel, PhD thesis, Australian National University.

Bradley, R. G. (1988), CFD validation philosophy, *in* 'Validation of Computational Fluid Dynamics', AGARD-CP-437.

Brown, J. M., Hougen, J. T., Johns, J. W. C., Kopp, I., Lefebvre-Brion, H., Merer, A. J., Ramsay, D. A., Rostas, J. and Zare, R. N. (1975), 'The labeling of parity doublet levels in linear molecules', *Journal of Molecular Spectroscopy* **55**, 500–503.

Burke, A. F. and Bird, K. D. (1962), The use of conical and contoured expansion nozzles in hypervelocity facilites, *in* 'Advances in Hypervelocity Techniques', Second Symposium on Hypervelocity Techniques, Plenum Press, University of Denver, pp. 373–424.

Cattolica, R. J. and Stephenson, D. A. (1984), Two-dimensional imaging of flame temperature using laser-induced fluorescence, *in* J. R. Bowen, N. Manson, A. K. Oppenheim and R. I. Soloukhin, eds, 'Dynamics of Flames and Reactive Systems', Vol. 95, AIAA, New York, pp. 714–721.

Chang, A. Y., Di Rosa, M. D. and Hanson, R. K. (1992), 'Temperature dependence of collision broadening and shift in the NO $A \leftarrow X(0,0)$ band in the presence of argon and nitrogen', *Journal of Quantitative Spectroscopy and Radiative Transfer* **47**, 375–390.

Chue, R. S. M. and Itoh, K. (1996), Influence of reflected-shock/boundary-layer interaction on driver-gas contamination in high-enthalpy shock tunnels, *in* '20th International Symposium on Shock Waves', World Scientific, pp. 777–782.

Crane, K. C. and Stalker, R. J. (1977), 'Mass-spectrometric analysis of hypersonic flows', *Journal of Physics D : Applied Physics* **10**, 679–695.

Daily, J. W. (1977*a*), 'Saturation effects in laser induced fluorescence spectroscopy', *Applied Optics* **16**(3), 568–571.

Daily, J. W. (1977*b*), 'Use of rate equations to describe laser excitation in flames', *Applied Optics* **16**(8), 2322–2327.

Danehy, P. M., Palma, P. C., Boyce, R. R. and Houwing, A. F. P. (1997), Comparison of theoretical and experimental laser-induced fluorescence images in hypersonic shock-layer flows, *in* '21th International Symposium on Shock Waves', Great Keppel Island, Australia.

Davies, L. and Wilson, J. L. (1969), 'Influence of reflected shock and boundary-layer interaction on shock-tube flows', *Physics of Fluids* **12**(6), I37–I43. Supplement I.

Demtröder, W. (1996), *Laser Spectroscopy*, 2nd edn, Springer-Verlag.

Di Rosa, M. D. (1994), 'Collision-broadening and -shift of NO $\gamma(0,0)$ absorption lines by H_2O, O_2, and NO at 295 K', *Journal of Molecular Spectroscopy* **164**, 97–117.

Di Rosa, M. D. (1996), High-Resolution Line Shape Spectroscopy of Transitions in Gamma Bands of Nitric Oxide, PhD thesis, Stanford University.

Doherty, P. M. and Crosley, D. R. (1982), 'Polarisation of laser-induced fluorescence of OH in an atmospheric pressure flame', *Applied Optics* **23**, 713–721.

Dreier, T., Dreizler, A. and Wolfrum, J. (1992), 'The application of a Raman-shifted tunable KrF excimer laser for laser-induced fluorescence combustion diagnostics', *Applied Physics B* **55**, 381–387.

Dumitrescu, M. P. (1996), Trapping the boundary layer: A method to diminish flow contamination in shock tunnels, *in* '20th International Symposium on Shock Waves', World Scientific, pp. 1581–1586.

Earls, L. T. (1935), 'Intensities in $^2\Pi$–$^2\Sigma$ transitions in diatomic molecules', *Physical Review* **48**, 423–424.

East, R. A., Stalker, R. J. and Baird, J. P. (1980), 'Measurements of heat transfer to a flat plate in a dissociated high-enthalpy laminar air flow', *Journal of Fluid Mechanics* **97**(4), 673–699.

Ebata, T., Anezaki, Y., Fujii, M., Mikami, N. and Ito, M. (1984), 'Rotational energy transfer in NO($A^2\Sigma^+$, v=0 and 1) studied by two-color double-resonance spectroscopy', *Journal of Chemical Physics* **84**, 151–157.

Ebrahim, N. (1975), Nonequilibrium in High Enthalpy Carbon Dioxide Flows, PhD thesis, Australian National University.

Eckbreth, A. C. (1996), *Laser Diagnostics for Combustion Temperature and Species*, 2nd edn, Gordon and Breach Publishers.

Einstein, A. (1917), 'Zur quantentheorie der strahlung', *Physikalische Zeitschrift* **18**, 121–128.

Engleman, Jr., R. and Rouse, P. E. (1971), 'The β and γ bands of nitric oxide observed during the flash photolysis of nitrosyl chloride', *Journal of Molecular Spectroscopy* **37**, 240–251.

Freedman, R. and Nicholls, R. W. (1983), 'Molecular constants for the $v'' = 0(X^2\Pi)$ and $v' = 0, 1(A^2\Sigma^+)$ levels of the NO molecule and its isotopes', *Journal of Molecular Spectroscopy* **83**, 223–227.

Gaydon, A. G. and Hurle, I. R. (1963), *The Shock Tube in High Temperature Chemical Physics*, Chapman and Hall, London.

Gilmore, J. O., Sharma, S. and Fletcher, D. (1996), Single-pulse spontaneous Raman-scattering measurements in an expanding nitrogen/oxygen admixture, *in* '20th International Symposium on Shock Waves', World Scientific, pp. 1605–1610.

Greenstein, H. and Bates, Jr., C. W. (1975), 'Line-width and tuning effects in resonant excitation', *Journal of the Optical Society of America* **65**(1), 33–40.

Hahn, J. W., Park, C. W. and Park, S. N. (1997), 'Broadband coherent anti-Stokes Raman spectroscopy with a modeless dye laser', *Applied Optics* **36**(27), 6722–6728.

Hannemann, K., Krek, R. and Eitelberg, G. (1996), Latest calibration results of HEG contoured nozzle, *in* '20th International Symposium on Shock Waves', World Scientific, pp. 1575–1580.

Herzberg, G. (1989), *Molecular Spectra and Molecular Structure: I. Spectra of Diatomic Molecules*, 2nd edn, Kreiger, Malabar, Florida.

Hiller, B. and Hanson, R. K. (1988), 'Simultaneous planar measurements of velocity and pressure fields in gas flows using laser-induced fluorescence', *Applied Optics* **27**(1), 33–48.

Hornung, H. G. and Bélanger, J. (1990), 'Role and techniques of ground testing for simulation of flows up to orbital speed', *AIAA Paper 90-1377*.

Houwing, A. F. P., Kamel, M. R., Morris, C. I., Wehe, S. D., Boyce, R., Thurber, M. C. and Hanson, R. K. (1996), 'PLIF imaging and thermomery of NO/N_2 shock layer flows in an expansion tube', *AIAA Paper 96-0537*.

Huber, K. and Herzberg, G. (1979), *Molecular Spectra and Molecular Structure: IV. Constants of Diatomic Molecules*, Van Nostrand Reinhold, New York.

Huber, M. C. E. and Sandeman, R. J. (1986), 'The measurement of oscillator strengths', *Reports on Progress in Physics* **49**, 397–490.

Humlícek, J. (1979), 'An efficient method for the evaluation of the complex probability: the Voigt function and its derivatives', *Journal of Quantitative Spectroscopy and Radiative Transfer* **21**, 309–313.

Itoh, K. (1996), Tuned operation of a free-piston shock tunnel, *in* '20th International Symposium on Shock Waves', World Scientific, pp. 43–51.

Ketterle, W., Schäfer, M., Arnold, A. and Wolfrum, J. (1992), '2d single-shot imaging of OH radicals using tunable excimer lasers', *Applied Physics B* **54**, 109–112.

Kewley, D. J. (1975), Vibrational and Chemical Relaxation Rates of Diatomic Gases, PhD thesis, Australian National University.

Killinger, D. K., Wang, C. C. and Hanabusa, M. (1976), 'Intensity and pressure dependence of resonance fluorescence of OH induced by a tunable uv laser', *Physical Review A* **13**(6), 2145–2152.

Korkegi, R. H. (1985), 'Impact of computational fluid dynamics on development test facilities', *Journal of Aircraft* **22**(3), 182–187.

Krehl, P. and Engemann, S. (1995), 'August Toepler — the first who visualized shock waves', *Shock Waves* **5**, 1–18.

Kychakoff, G., Howe, R. D. and Hanson, R. K. (1984), 'Quantitative flow visualisation technique for measurements in combustion gases', *Applied Optics* **23**, 704–712.

Laurendeau, N. M. (1988), 'Temperature measurements by light-scattering methods', *Progress in Energy Combustion Science* **14**, 147–170.

Lee, M. P. (1991), Temperature Measurements in Gases using Planar Laser-Induced Fluorescence Imaging of NO and O_2, PhD thesis, Stanford University.

Lemoine, F. and Leporcq, B. (1995), 'An efficient optical pressure measurement in compressible flows: Laser-induced iodine fluorescence', *Experiments in Fluids* **19**, 150–158.

Levenson, M. D. and Kano, S. S. (1987), *Introduction to Nonlinear Laser Spectroscopy*, Academic Press, London.

Lewis, B. R., Gibson, S. T., Baldwin, K. G. H. and Carver, J. H. (1989), 'Vacuum-ultraviolet absorption linewidth measurement using high-order anti-Stokes Raman-shifted radiation', *Journal of the Optical Society of America B*

6(6), 1200–1208.

Liepmann, H. W. and Roshko, A. (1957), *Elements of Gasdynamics*, John Wiley & Sons, New York.

Lucht, R. P. and Laurendeau, N. M. (1979), 'Two-level model for near saturated fluorescence in diatomic molecules', *Applied Optics* **18**, 856–861.

Mach, E. and Wosyka, J. (1875), 'Über einge mechanische Wirkungen des elecktrischen Funkens', *Sitzungsber Akad Wiss Wien (II. Abth.)* **72**, 44–52.

Maus, J. R., Griffith, B. J., Szema, K. Y. and Best, J. T. (1984), 'Hypersonic Mach number and real gas effects on shuttle orbiter aerodynamics', *Journal of Spacecraft and Rockets* **21**(2), 136–141.

McDaniel, J. C., Hiller, B. and Hanson, R. K. (1983), 'Simultaneous multi-point velocity measurements using laser-induced iodine fluorescence', *Optics Letters* **8**(1), 51–53.

McDermid, I. S. and Laudenslager, J. B. (1982), 'Radiative lifetimes and electronic quenching rate constants for single-photon-excited rotational levels of NO ($A^2\Sigma^+, v' = 0$)', *Journal of Quantitative Spectroscopy and Radiative Transfer* **27**, 483–492.

McIntosh, M. (1968), Computer program for the numerical calculation of frozen equilibrium conditions in shock tunnels, Technical report, Department of Physics, Faculties, Australian National University.

McIntyre, T. J. (1995), Intensified CCD camera system, Technical report, Department of Physics, Faculties, Australian National University.

McMillin, B. K. (1993), Instantaneous Two-Line PLIF Temperature Imaging of Nitric Oxide in Supersonic Mixing and Combustion Flowfields, PhD thesis, Stanford University.

McMillin, B. K., Lee, M. P. and Hanson, R. K. (1992), 'Planar laser-induced fluorescence imaging of shock-tube flows with vibrational nonequilibrium', *AIAA Journal* **30**, 436–443.

McMillin, B. K., Palmer, J. L. and Hanson, R. K. (1991), 'Two-dimensional temperature measurements of shock tube flows using planar laser-induced fluorescence imaging of nitric oxide', *AIAA Paper 91-1670* .

McMillin, B. K., Palmer, J. L. and Hanson, R. K. (1993), 'Temporally resolved, two line fluorescence imaging of NO temperature in a transverse jet in a supersonic crossflow', *Applied Optics* **32**, 7532–7545.

McMillin, B. K., Seitzman, J. M. and Hanson, R. K. (1994), 'Comparison of NO and OH planar LIF temperature measurements in SCRAMJET model flowfields',

AIAA Journal **32**, 1945–1952.

Mehta, U. B. (1990), 'Computational requirements for hypersonic flight performance estimates', *Journal of Spacecraft and Rockets* **27**(2), 103–112.

Meijer, G., ter Meulen, J., Andresen, P. and Bath, A. (1986), 'Sensitive quantum state selective detection of H_2O and D_2O by (2+1)-resonance enhanced multi-photon ionization', *Journal of Chemical Physics* **85**(12), 6914–6922.

Milne, E. A. (1924), 'The equilibrium of the calcium chromosphere', *Monthly Notices of the Royal Astronomical Society* **85**(2), 111–141.

Mitchell, A. C. G. and Zemansky, M. W. (1934), *Resonance Radiation and Excited Atoms*, Cambridge University Press.

Mudford, N. R. (1992), Transient disturbances in free piston shock tunnels, *in* 'Third International Workshop on Shock Tube Technology', Department of Mechanical Engineering, University of Queensland and Department of Physics, Australian National University.

Mundt, C. (1992), 'Calculation of hypersonic, viscous, non-equilibrium flows around re-entry bodies using a coupled boundary layer/Euler method', *AIAA Paper 92-2856* .

Neumann, R. D. (1988), Missions and requirements, *in* 'Special Course on Aerothermodynamics of Hypersonic Vehicles', AGARD Report 761, Neuilly sur Seine, France.

Neumann, R. D. (1989), Experimental methods for hypersonics: Capabilities and limitations, *in* '2nd Joint Europe/US Short Course in Hypersonics', Colarado Springs.

Olejniczak, J. (1997), Computational and Experimental Study of Nonequilibrium Chemistry in Hypersonic Flows, PhD thesis, University of Minnesota.

Palma, P. C., Houwing, A. F. P. and Sandeman, R. J. (1993), 'Absolute intensity measurements of impurity emissions in a shock tunnel and their consequences for laser-induced fluorescence experiments', *Shock Waves* **3**(1), 49–53.

Palmer, J. L. and Hanson, R. K. (1995), 'Single-shot OH PLIF thermometry in a reacting, supersonic free jet', *AIAA Paper 95-0517* .

Palmer, J. L., McMillin, B. K. and Hanson, R. K. (1992), 'Planar laser-induced fluorescence imaging of velocity and temperature in shock tunnel free jet flow', *AIAA Paper 92-0672* .

Palmer, J. L., McMillin, B. K. and Hanson, R. K. (1993), 'Planar laser-induced fluorescence in free jet flows with vibrational nonequilibrium', *AIAA Paper 93-0046* .

Palmer, J. L., McMillin, B. K. and Hanson, R. K. (1996), 'Multi-line fluorescence imaging of the rotational temperature field in a shock tunnel', *Applied Physics B* **63**(8), 167–178.

Partridge, Jr., W. P. and Laurendeau, N. M. (1995), 'Formulation of a dimensionless overlap fraction to account for spectrally distributed interactions in fluorescence studies', *Applied Optics* **34**(15), 2645–2647.

Paul, P. H., Gray, J. A., Durant, Jr., J. L. and Thoman, Jr., J. W. (1994), 'Collisional quenching corrections for laser-induced fluorescence measurements of NO$A^2\Sigma^+$', *AIAA Journal* **32**(8), 1670–1675.

Paul, P. H. and Hanson, R. K. (1990), 'Applications of laser-induced fluorescence imaging diagnostics to reacting flows', *AIAA Paper 90-1844* .

Paul, P. H., Lee, M. P. and Hanson, R. K. (1989), 'Molecular velocity imaging of supersonic flows using pulsed planar laser-induced fluorescence of NO', *Optics Letters* **14**, 417–419.

Paull, A. (1996), A simple shock-tunnel driver-gas detector, *in* '20th International Symposium on Shock Waves', World Scientific, pp. 1557–1562.

Paull, A. and King, K. D. (1995), 'A driver gas detection device for shock tunnels', *Shock Waves* **4**(5), 289–291.

Piepmeier, E. H. (1972), 'Theory of laser saturated atomic resonance fluorescence', *Spectrochimica Acta* **27B**, 431–443.

Piper, L. G. and Cowles, L. M. (1986), 'Einstein coefficients and transition moment variation for the NO($A^2\Sigma^+$–$X^2\Pi$) transition', *Journal of Chemical Physics* **85**(5), 2419–2422.

Press, W. H., Teukolsky, S. A., Vetterling, W. T. and Flannery, B. P. (1992), *Numerical Recipies in FORTRAN: The Art of Scientific Computing*, 2nd edn, Cambridge University Press, New York.

Quagliaroli, T. M., Laufer, G., Hollo, S. D., Krauss, R., Whithurst III, R. and McDaniel, Jr., J. (1994), 'Planar KrF laser-induced OH fluorescence imaging in a supersonic combustion tunnel', *Journal of Propulsion and Power* **10**, 377–381.

Raiche, G. A. and Crosley, D. R. (1990), 'Temperature dependent quenching of the $A^2\Sigma^+$ and $X^2\Pi$ states of NO', *Journal of Chemical Physics* **92**, 5211–5218.

Reisel, J. R., Carter, C. D. and Laurendeau, N. M. (1992), 'Einstein coefficients for rotational lines of the (0,0) band of NO $A^2\Sigma^+$–$X^2\Pi$ system', *Journal of Quantitative Spectroscopy and Radiative Transfer* **47**(1), 43–54.

Ruyten, W. M. (1996), 'Comparison of calculated and measured temperature fields

in the AEDC impulse facility', *AIAA Paper 96-2236* .

Ruyten, W. M., Smith, M. S. and Williams, W. D. (1995), On the role of laser absorption in planar laser-induced fluorescence imaging of high-enthalpy flows, *in* '20th International Symposium on Shock Waves', Pasadena, CA.

Seigman, A. E. (1986), *Lasers*, University Science Books, Mill Valley, California.

Seitzman, J. M. and Hanson, R. K. (1993), Planar fluorescence imaging in gases, *in* 'Instrumentation for Flows with Combustion', Academic Press Ltd.

Seitzman, J. M., Hanson, R. K., Barber, P. A. and Hess, C. (1994), 'Application of quantitative two-line OH PLIF for temporally resolved planar thermometry in reacting flows', *Applied Optics* **33**, 4000–4012.

Seitzman, J. M., Kychakoff, G. and Hanson, R. K. (1985), 'Instantaneous temperature field measurements using planar laser-induced fluorescence', *Optics Letters* **10**(9), 439–441.

Skinner, K. A. and Stalker, R. J. (1994), 'Time-of-flight mass spectrometer for impulse facilities', *AIAA Journal* **32**, 2325–2328.

Slade, J. C., Crane, K. C. and Stalker, R. J. (1993), Driver gas detection by quadrupole mass spectrometry in shock tunnels, *in* '19th International Symposium on Shock Waves, Marseille, France', Springer-Verlag, Heidelberg, pp. 293–298.

Smith, C. E. (1966), 'The starting process in a hypersonic nozzle', *Journal of Fluid Mechanics* **24**(4), 625–640.

Snowdon, P., Skippon, S. M. and Ewart, P. (1991), 'Improved precision of single-shot temperature measurements by broadband CARS by use of a modeless laser', *Applied Optics* **30**(9), 1008–1010.

Stalker, R. J. (1967), 'A study of the free-piston shock tunnel', *AIAA Journal* **5**(12), 2160–2165.

Stalker, R. J. (1972), 'Development of a hypervelocity wind tunnel', *Aeronautical Journal* **76**, 374–384.

Stalker, R. J. and Crane, K. C. A. (1978), 'Driver gas contamination in a high-enthalpy reflected shock tunnel', *AIAA Journal* **16**(3), 277–279.

Stalker, R. J. and McIntosh, M. K. (1973), 'Hypersonic nozzle flow of air with high initial dissociation levels', *Journal of Fluid Mechanics* **58**(4), 749–761.

Stephenson, J. C. (1974), 'Vibrational relaxation of $NOX^2\Pi(v = 1)$ in the temperature range 100–300 K', *Journal of Chemical Physics* **60**, 4289–4294.

Sudani, N. and Hornung, H. G. (1997), Detection and reduction of driver gas contamination in a high-enthalpy shock tunnel, *in* '21st International Symposium on Shock Waves, Great Keppel Island, Australia'.

Sudani, N. and Hornung, H. G. (1998), 'Gasdynamical detectors of driver gas contamination in a high-enthalpy shock tunnel', *AIAA Journal* **36**(3), 313–319.

Thorne, A. P. (1988), *Spectrophysics*, 2nd edn, Chapman and Hall.

Timmermann, A. and Wallenstein, R. (1981), 'Doppler-free two-photon excitation of nitric oxide with frequency-stabilized cw dye laser radiation', *Optics Communications* **39**, 239–242.

Toepler, A. (1875), *Beobachtungen nach einer neuen optischen Methode - Ein Beitrag zur Experimentalphysik*, Max Cohen & Sohn, Bonn.

Vardavas, I. (1984), 'Modelling reactive gas flows within shock tunnels', *Australian Journal of Physics* **37**, 157–177.

Vincenti, W. G. and Kruger, Jr., C. H. (1975), *Introduction to Physical Gas Dynamics*, Kreiger, Malabar, Florida.

Wollenhaupt, M., Rosenhauer, M., Müller, T., Jourdan, J., Scholz, J., Hartung, S. and Beck, W. H. (1997), NO laser-induced fluorescence studies for the application of single-shot two-line thermoemtry to HEG, *in* '21th International Symposium on Shock Waves', Great Keppel Island, Australia.

Yariv, A. (1988), *Quantum Electronics*, 3rd edn, John Wiley & Sons, New York.